1999 SUMMER RESEARCH PROGRAM FOR HIGH SCHOOL JUNIORS

AT THE

UNIVERSITY OF ROCHESTER'S

LABORATORY FOR LASER ENERGETICS

Reviewed for Classification 3-28-2000
(Date)

UNCLASSIFIED

R.L. McCrory, Jr.
Authorized Derivative Classifier

STUDENT RESEARCH REPORTS

RECEIVED
JUL 17 2000
OSTI

PROGRAM COORDINATOR

Dr. R. Stephen Craxton
LABORATORY FOR LASER ENERGETICS
University of Rochester
250 East River Road
Rochester, NY 14623-1299

During the summer of 1999, 12 students from Rochester-area high schools participated in the Laboratory for Laser Energetics' Summer High School Research Program. The goal of this program is to excite a group of high school students about careers in the areas of science and technology by exposing them to research in a state-of-the-art environment. Too often, students are exposed to "research" only through classroom laboratories that have prescribed procedures and predictable results. In LLE's summer program, the students experience all of the trials, tribulations, and rewards of scientific research. By participating in research in a real environment, the students often become more enthusiastic about careers in science and technology. In addition, LLE gains from the contributions of the many highly talented students who are attracted to the program.

The students spent most of their time working on their individual research projects with members of LLE's technical staff. The projects were related to current research activities at LLE and covered a broad range of areas of interest including laser modeling, diagnostic development, chemistry, liquid crystal devices, and opacity data visualization. The students, their high schools, their LLE supervisors and their project titles are listed in the table. Their written reports are collected in this volume.

The students attended weekly seminars on technical topics associated with LLE's research. Topics this year included lasers, fusion, holography, optical materials, global warming, measurement errors, and scientific ethics. The students also received safety training, learned how to give scientific presentations, and were introduced to LLE's resources, especially the computational facilities.

The program culminated with the High School Student Summer Research Symposium on 25 August at which the students presented the results of their research to an audience that included parents, teachers, and members of LLE. Each student spoke for approximately ten minutes and answered questions. At the symposium the William D. Ryan Inspirational Teacher award was presented to Mr. John Harvey, a mathematics teacher at Honeoye Falls-Lima Senior High School. This annual award honors a teacher, nominated by alumni of the LLE program, who has inspired outstanding students in the areas of science, mathematics, and technology.

DISCLAIMER

A total of 103 high school students have participated in the program since it began in 1989. The students this year were selected from approximately 80 applicants. Each applicant submitted an essay describing their interests in science and technology, a copy of their transcript, and a letter of recommendation from a science or math teacher.

LLE plans to continue this program in future years. The program is strictly for students from Rochester-area high schools who have just completed their junior year. Applications are generally mailed out in early February with an application deadline near the end of March. For more information about the program or an application form, please contact Dr. R. Stephen Craxton at LLE.

This program was supported by the U.S. Department of Energy Office of Inertial Confinement Fusion under Cooperative Agreement No. DE-FC03-92SF19460.

High School Students and Their Projects (1999)			
Student	**High School**	**Supervisor**	**Project**
Kendra Bussey	Pittsford Sutherland	K. Marshall	Synthesis of Highly Soluble Near-IR Dyes for the Liquid Crystal Point-Diffraction Interferometer
Michael Harvey	R. J. Davis. Livonia	M. Skeldon	Characterization of Inter-Pulse Noise and the Signal-to-Noise Ratio in a Regenerative Amplifier
Peter Hopkins	The Harley School	S. Craxton	Comparing Opacity Data Groups with a Java-Based GUI Solution
Jyoti Kandlikar	Brighton	R. Epstein	Statistical Properties of Continuous and Discrete Distributed Phase Plates
Brian Kubera	Webster	R. Boni	Bandwidth Measurement of Fiber Optic Bundles
Aman Narang	The Harley School	W. Donaldson	Analysis of the 3ω SSD Spectrum of an OMEGA Laser Beamline
Lutao Ning	Brighton	M. Guardelben	Characterization of the Liquid Crystal Point-Diffraction Interferometer
Rohit Rao	Brighton	S. Craxton	LCPDI Modeling
Alice Tran	Spencerport	C. Stoeckl	Integrating Hard X-ray Diagnostics into OMEGA Operations
Jordan VanLare	Victor	K. Marshall	Predicting the Optical and Dielectric Anisotropy of Liquid Crystalline Systems
Jeffrey Vaughan	Fairport	P. Jaanimagi	Removing Distortion in an X-ray Streak Camera
Emily Walton	Fairport	J. Knauer	Measurement of Scattered 351nm Light from OMEGA Targets

"Synthesis of Highly Soluble Near-IR Dyes for the Liquid Crystal Point- Diffraction Interferometer"

Kendra Bussey
Kenneth L. Marshall, advisor
Summer High School Research Program

August 1999

Abstract

Nickel dithiolene dyes show considerable promise for use in the liquid crystal point diffraction interferometer (or LCPDI). Due to the *d*-orbital interactions between the nickel and sulfur atoms in the molecules, the compounds possess a near-IR absorbance band. The dye is utilized in the LCPDI device because of the requirement for the object beam to have the same intensity as the reference beam.

Substitution of thioether groups for alkyl- or alkoxyphenyl substituents in nickel dithiolenes produces a bathochromic shift in the near-IR absorbance band. The new alkylthio-substituted compounds are more efficient absorbers at 1054 nm and are more soluble in the LC host than phenyl-substituted dithiolenes. The use of multi-component dye mixtures improves overall solubility in the LC host and enhances the performance of the LCPDI; however, additional dye components will be necessary in order to meet the requirements for LCPDI use on the OMEGA laser. Nickel dithiolenes with chiral terminal groups form an induced cholesteric phase when they are added to a LC host.

Introduction

As the twenty-first century quickly approaches, laser fusion is becoming a promising form of technology and power, and much research is being performed to develop it. One important requirement for lasers used in fusion experiments is for them to have a uniform optical wave front so that both maximum energy output and uniform target illumination are achieved. The liquid crystal point-diffraction interferometer is used to diagnose aberrations in this optical wave front[1]. For the LCPDI device to function properly there is a need to add a dye that absorbs at the laser wavelength to the liquid crystal host to insure that the object beam and the reference beam have the same intensity.

The ideal dye for use in the LCPDI would have (1) a large absorbance (optical density) at the laser operating wavelength of 1054 nm; (2) high solubility in the liquid crystal host; (3) high thermal stability so the laser would not cause it to decompose; and (4) either a low impact on the order parameter of the liquid crystal host or, preferably, a liquid crystalline phase of its own. This work reports on two dyes that were synthesized for use in the LCPDI device. One of these dyes, tetrakis (n-butylthio)-bis(ethylene-1,2-dithiolene) nickel (0), termed SC4, was previously synthesized and reported in the literature by A. Charlton et al[2], while the other dye, tetrakis (2-methyl-butylthio) bis (ethylene-1,2-dithiolene) nickel (0), termed S2MeBu, had not previously been synthesized. Both dyes have a λ_{max} in the liquid crystal host of 1020 nm; however, the chiral 2-methylbutyl group in S2MeBu provides additional interesting physical properties when the metal complex is dissolved in a liquid crystal host. Both of these dyes were found to be more soluble in E7 than phenyl-substituted compounds previously synthesized. and substituting a thioether group for the phenyl ring produced a bathochromic shift in the near-IR absorption band of 49 nm–now, the absortion is only 35 nm from the ideal λ_{max}. This bathochromic shift has been found to enhance LCPDI performance.

Background

The liquid crystal point-diffraction interferometer

In the liquid crystal point-diffraction interferometer, the laser beam to be diagnosed is brought almost to a focus on a glass microsphere 20 μm in diameter sandwiched between two conductive glass substrates. The cavity between the plates is filled with a liquid crystal fluid that contains the dye. The incident beam is larger in diameter than the microsphere, and the part that passes through the microsphere forms the reference beam, while the part that passes through the dyed nematic liquid crystals forms the object beam. Interaction of the object and reference beams produces optical intereference effects.

Liquid crystals are used because they can be re-oriented using an electric field. The reorientation of the molecules changes the phase of the object beam. The dye causes the intensity of the object beam to be the same as that of the reference beam. After the beam passes through the LCPDI device, light that is not polarized is eliminated using a polarizer. A ground glass viewing screen shows the interferogram produced by the two beams; this can be used to determine the quality of the optics used.

Liquid crystals

The liquid crystalline phase is a unique mesophase in some compounds that is between the solid, crystalline phase and the liquid, fluid phase. These compounds possess a unique "double melting point"—the first melting point is the transition between the solid, crystalline phase and the liquid crystalline phase. The second melting point is the phase transition between the liquid crystalline phase and the isotropic (or disordered liquid) phase.

Liquid crystals have a crystalline structure like a solid, but they move as a fluid. Liquid crystals have four different "phases"—nematic, cholesteric, smectic, and discotic. The nematic and cholesteric phases are the primary concerns in this paper. The nematic phase is the least ordered liquid crystalline phase. The cigar-shaped molecules only are oriented in one plane, with their long axes parallel. In the cholesteric phase (or chiral nematic phase) the cigar-shaped molecules are oriented along two planes; the molecules are arranged in a planar manner in several layers, and the layers are arranged on a helical axis (Fig. 1).

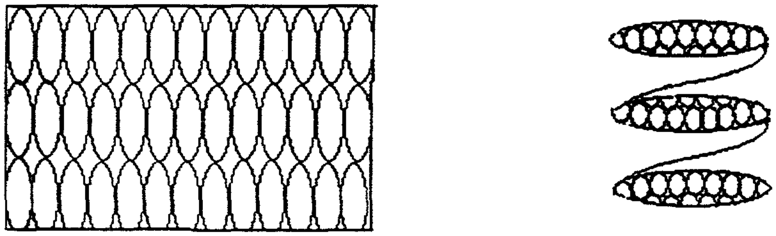

Fig. 1. Nematic liquid crystals, which are cigar shaped molecules, are oriented along one plane (above, left). Cholesteric liquid crystals are also cigar-shaped molecules; however, they are oriented along two planes—the molecules are aligned along their long axes, but the different layers are arranged in a helical fashion.

Merck E7, the liquid crystal host used for the LCPDI devices, is an example of a material that possesses a nematic phase. Merck E7 is a mixture of four different liquid crystals. They are present in different amounts, as shown in Fig. 2.

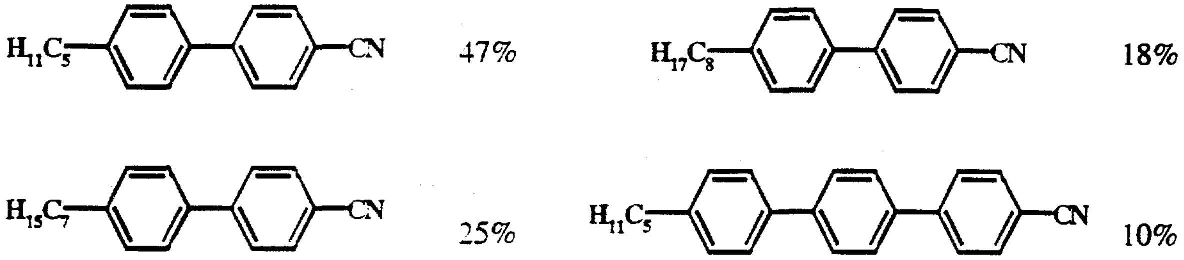

Fig. 2. Merck E7 is a mixture of four different liquid crystalline compounds.

IR absorbing dyes

Dyes are necessary in the liquid crystal point-diffraction interferometer because they cause the intensity of the object beam to be the same as that of the reference beam. They do this by absorbing a specific wavelength—usually the operating wavelength of the laser. The dyes have strong absorption bands in the near-IR absorbance region because of the interactions between the *d*-orbitals of the sulfur and nickel atoms[3]. The nickel dithiolene dyes are relatively highly soluble in liquid crystal hosts and hydrocarbon solvents[7]; this is due to the zerovalent core.

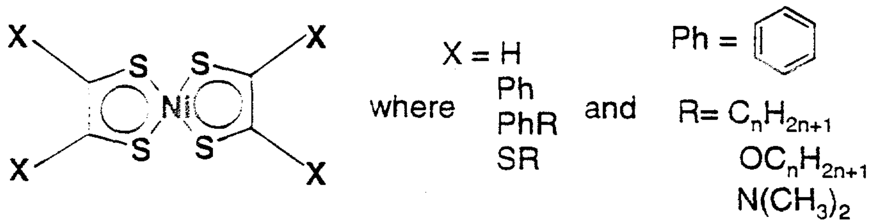

Fig. 3 Interactions between the d-orbitals of the nickel and sulfur atoms cause the near-IR absorbance band.

Different R-groups on the nickel dithiolene complexes affect both solubility and absorbance in the liquid crystal host[3]—this is very important for LCPDI applications, because solubility is very important in achieving the large absorbance, or optical density (OD) that is required for the LCPDI to operate properly. For operation on OMEGA, an OD value of between 1.8-2 is required at 1054 nm.

Experimental

Dye Synthesis

Two dyes with differing terminal groups were synthesized. The first is from a group of dyes reported by A. Charlton et al[2]. The tetrakis (butylthio) bis(ethylene-1,2-dithiolene) nickel (0) and the tetrakis (2-methyl-butylthio) bis (ethylene- 1,2-dithiolene) nickel (0) were synthesized using a modified version of methods prepared by A. E. Underhill et al[4], N. Svenstrup et al.[5], and A. Charlton et al[2].

$[TEA]_2$ [Zn(dmit)$_2$] Synthesis Procedure

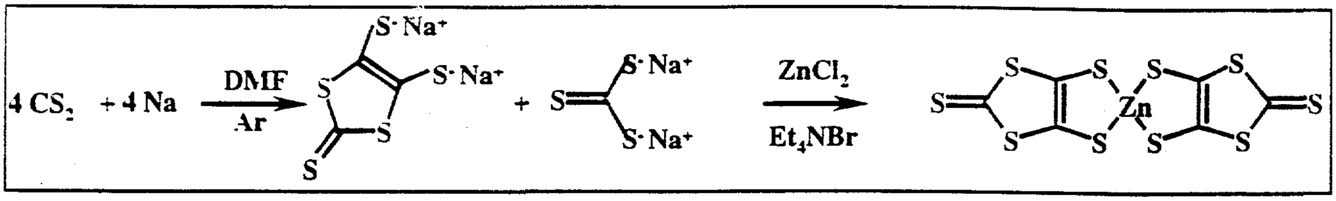

Fig. 4: The first step in the dye synthesis starts with two relatively simple substances, carbon disulfide and sodium metal and produces the $[TEA]_2$ $[Zn(dmit)_2]$.

A method published by A. Underhill et al [4] was used to produce the di(tetraethylammonium) bis (1,3-dithiol-2-thione-4,5-dithiolate) zincate. Sodium metal was sliced into small pieces under paraffin oil and then weighed in a container of toluene (the toluene removed the oil). The sodium metal was placed in 36 ml of carbon disulfide in a 500 ml 3-neck round-bottomed flask that had been purged under argon for 30 min. The flask was equipped with a stir bar and fitted with an addition funnel, a condenser, and an ice bath. Dimethylformamide (DMF, 44 ml) was placed in the addition funnel, and the system was allowed to purge for 20 min. The DMF was added dropwise (which caused a color change to red), and the mixture was allowed to stir overnight. Methanol (25 ml) was added in the morning to decompose any remaining sodium. A mixture of 60 ml methanol and 60 ml de-ionized H_20 was then added to the dark red solution. Four grams of $ZnCl_2$ dissolved in 100 ml of concentrated NH_4OH and 100 ml de-ionized H_20 were added dropwise. Tetraethylammonium bromide (10.6 g) dissolved in 30 ml de-ionized H_20 was added dropwise over 1 ½ hours, and the ice bath was removed. The mixture was allowed to stir overnight, and then the red-orange mixture was filtered. The orange-red crystals were washed with de-ionized H_20, isopropanol, 50:50 isopropanol/ethyl ether, and finally with ethyl ether. A second crop of product crystals was obtained by recrystallization from acetone/isopropanol, and the crystals were dried overnight (17.58 g, 83.34% yield based on $ZnCl_2$; m.p. 205°C).

Synthesis of 4,5-bis(2'-butylthio)-1,3-dithiole-2-thione

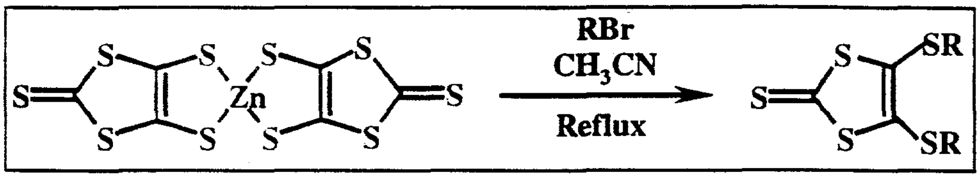

Fig. 5: The reaction to produce the ether is accomplished in one step that takes a relatively small amount of time.

Following the method of N. Svenstrup et al.[5], 3.00 g of bis (1,3-dithiole-2-thione-4,5-dithiolate) zincate was placed in a 3-neck round-bottomed flask equipped with a stir bar, a condenser, and an addition funnel. Acetonitrile (52 ml) was added to the crystals and the mixture was stirred. 1-Bromobutane (2.24 ml) was then added and the solution was refluxed for 1½ hours. After refluxing, the solution was filtered and then the solvent was removed under vacuum using a rotary evaporator. The product was then dissolved in 52 ml of methylene chloride (CH_2Cl_2) and transferred to a separatory funnel. The sample was washed with four 42 ml portions of H_20, dried over anhydrous $MgSO_4$, and the magnesium sulfate was then filtered. The filtrate was concentrated under vacuum using a rotary evaporator. The product was then weighed. (2.26 g, 87.26% yield).

Synthesis of 4,5-bis(2'-methylbutylthio)-1,3-dithiole-2-thione

Following the method of N. Svenstrup et al.[5], 2.91g of di(tetraethylammonium) bis (1,3-dithiol-2-thione-4,5-dithiolate) zincate were placed in a 100-ml 3-neck round-bottomed flask and dissolved in 50 ml of acetonitrile. The flask was fitted with a magnetic stir bar, a condenser, and two stoppers. The reaction mixture was stirred for 15 minutes and 3.02 g of 1-bromo-2-methylbutane were added to the mixture drop-wise (excess was added to ensure that any material lost in the pipette or in the vial would not cause an incomplete reaction). A heating mantle was placed around the flask and the reaction mixture was refluxed for 2 hours. The solution remained a light orange-brown. The mixture was filtered, and red crystals that were not the starting material, according to solubility testing, were filtered off. The filtrate was evaporated under vacuum using a rotary evaporator. The residue was dissolved in methylene chloride, transferred to a separatory funnel, and washed with four 50 ml portions of H_20. The solvent was removed under vacuum using a rotary-evaporator and a reddish-orange oil was recovered, along with a black solid. The mixture was then taken up in toluene and suction-filtered. A black tarry solid was removed and washed with toluene. The red-orange liquid was set aside and the solid was washed with hexane. The red-orange liquid was removed under vacuum until an oil was left. The oil was then weighed. (1.63 g, 59.5% yield).

Synthesis of tetrakis (n-butylthio) nickel bis(ethylene-1,2-dithiolene)

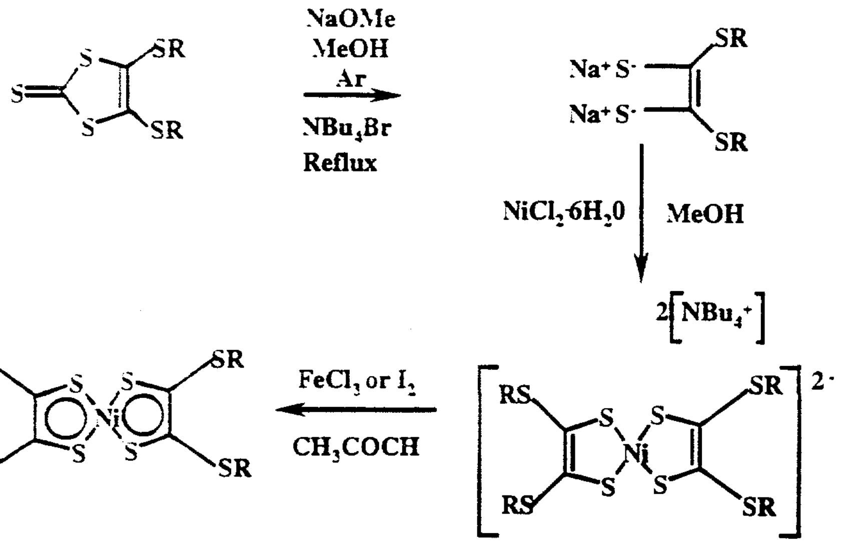

Fig. 6: The above equations are the process for producing the black nickel dye crystals (green in solution) starting from the bis(alkylthio)-1,3-dithiol 2-thione. Originally I_2 was used as the oxidizing agent; then $FeCl_3$ was used.

This nickel dithiolene complex was prepared following the method of A. Charlton[2], with some modifications. A three-neck, round-bottomed, 250-ml flask was fitted with a stir bar, an addition funnel, and a condenser. The glassware setup was purged with argon, and 2.00 g of bis(butylthiol)-1,3-dithiol-2-thione was added to the flask with 60 ml of methanol. Sodium methoxide (25 ml, 0.5 M) was placed in the addition funnel, purged with argon, and then added drop-wise to the reaction mixture for about 15 minutes. This mixture was refluxed for 1 ½ hours and then cooled in an ice bath. Tetrabutylammonium bromide (4.14 g) was dissolved in 20 ml methanol, placed into the addition funnel, purged with argon, and added drop-wise. Then 0.76 g $NiCl_2 \bullet 6H_20$ in 60 ml of H_20 was added drop-wise over 45 minutes and the mixture was allowed to stir for 35 minutes. The argon purge was removed so that air could enter to partially oxidize the nickel complex to the zerovalent oxidation state. The volume of the mixture was then reduced on the rotary-evaporator. The solid was dissolved in acetone and filtered. Previous syntheses of the dye had caused suspicion that the iodine was causing problems with the reaction—a black tar was produced that was difficult to purify. This made us suspect the nickel wasn't fully oxidized and the iodine was not easily separated from the nickel complex. Because of this, the product was split into two portions. To one portion was added $FeCl_3$ dissolved in 20 ml acetone, and to the other portion was added 0.381 g of iodine in 20 mL acetone. Both mixtures were transferred to round-bottomed flasks, fitted with condensers and stirring rods, and were left to stir overnight in air to oxidize. The crystals were filtered from each mixture the next morning, and a UV-VIS-NIR spectra showed a strong absorbance band at around 1002 nm. The isolated products were re-crystallized twice using ethyl acetate and washed using a mixture of cold ethyl acetate and methanol. The ferric chloride was separated from the product more easily than the iodine (0.87 g, 49.01 % yield, m.p. 103°C).

Synthesis of tetrakis (2-methylbutylthio) bis(ethylene-1,2-dithiolene) nickel (0)

The above compound was prepared following the method of A. Charlton[2], with some modifications. The glassware was oven dried and then purged with argon. Bis(methylbutylthiol)-1,3-dithiol-2-thione (91.63 g) was placed in the flask with a magnetic stir bar and 49 ml methanol. This mixture was stirred for 20 minutes before 20 ml of sodium methoxide was added dropwise. The reaction mixture was refluxed for 1 ½ hours, and 3.32 g of tetrabutylammonium bromide in 16 ml of methanol was added dropwise. Nickel chloride hexahydrate (0.609 g) in 48 ml of H_20 was added dropwise to the clear, red solution. This resulted in a color change to dark brown and then brown-black. The mixture was stirred for ½ hour; then the argon purge was removed and the reaction mixture was exposed to air for 60 hours to allow the complex to oxidize to the zerovalent state. The reaction mixture was then filtered and the solvent was removed under vacuum. The dark residue was dissolved in acetone, 0.39 g of $FeCl_3$ in 16 ml acetone was added, and the mixture was stirred for 24 hours. The solvent was removed under vacuum, and the remaining solid and oil were partially dissolved in toluene (the oil was not soluble). When this was filtered, the black oil remained in the funnel until the suction was increased (this was necessary because not all the toluene went through). The filtrate was then put in a separatory funnel to separate the oil from the toluene; it did separate, but since the oil and the filtrate were the same color then rate of flow through the funnel was used to determine the change in substance. The solvent was then removed under vacuum; some would not evaporate so it was left to dry overnight and in the morning a dark solid was found. The solid was re-crystallized from ethyl acetate; later crops were re-crystallized using ethyl acetate/methanol (.20 g, 16.5% yield, 108.5°C).

Discussion

The procedure used for the original method included several steps between the $[TEA]_2$ $[Zn(dmit)_2]$ and the ether. These steps required several days, and column chromatography was necessary to purify the ether once it had been produced. A more recent article used the etherification process outlined above, which only requires a few hours and does not require chromatography, as the product is usually about 94-95% pure.

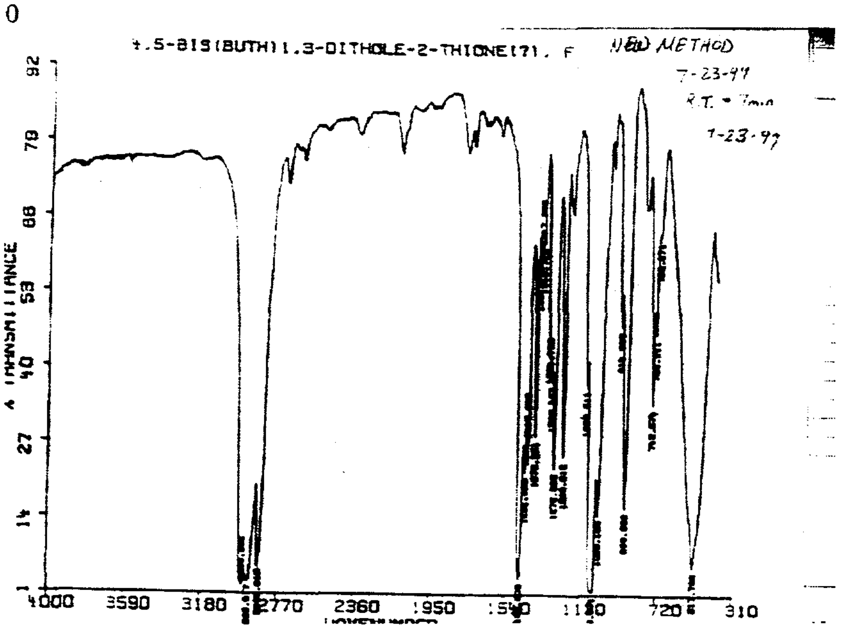

Fig. 7:. This graph of the infrared absorption of C4 ether was produced using Fourier Transform Infrared Spectrometry; the ether was produced by the new reaction method.

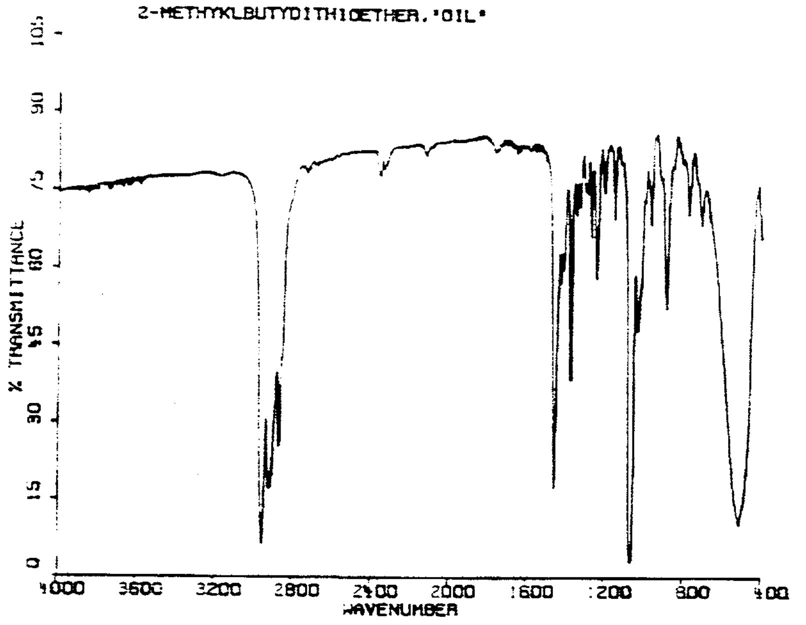

Fig. 8: The S2MeBu etherification produced two different products; the oil was determined to be the ether because the graph closely resembled other ether graphs produced by Fourier Transform Infrared Spectrometry analysis. The solid produced was insoluble in toluene, which suggested that it was not the product, and it was only slightly soluble in chloroform, so the IR spectrum showed very little transmittance.

The results from the nickel complexation obtained by following the original procedure described by A. Charlton et al.[2] were very poor. The product was very difficult to isolate. By making some modifications to the procedure described, the results were much better and the percent yields were higher than those reported. After the $NiCl_2 \bullet 6H_20$ was added and the mixture had stirred, the argon purge was removed before oxidation. The solid recovered from rotary evaporation was then oxidized using $FeCl_3$ instead of I_2, and the oxidation took place in air. No instantaneous color change was observed; rather, it took several hours and the Ni was always oxidized overnight. Results are shown below for the SC_4 and S2MeBu; the SC_4 results are also compared with other compounds in the same family (they differ in alkyl chains).

Functional group	M.P. (°C)	Literature Yield[2]	Yield	Purity
$-SC_4H_9$	103	15%	49%	99.3%
$-SC_5H_{11}$	97-98	15%	54%	98.8%
$-SC_7H_{15}$	82-83	27%	37%	99.2%
$-SC_8H_{17}$	73	31%	56%	99.3%
$-SCH_2CH^*(CH_3)CH_2(CH_3)$ "2MeBu"	108.5	--	13%	99.7%

Table 1: The –SC4 and the S2MeBu were synthesized, along with three other compounds in the same family as the –SC4. Purities were determined using high performance liquid chromatography.

Solubility Studies

Only the –SC4, -SC7, -SC8, and -S2MeBu were available for solubility studies in Merck E7. The solubility testing was performed using a simple "sedimentation" experiment[6]. Samples of the dyes were placed in E7; they were 0.50wt% and 1.0wt%. The samples were then heated to the LC clearing point and cooled to room temperature, at which point they were filtered through a 0.5 μm Teflon membrane to remove any undissolved dye and insoluble particulates. The samples were then checked periodically both visually and through inspection using microscopy to determine if any dye had precipitated.

X-group	λ_{max} E7	Solubility limit (E7)[6]
-PhOC$_9$	970 nm	<0.3%
-PhOC$_4$	970 nm	<=0.3%
-PhC$_4$	910 nm	>0.3%
-SC$_4$H$_9$	1020 nm	<0.5%
-SC$_7$H$_{15}$	1020 nm	>=0.5%
-SC$_8$H$_{17}$	1020 nm	>=0.5%
S2-MeBu	--	<0.5%

Table 2. The thioether compounds show much better absorption than the dyes with phenyl terminal groups previously synthesized—substituting a thioether group for the phenyl terminal group produces a bathochromic shift in the near-IR absorption band. The solubility limits of the thioether dyes have qualitatively been determined to be higher than those of the dyes with phenyl terminal groups. More quantitative analysis needs to be performed to determine the limits more precisely.

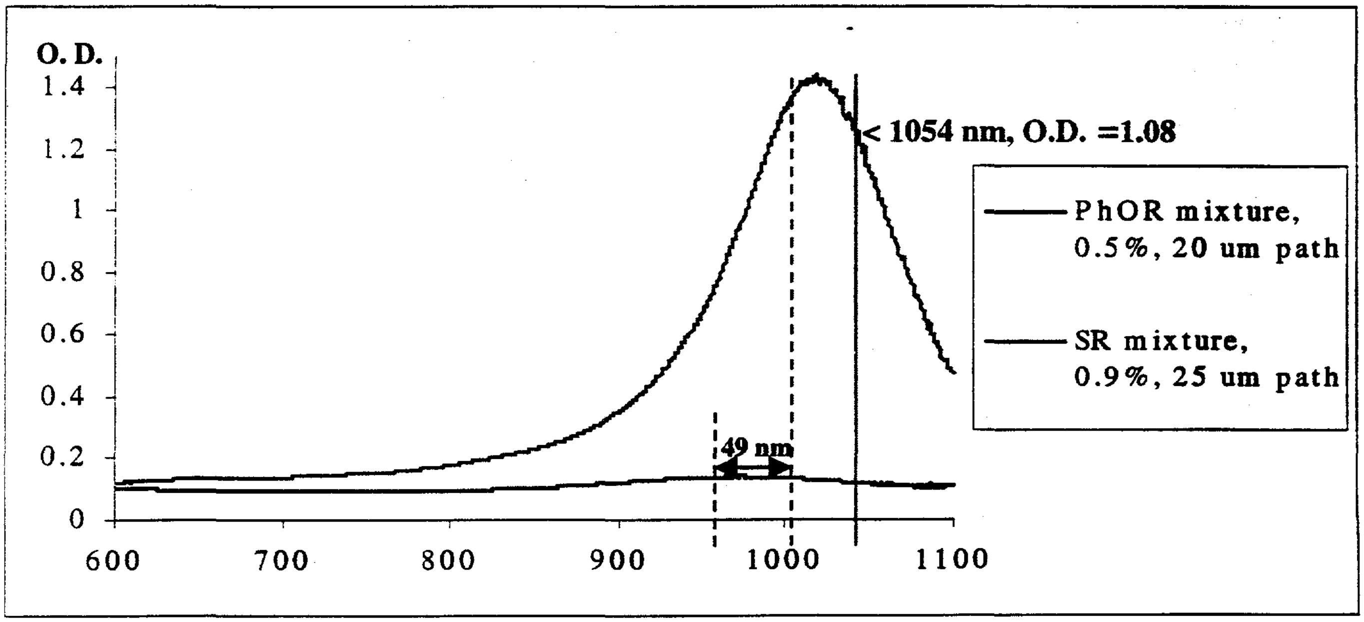

Fig. 9: These results were used to find the maximum absorbance of the dye mixtures in E7; the new dye mixture was compared with the old one. The results were obtained using LCPDI devices. Substitution of a thioether group for the alkoxyphenyl group produced a bathochromic shift of 49 nm. The results were taken using an HP 8453E-diode array spectrophotometer, incident beam polarized parallel to the cell alignment axis.

Mixtures of dyes have been shown to be more soluble in the liquid crystal host than any individual dye. Both the PhOR dyes and the –SR dyes are soluble individually at concentrations between 0.2 wt % and 0.5 wt %. A ternary mixture of three thioether dyes, -SC4, -SC7, and -SC8, is soluble in E7 at 0.9 wt% of dye. This is a significant improvement over the mixture of the PhOR dyes—the 1:1 mixture of PhOC9 and PhOC4 had a maximum solubility in E7 at 0.5 wt% of dye. The thioether mixture is almost twice as soluble—which suggests that improved solubility can be reached by using more dye components in the mixtures. The solubility is much higher than that of the phenyl dyes, but even more dye is needed in the LCPDI devices to meet the requirements for LCPDI deployment on OMEGA.

Fig. 10: The S2MeBu crystals viewed under polarizing microscope; magnified 100 times. The field of view is 250 μm.

The S2MeBu has very interesting properties in Merck E7. The very small black crystals are soluble at 0.5% indefinitely, at which concentration it shows normal characteristics of dyes placed in the E7 host. At 1.0 wt %, it is soluble for twelve to fourteen hours; however, the presence of the dye in E7 at that concentration causes an induced chiral nematic phase or cholesteric phase in the E7 host. This is a novel discovery—to the best of our knowledge, it is the first observation of mesophase chirality induced by a transition metal dithiolene. The chiral nematic phase was identified by the characteristic "fingerprint" optical texture. The helical structure of the chiral nematic phase causes the different color bands—the color is dependent on the position of the helix.

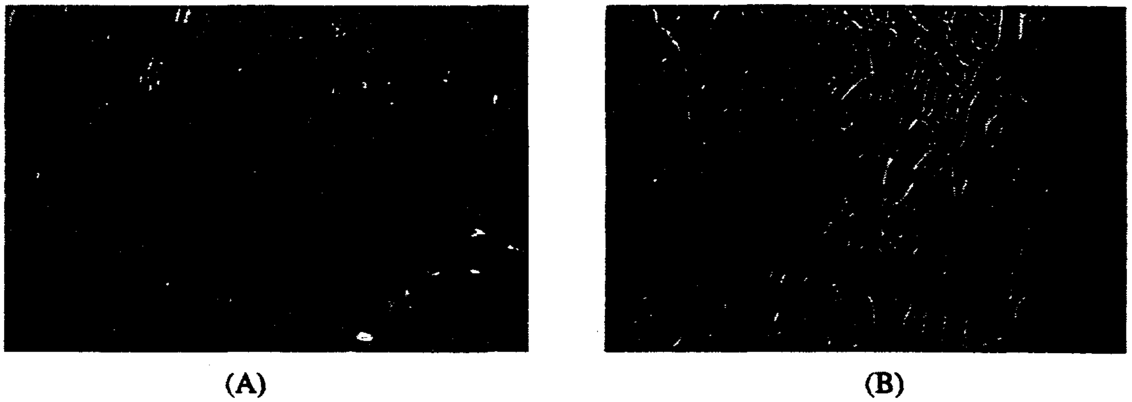

Fig 11: Effect of addition of S2MeBu dye to the nematic E7 host. (A) Pure E7 viewed under crossed polarizers, 100 x magnification. (B) E7 containing 1wt% of S2MeBu dye viewed under the same conditions. The "fingerprint" optical texture is a result of the induced chiral nematic phase.

Conclusion

Substitution of thioether groups for alkyl- or alkoxyphenyl substituents in nickel dithiolene dyes produces a bathochromic shift in the near-IR absorbance band. This means that the new alkylthio-substituted compounds are more efficient absorbers at 1054 nm; they are also more soluble in the LC host than the phenyl-substituted dyes previously synthesized (≈0.5% vs. ≈0.3%). Using multi-component dye mixtures improves overall solubility in the LCPDI and also enhances the performance of the LCPDI device. A ternary dye mixture of the three thioether dyes has an OD in the LCPDI device at 1054 nm of about 1.08. A binary dye mixture of the phenyl dyes has an OD at the same wavelength about a tenth as large. This leads to the conclusion that a mixture of 4 or more dyes will have an even better OD. To meet the requirements for LCPDI deployment on OMEGA, a mixture of more than three dyes is necessary—the OD needs to be 1.8-2. Nickel dithiolene compounds with chiral terminal groups form an induced cholesteric phase when added to an LC host—this is the first observation of mesophase chirality induced by a transition metal dithiolene.

References

---

1. Mercer, C.R.; Creath, K.; *Optical Letters*, **1994**, 19, 916-917.
2. Charlton, A.; Hill, C.A.S.; Underhill, A.E.; Malik, K.M.A.; Hursthouse, M.B.; Karaulov, A.I; Moller, J. *J. Mater. Chem.*, **1994**, 4(12), 1861-1866.
3. U.T. Mueller-Westerhoff and B. Vance, in "Comprehensive Coordination Chemistry" V2, pp 595-631, Pergamon Press, Sir Geoffrey Wilkinson, Editor.
4. C.E. A. Wainwright and A. E. Underhill, ***Mol. Cryst. Liq. Cryst.***, Vol 234, pp 193-198, 1993.
5. Svenstrup, N.; Rasmussen, K.M.; Hansen, T.K.; Becher, J. *Synthesis* **1994**, 809-812.
6. Irene Lippa, "Synthesis of Nickel Dithiolene Dyes and Analysis of Solubilities in a Nematic Liquid Crystal Host", LLE Summer High School Research Program, 1998.
7. Marshall, K.L. and Jacobs, S.D. Mol. Cryst. Liq. Cryst., 1988,159, 181-196.
8. Steven Corsello, "Computer-Aided Design and Modeling of Nickel Dithiolene Near-IR Dyes", LLE Summer High School Research Program, 1998.

Acknowledgments

I would like to thank my supervisor, Kenneth L. Marshall for the time he spent explaining the reactions and equipment. His help was invaluable. I would also like to thank the University of Rochester Laboratory for Laser Energetics, the High School Summer Research Program director Dr. R. Stephen Craxton, and the optical materials laboratory staff.

Characterization of inter-pulse noise and the signal to noise ratio in a Regenerative Amplifier

Michael J. Harvey

Advisor: Dr. Mark Skeldon

University of Rochester
Laboratory for Laser Energetics

Summer High School Research Program, 1999

1. Introduction

1.1 Research Objective

The OMEGA laser system at the University of Rochester's Laboratory for Laser Energetics consists of sixty beams on target at a wavelength of 351 nm (UV) and a total energy of 35 kJ. Pre-pulse noise exists in the system that can be detrimental to target performance. Although the noise is several orders of magnitude less than the signal, it has enough power to damage the target before the rest of the pulse arrives. This pre-pulse noise may originate in the system's *regenerative amplifiers* as the spontaneous emission of photons.

The term regen, or regenerative amplifier is associated with the process of amplifying an optical pulse. A regen is a multiple-pass amplifier into which a pulse is injected. After the optimal number of round trips through the cavity, a highly amplified infrared pulse is switched out of the system and sent to the OMEGA Laser Bay.

At this time, OMEGA scientists are on the verge of installing the new Aperture-Coupled Stripline pulse shaping system which changes the current front-end configuration of OMEGA. This raises some important new questions. How much energy is lost to the new pulse shaping system? And how does this affect the signal-to-noise ratio in the output of the regen? What affect does changing the injected power into a regen have on the output signal-to-noise ratio?

1.2 OMEGA. OR. and PGR

Fusion research is the current focus of LLE although constant research is done on advancements for OMEGA itself. The OMEGA system consists of four rooms: the Oscillator Room. the Pulse Generation Room. the Laser Bay, and the Target Bay (see figure 1).

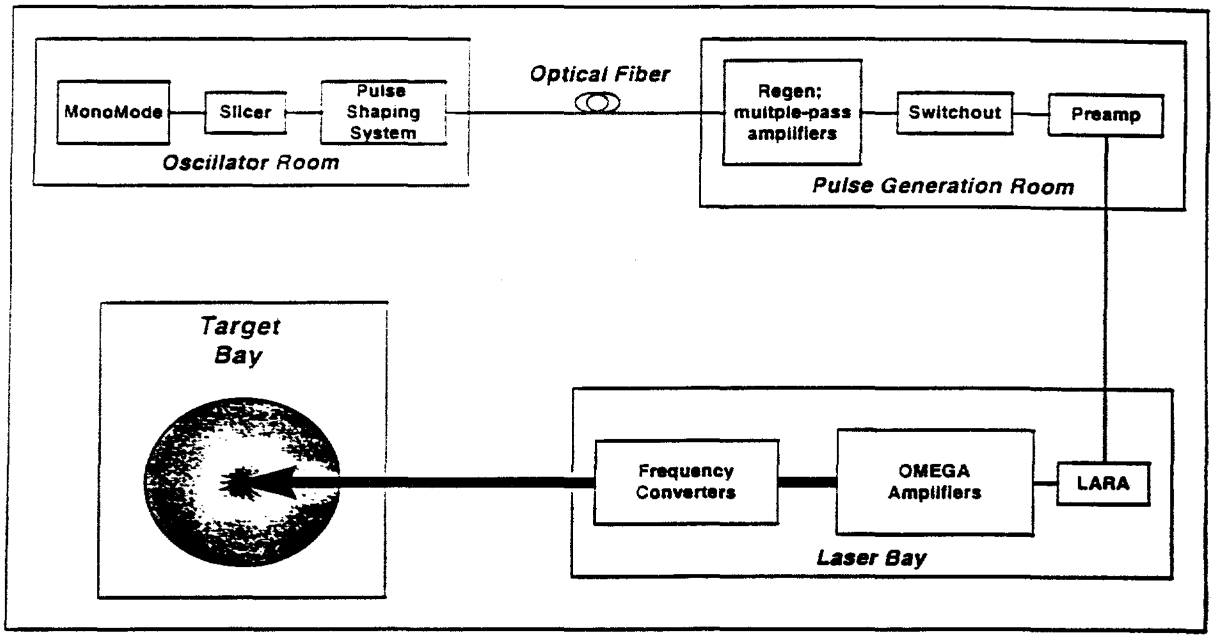

Figure 1. OMEGA Layout

The OMEGA system is seeded by a single laser pulse which originates in the Oscillator Room (OR). A diode pumped Mono Mode laser emits an infrared pulse train with one frequency, or mode at a wavelength of 1054 nm. The pulse is then temporally shaped by sending it through the pulse shaping modulators and is sent to PGR by way of optical fibers for additional energy boost.

The Pulse Generation Room (PGR) contains three regenerative amplifiers; one for each of three pulse shaping channels. These regens amplify the signals by seven orders of magnitude before they are sent to OMEGA for additional amplification.

Once in the Laser Bay, the main pulse is split into 60 separate beams and sent through a series of one-pass amplifiers and frequency converters. All sixty beams are brought to focus in the Target Bay. The targets are spheres which contain deuterium and tritium. When a shot is taken. the laser radiation causes the outside shell of the target to expand outward while the inner mixture implodes and reaches a very high temperature and density. This creates a fusion reaction, similar to the one that occurs in our own sun, and releases alpha particles and energy in the form of neutrons.

1.3 The diode-pumped Mono Mode laser

The Mono Mode laser is a very specialized laser designed to emit a laser beam with only one frequency component, or mode. This is accomplished by unidirectional propagation of the beam in the ring laser cavity and by controlling the cavity length of the laser. This cavity length is closely monitored and controlled (by adjusting the position of a Brewster prism) by feedback to a computer program. Regulating the cavity length forces the Mono Mode to lase at one frequency corresponding with the peak of the gain curve of the active medium (Nd:YLF). It is very important to operate with one mode. If the laser is allowed to run multi-mode, pulse shapes with many amplitude fluctuations due to mode beating can occur, and can be amplified past the damage thresholds for OMEGA optical components.

If the Mono Mode laser does not act as it is designed to act, it may lase at more than one frequency. These frequencies can beat together causing amplitude fluctuations on the optical pulse. When the Mono Mode is lasing with more than one mode, a frequency side band can be measured at a frequency that is equal to the distance between the two temporal modes in frequency space (see figure 2).

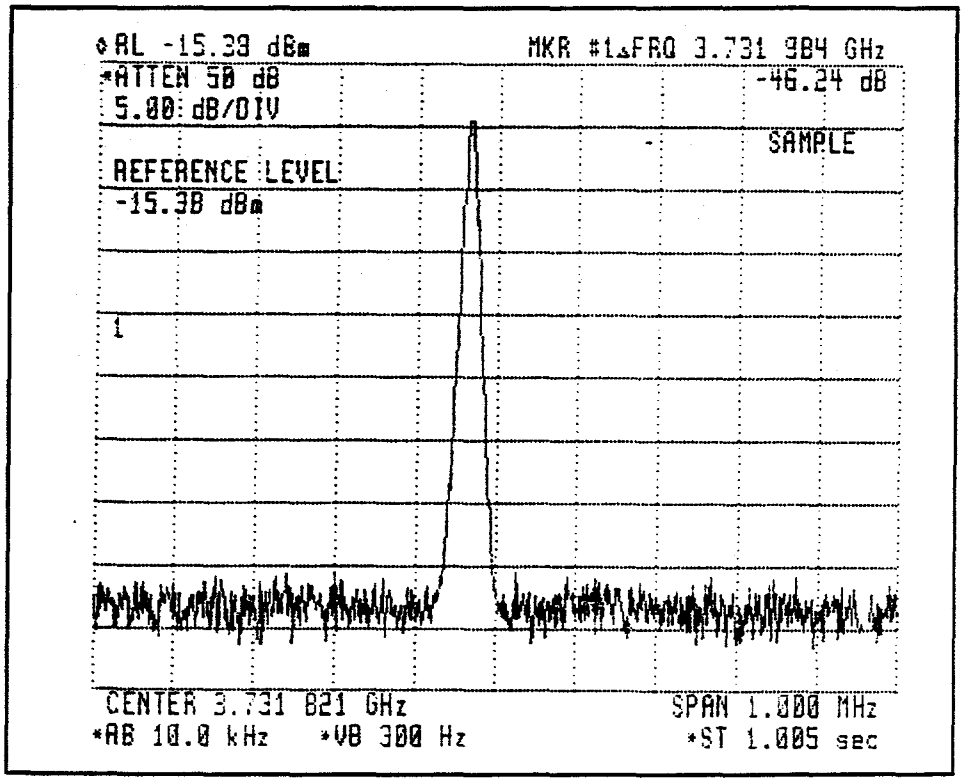

Figure 2. *Side band at 3.731 GHz is evidence of mode beating.*

The distance between laser cavity modes is equal to $\frac{c}{2L}$ where c is the speed of light and L is the the cavity length which we assume to be about 4 cm. We should see this side band appearing around 3.75 GHz. The spectral analysis of the Mono Mode shows the side band, as expected, at 3.731 GHz. Also, since we see no side band when the laser is running with one mode, we can assume that the frequency component which produced this side band is 40 dB down from the signal.

Although this is not the focus of our investigation, it verifies that noise due to mode beating does not contribute to the results of our experiment.

1.4 Current pulse shaping on OMEGA and the new ACSL system

Currently, pulse shaping for OMEGA is done in OR by a series of modulators driven by electrical waveform generators. The present system is large, difficult to monitor, and complicated. It requires its own small laser to trigger silicon switches on the waveform generators.

The Aperture Coupled Strip Line (ACSL) system is the upgrade that is in its final stages of approval for installation on OMEGA. This system is computer regulated and controlled and relies on electrical waveforms generated by the ACSLs. An entire pulse shaping channel is contained within four boxes. This system offers improved pulse predictability and a diagnostic of pulses straight out of the modulator boxes.

In all experiments the ACSL pulse shaping system was used to produce square optical pulses with variable pulse widths.

1.5 The Regenerative Amplifier

A regen is a multiple-pass amplifier consisting of a 100 percent reflective mirror, a partially reflective mirror, the gain medium, a pump source, and a Q-switch as shown in figure 3 (Skeldon).

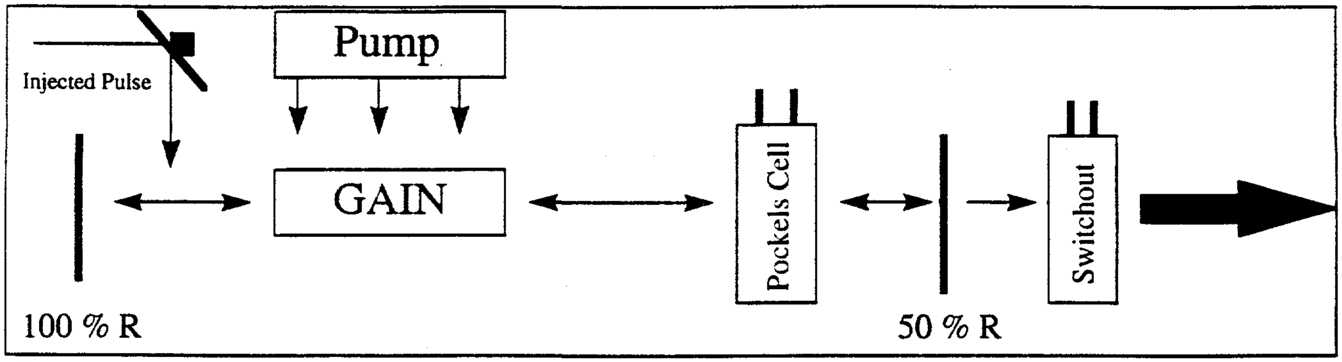

Figure 3. In this case, the Pockels Cell acts as a Q-switch by introducing loss into the cavity

The Gain medium of our regens is Nd:YLF. When pumped with photons from a flashlamp it builds up a gain curve, the peak of which is at 1054 nm. When the gain reaches its maximum, a pulse is injected into the regen cavity at time Q_1 (see figure 4.).

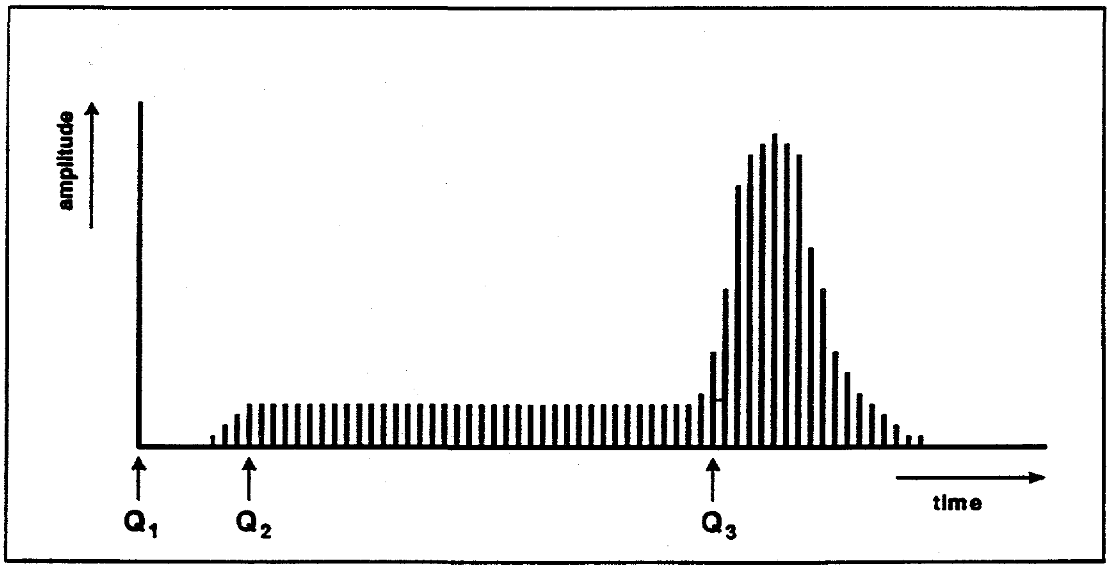

Figure 4. The regen pulse train

The amplification of the injected pulse is controlled inside the regen by a pair of pockels cells. At first, the pulse sees exponential gain, but at the point Q_2 loss is introduced into the cavity by the use of the pockels cells. A voltage is applied to a crystal within the pockels cell to change the transmission of the crystal/polarizer combination and clamp the energy of the pulses at a certain amplitude. Because the pulses oscillating through the cavity see no net gain, the laser rod stores energy. At the point Q_3 all voltage to the crystals is dropped allowing the pulses to experience gain. When this occurs, the laser rod transfers all of its stored energy into the optical field in the cavity (see figure 4).

It is at the peak of this *saturation regime* (after Q_3) that a pulse is switched out and sent through to the OMEGA amplifiers (Babushkin).

To ensure that the wavelength of the injected pulse matched the wavelength of the peak of the regen gain curve, output from the regen was also analyzed by a spectrometer. If the injected pulse does not match the peak of the regen gain curve it will not be amplified as effectively. First, pulses were injected into the regen and sent to a spectrometer to test the wavelength of the injected pulse. Then, the regen was allowed to build up from spontaneous noise and the gain curve of the regen was analyzed (see figure 5).

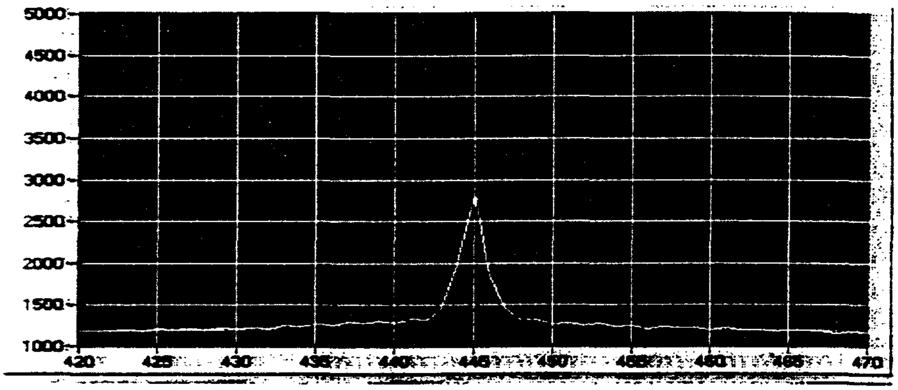

Spectrum of the seeded regen

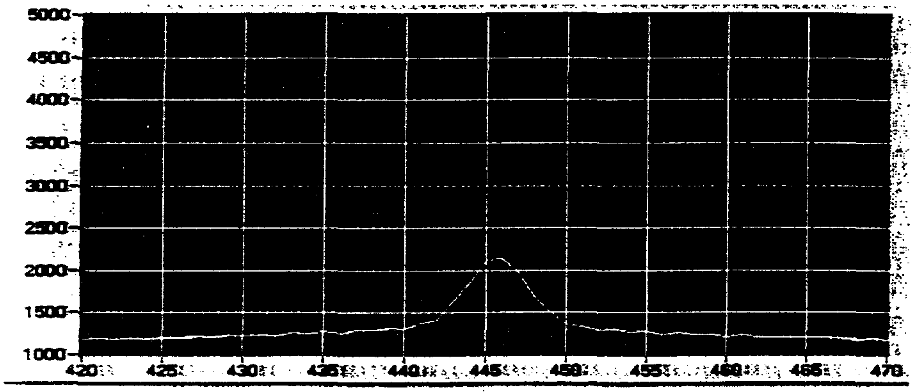

Spectrum of the unseeded regen

Figure 5. Notice that the injected signal is almost at the peak of the gain curve.
One Pixel ≈ 0.17 Å

2. Theory: signal-to-noise ratio

2.1 Amplification of optical pulses

The purpose of the regenerative amplifier is to amplify an injected optical pulse. A regen is very similar to a simple laser with the exception that the regen starts from an injected pulse instead of the spontaneous emission of photons. The pumped-up gain in the regen is able to amplify a pulse that passes through it due to its population inversion.

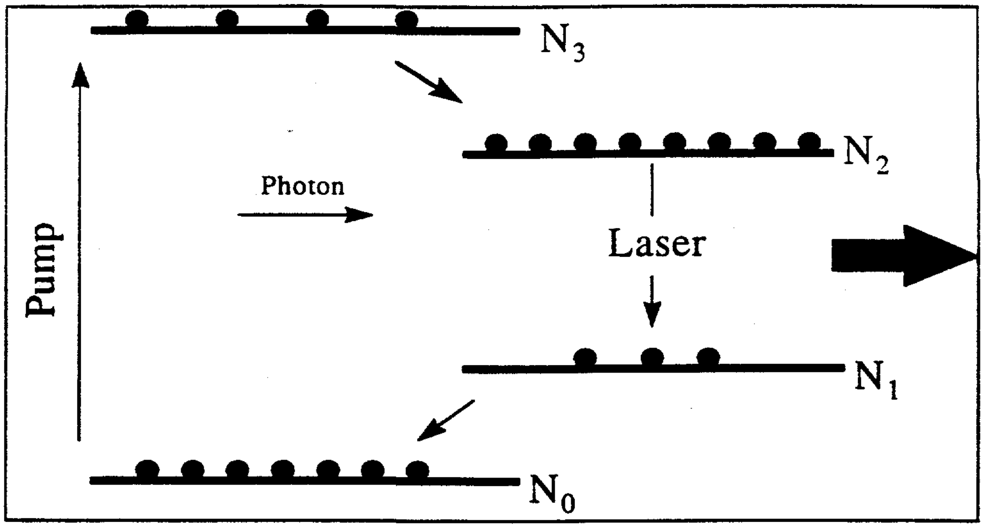

Figure 6. Population Inversion ($N_2 > N_1$)

A population inversion occurs when there are more excited atoms in the N_2 sublevel than in the N_1 sublevel as shown in figure 6 (Skeldon *et. al.*). The pump photons excite atoms into the highest energy level (N_3) where they stay for a short period of time before decaying to the N_2 sublevel. The excited atoms spend considerably more time (520 μs) in the N_2 sublevel while atoms decay out of the N_1 sublevel very quickly (20 ns). This is the population inversion. When a photon which is part of the injected pulse passes through the gain medium, it stimulates an atom to decay from the N_2 energy level to the N_1 energy level and emit a photon identical to the incident photon.. A theoretical equation has been developed to model the amplification of the signal and noise inside the regen cavity.

2.2 The Signal to Noise ratio

Lasers can be described by a set of equations known as the laser rate equations.
The equation

$$\frac{dP}{dt} = \gamma P + \frac{N_2}{N_2 - N_1} \gamma h \nu \Delta \nu + \gamma C P \qquad (1)$$

models the total evolution of the power (P) of the pulse in the regen (see Eq. 1).
In equation 1, P is the power of the pulse, γ is the gain coefficient, $1/C$ is the injected signal-to-noise ratio from the modulators, and $\Delta\nu$ is the gain bandwidth of the Nd:YLF

crystal. If we assume that $N_1 = 0$ then the population inversion factor

$$\frac{N_2}{N_2 - N_1} = \mu$$

equals one ($\mu = 1$).
The solution to the above equation(Yariv, 703) is given by

$$P(t)=\underset{\substack{\nearrow \\ \text{Amplified} \\ \text{Signal}}}{P_0e^{\gamma t}}+\underset{\substack{\uparrow \\ \text{Amplified} \\ \text{A.S.E. noise}}}{\mu h\nu\Delta\nu\left(e^{\gamma t}-1\right)}+\underset{\substack{\nwarrow \\ \text{Amplified Injected} \\ \text{Modulator Contrast}}}{CP_0e^{\gamma t}} \tag{2}$$

This function displays the power of the signal as a function of the time it spends in the amplifier. The first term is the amplified injected signal. The second term is the amplified spontaneous emission noise, and the third term is the amplified injected signal-to-noise ratio from the modulators. Thus, the signal-to-noise ratio at the output of the regen (Eq. 3) is

$$\boxed{\left(\frac{S}{N}\right)_{output}=\frac{P_0}{\mu\, h\, \nu\, \Delta\nu}\frac{G}{(G-1)+GCP_0} \qquad (3)}$$

2.3 Explanation of theory

The signal-to-noise ratio is defined as the ratio of the output signal to the output inter-pulse noise. The signal is simply the injected power multiplied by the gain constant $G \equiv \exp(\gamma t)$ where t is the time that the optical signal has spent in the amplifier. The sources of noise are more complicated to model. The term $h\nu\Delta\nu$ characterizes the spontaneous emission of photons, where $h\nu$ is the energy of a single photon and $\Delta\nu$ is the gain bandwidth of the Nd:YLF crystal which we assume to be 15Å. The term CP_0 characterizes the injected signal-to-noise ratio from the pulse-shaping modulators. C is the noise escaping through the modulator divided by the signal injected into the regen from the modulator. A small C implies large injected signal-to-noise ratio. When both noise terms are multiplied by the gain we arrive at the signal-to-noise ratio equation.

Because the signal to noise ratio depends on both ASE noise and injected signal-to-noise, we see a curvature to the data that was not previously modeled by any existing theory. If we divide equation 3 through by the gain constant, G, while assuming $\mu = 1$, we obtain for large $G > 1$...

$$\left(\frac{S}{N}\right)_{out} = \frac{P}{h\nu\Delta\nu + CP} \tag{4}$$

Equation 4 is a simpler way to represent the behavior of the data.

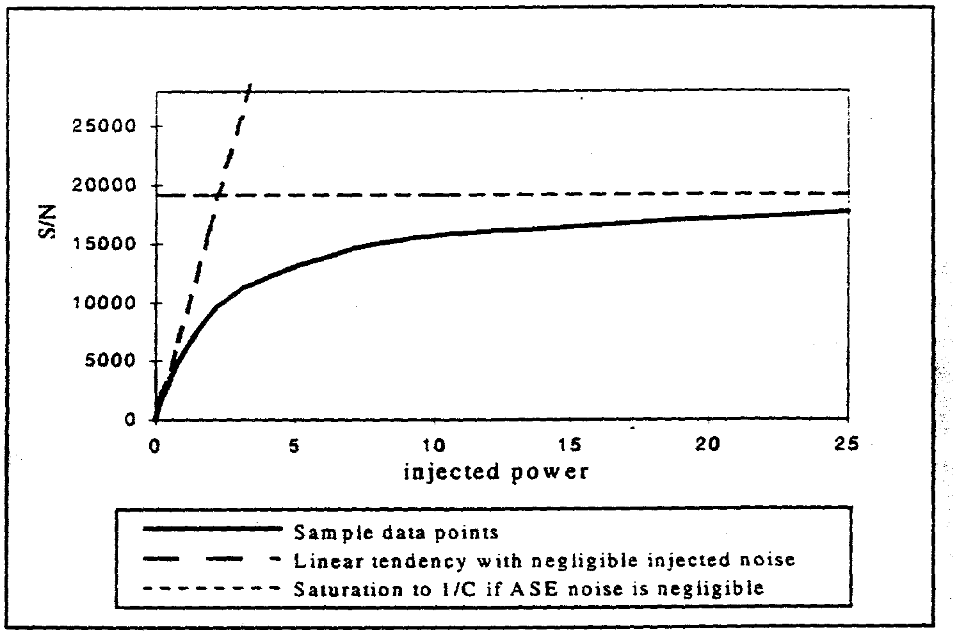

Figure 7. Explanation of theory.

As seen in figure 7, if the ASE noise ($h\nu\Delta\nu$). is negligible the data will saturate to the line 1/C. The inverse is also true; if the injected contrast (CP_0) is negligible we see the data following the linear trend $P_0 / h\nu\Delta\nu$. When these two factors are combined they produce the curvature seen in the data.

3. Experimental Setup

3.1 Oscillator Development Lab

The Oscillator Development Lab(ODL) is very similar to OR and PGR. It contains a Mono Mode laser identical to the one in OR and regen similar to those in PGR, figure 8. In ODL the ACSL pulse shaping system is installed and was used in all experiments.

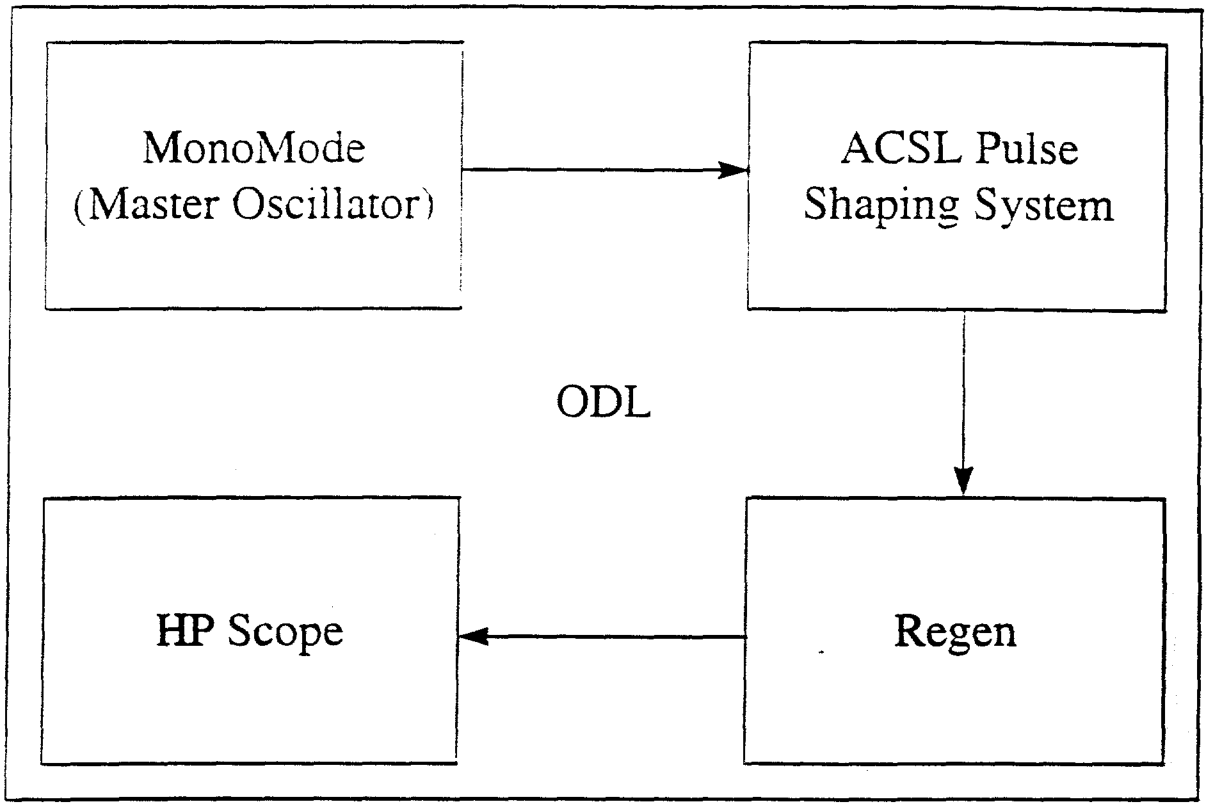

Figure 8. ODL Setup

The Mono Mode emits a train of Gaussian-shaped pulses with an approximate width of 200 ns (full width half max). One of these pulses is switched out and sent to the ACSL modulators where a shorter. square pulse is switched out from the peak. The pulse lengths used were 1.5. 3. or 6 nano-seconds in all experiments.

3.2 Injected energy / Peak Voltage Calibration

In order to determine the energy injected into the regen a calibration was done. Injected energy is gradually lowered by rotating a half wave plate / polarizer combination placed between the Mono Mode and the fiber coupler to the ACSL. The peak voltage of a detector sampling the 10 ns square pulse (at 5 Hz) is observed on an HP oscilloscope and recorded while the energy injected into the regen is recorded using an energy meter. Injected energy versus peak voltage can be plotted on the same graph. A least squares fit is done on the data to produce a linear calibration between the two scales, figure 9. This allows us to measure the injected energy into the regen by observing the peak voltage of the detector.

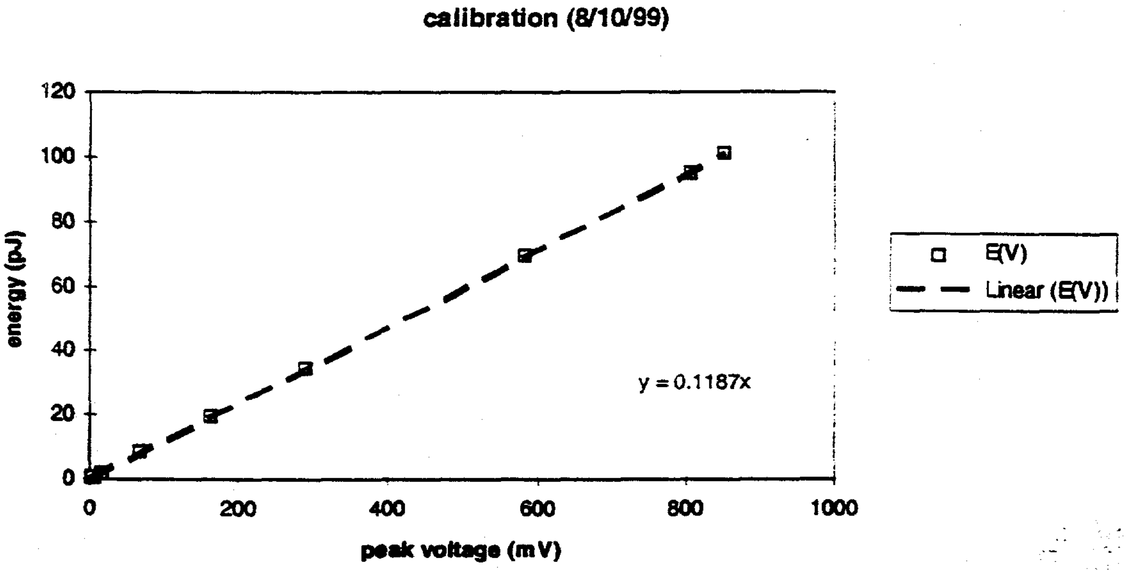

Figure 9. Calibration data

3.3 signal-to-noise Ratio experimental procedure

After a pulse is shaped (at 300 Hz) in the ACSL modulators, it is injected into the regenerative amplifier. The switched-out pulse is sent, in this case, to a Hewlett Packard Oscilloscope. Data was taken on pulses switched out of the *linear* (clamped) portion of the pulse train as well as the saturation regime of the pulse train.

Amplitude within the cavity is controlled because of the clamping affect of the pockels cells. Lowering injected energy only increases the build up time, the distance between Q_1 and Q_2, but doesn't affect the amplitude of the rest of the pulse train. For this reason, the pulse train has the same shape and amplitude regardless of the injected energy.

The timing of the switch-out can be adjusted so that one full pulse is allowed to escape the regen. The amplitude of this pulse is recorded. The timing can also be adjusted about 10 nano-seconds backwards in time to let the noise between pulses exit the regen, (see figure 10). As the injected energy is lowered by rotating the half-wave plate, the average voltage of the noise (V_{avg}) is recorded over a 5.0 nano-second window between pulses.

The ratio of the signal to this inter-pulse noise is plotted as a function of injected energy, and the theoretical function is matched to the data points to calculate values for both the ASE noise and the injected signal-to-noise.

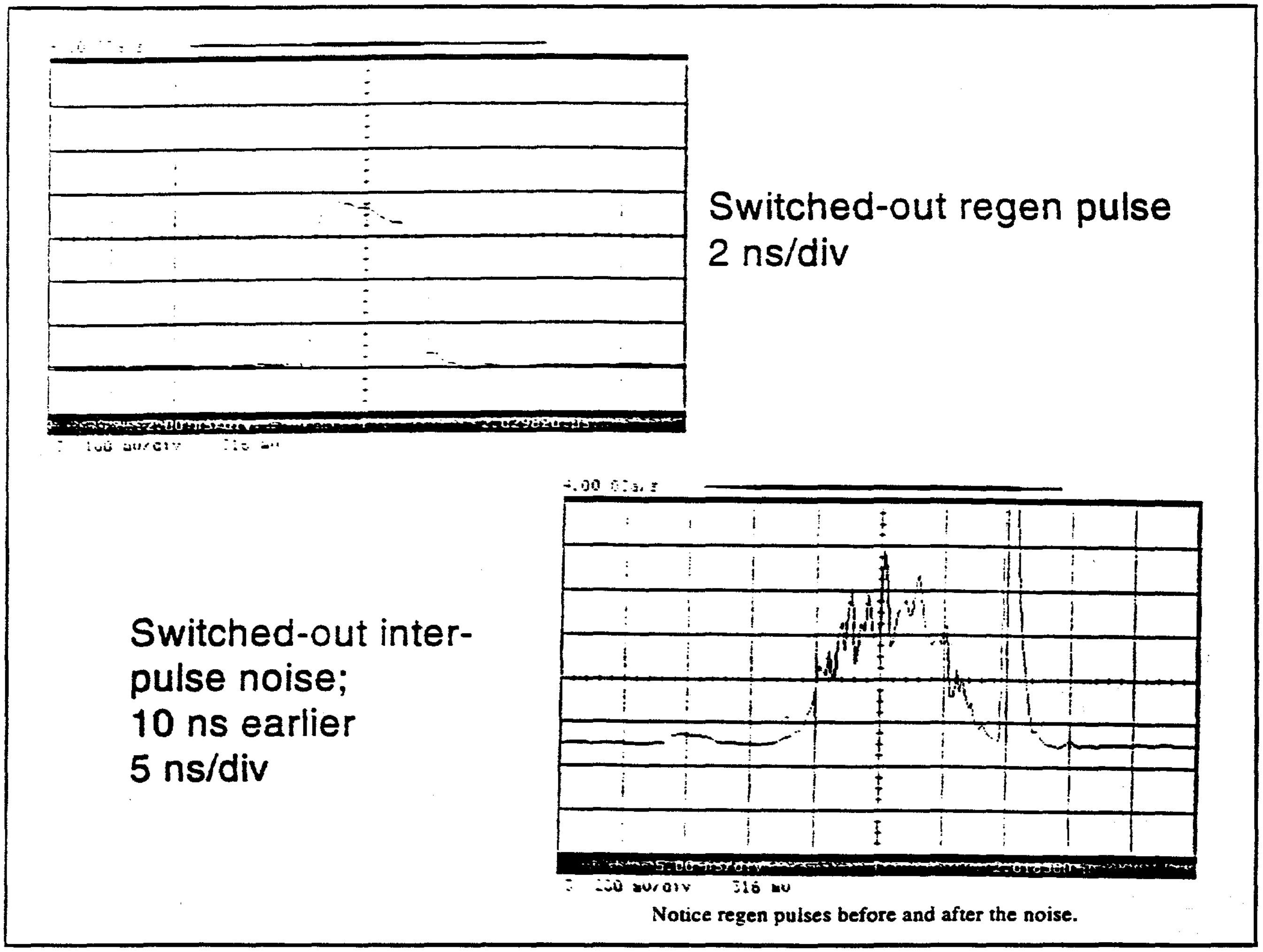

Notice regen pulses before and after the noise.

Figure 10. Switched out pulse/ inter-pulse noise.

4. Data

4.1 Repeatability

In order to insure that the data is repeatable many sets of data were taken in both the saturated and linear regimes. One and a half, three, and six nano-second pulse lengths were used in the experiments. Data was taken on seven different days and up to five sets of data were taken on each day.

4.2 Calculations

To validate the experimental data. an estimated value was calculated for the hνΔν term in equation 4…

$$h\nu = \frac{hc}{\lambda} = \frac{(6.626\times10^{-34}\,J\cdot s)\cdot(3\times10^{8}\,m/s)}{1.054\times10^{-6}\,m} = 1.886\times10^{-20}\,J$$

$$\Delta\nu = 1.5\,\overset{\circ}{A} = 1.5(3\times10^{10}\,s^{-1}) = 4.5\times10^{11}\,s^{-1}$$

$$h\nu\Delta\nu = 8.487\times10^{-8}\,W$$

Amplified spontaneous emission noise should remain somewhat constant in our regen. Therefore, we gage the validity of our measurements by the hνΔν values that we obtain by fitting the theoretical function to each set of data we take.

4.3 Experimental data.

When the experiment was first begun, data was taken with one pulse-shaping modulator. Because some noise escaped the modulator and was injected into the regen cavity, a curved trend in the data was observed (see figure 11, top). Because classical theory predicts the output signal-to-noise ratio of a regen to be linear, we added another modulator to cut down on injected noise. By increasing the injected modulator contrast, we decreased the CP_0 term and the behavior of the data became more linear as expected (see figure 11, bottom).

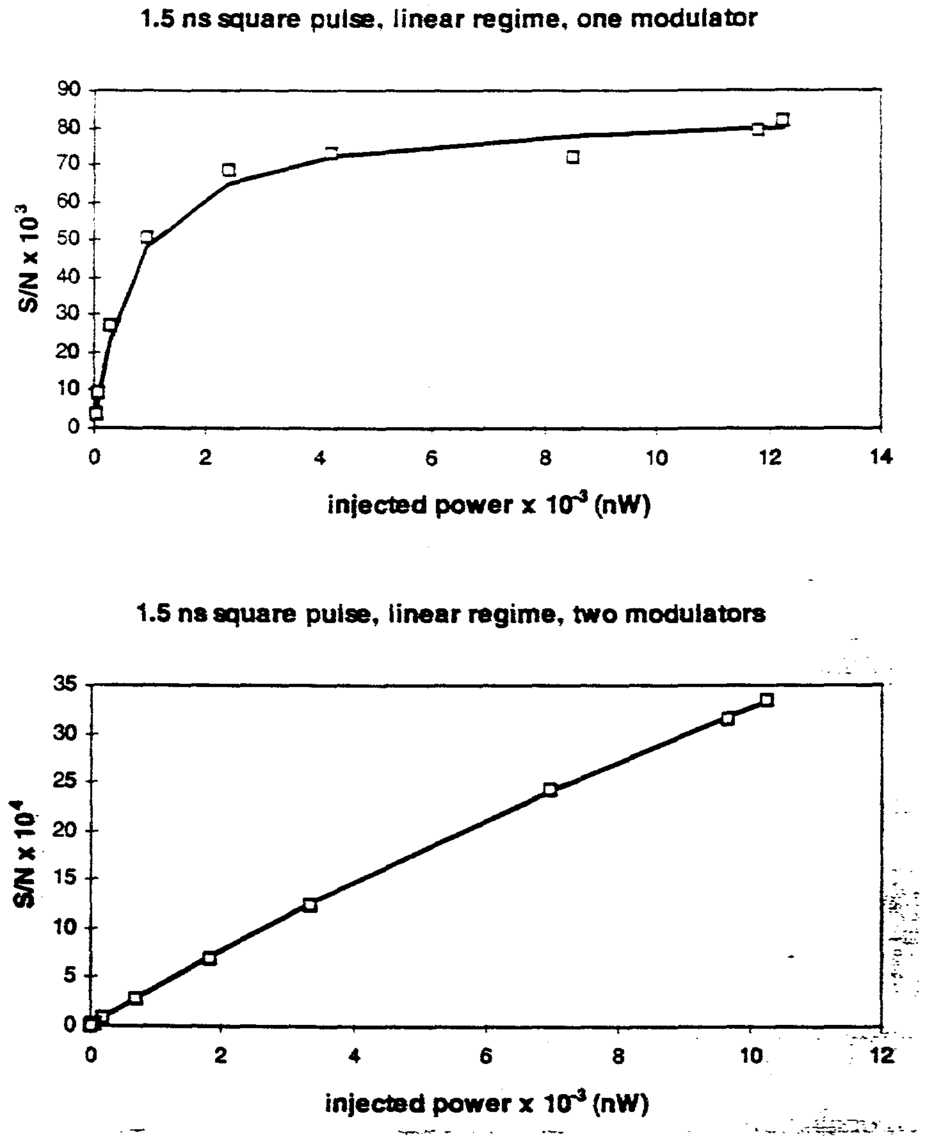

$$\left(\frac{S}{N}\right)_{out} = \frac{P}{h\nu\Delta\nu + CP}$$

Measured:

$h\nu\Delta\nu = 84\,nW$

$C = 1.19 \times 10^{-4}$

Measured:

$h\nu\Delta\nu = 24.9\,nW$

$C = 5.47 \times 10^{-7}$

Theoretical:

$h\nu\Delta\nu = 85\,nW$

Figure 11. Data sets show similar values for hvΔv. A more linear behavior is seen with two modulators.

In both cases, the hvΔv values were within an order of magnitude of each other and we may assume that our experimental data is valid.

Data was taken in the saturation regime of the regen pulse train to investigate the behavior of noise when peak amplitude is not clamped (see figure 12). This is of interest to OMEGA because pulses in the OMEGA system are switched-out from the saturation regime of the pulse train.

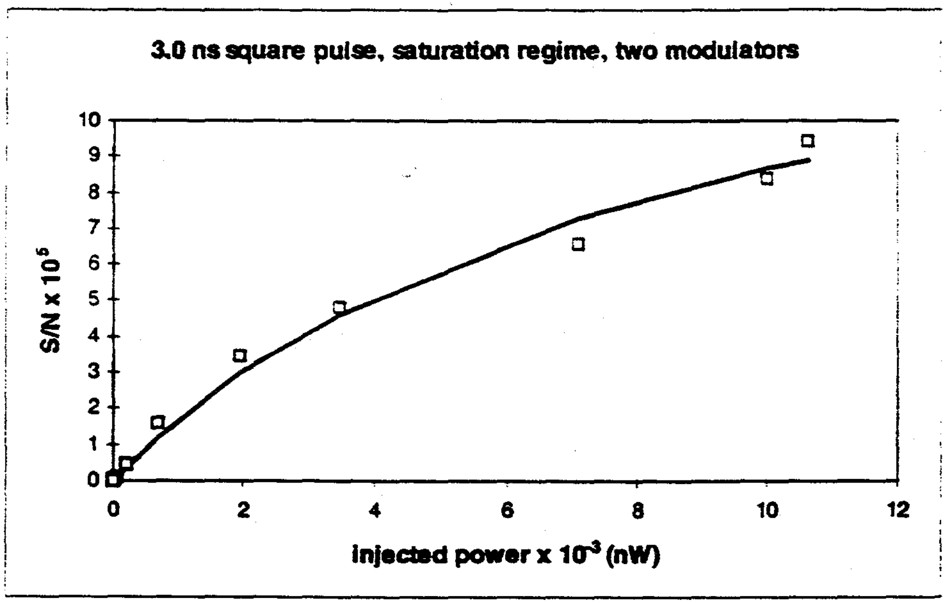

$$h\nu\Delta\nu = 5.32\,nW$$

Figure 12. Data from the saturation regime of the regen pulse train.

Although the hvΔv value for the data from the saturation regime is less than the same values from the linear regime, all three are within an order of magnitude and assumed to be valid.

5. Conclusion and Acknowledgments

5.1 The Signal-to-Noise ratio of a regenerative amplifier has been modeled.

The theoretical equation

$$\left(\frac{S}{N}\right)_{out} = \frac{P}{h\nu\Delta\nu + CP}$$

models the ratio in the regens differently than classical descriptions of signal-to-noise ratio. As a result of our own research, we added the second term which contributes to the noise and models the injected modulator contrast. The answer to increased signal-to-noise in OMEGA's regens is not only to increase injected energy, but also to increase the modulator contrast.

5.2 Acknowledgments

I would like to thank the entire staff of the Laboratory for Laser Energetics for making this experience such a success for every student in the program this summer.

I would also like to thank Dr. R. S. Craxton for running and supervising the program.

Many thanks to Dr. Andrey Okishev for his help with the Mono Mode laser.

Dr. Andrei Babushkin made my work with the regens possible because of his excellent knowledge, expertise, and willingness to help me this summer.

The person to whom I owe the greatest debt of thanks is my primary advisor, Dr. Mark D. Skeldon. Dr. Skeldon spent countless hours over the past eight weeks explaining the concepts of laser fusion and optics to me. His guidance has given me an insight into the field, sparked my curiosity, and influenced my decision of future plans.

6. References

Babushkin, Andrei. Conversation. July, 1999.

Skeldon, Mark D. Conversation. July, 1999.

Skeldon, M. D., A. Babushkin, W. Bittle, A. V. Okishev, and W. Seka, "Modeling the Temporal-Pulse-Shape Dynamics of an Actively Stabilized Regenerative Amplifier." *IEEE J. Quantum Electron.*, vol. 34, pp. 286-291, 1998.

Yariv, Amnon. Optical Electronics, Fourth Edition. New York: Holt, Rinehart and Winston, 1991. pp. 701-703.

Comparing Opacity Data Groups with a Java-Based GUI Solution

Peter W. Hopkins

Advisor: Dr. R. S. Craxton

Laboratory for Laser Energetics
University of Rochester

Summer High School Academic Research Program
1999

1. Introduction

One important aspect of research on the OMEGA laser system is the computer modeling of targets. It is critical to be able to predict the behavior of a target when it is hit by the laser. An integral part of these simulations is opacity data, which provides information on how radiation will be absorbed by targets. Recently an updated database of opacity was received at the Lab, but there was no easy way to determine the differences between the two databases, new and old. The solution outlined in this paper was created to address that problem.

2. Opacity

Opacity is a value, given in 1/cm, corresponding to the inverse of the distance that a photon of a specific energy will travel through a material of a particular temperature and density before it is absorbed by an electron. Opacity data is used primarily in modeling the behavior of radiation inside an OMEGA target. Hydrocodes run at LLE interpret tables of opacity data and generate information about the state of the target at specified times.

2.1 Opacity Data in Detail

The opacity database used at the Laboratory for Laser Energetics was calculated at Los Alamos National Laboratory.[1] Two versions of these files exist: a legacy version from the late 1970s and an updated version received in early 1999. The older files have 2 000 data points per temperature-density point and will hereafter be referred to as the 2000-group files. The new files, with 14 900 points per graph, will be called the 14900-group.

"Native" opacity data is on a non-standard scale that normalizes the data for simpler inclusion into the data files. The X axis of the data is measured in $\frac{h\nu}{kT}$. By dividing by the temperature (T), the X values for all temperature points can be fixed at a range of 0.01–20 for the 2000-group and 0.00125–30 000 for the 14900-group. The Y values have been altered as well. They are given as the result of the function $\mathrm{D}(u) = \left(\frac{3\sqrt{3}M_e ckT}{16he^2}\right)\frac{u^3}{1-e^{-u}}\sigma'$. This function, in which u is given in $\frac{h\nu}{kT}$ and σ' is in $\mathrm{cm}^2/\mathrm{ion}$, reduces the range of Y values. D(u) values were specially packed in the 2000-group, saving space by taking advantage of the altered range. 14900-group files use a standard numerical representation for the data, but are still stored as D(u) values.

Besides formatting, which is invisible to the average user of the data, the two versions of the opacity files differ in three other key ways. The first, as noted above, is in resolution. The 14900-group data has more than seven times the number of points per graph than the 2000-group data. The 14900-group can thus describe the structure of the graph in greater detail than is available in the 2000-group. Secondly, the 14900-group has data over a much wider domain than the 2000-group. In most cases, the 2000-group data contains all the important structure of the graph. In some special cases, however, especially with elements of larger atomic number such as titanium, relevant features such as the K-edge of the graph are lost in the 2000-group because of its smaller domain. These features are available in the 14900-group data, however. The third difference between the two is their treatment of scattering data, which is included as part of the 2000-group but is separate in the 14900-group. (Scattering refers to the deflection rather than absorption of an incoming photon due to collisions with electrons.) Because most of the calculations done at LLE involve the opacity data but not the scattering data, the scattering data had to be subtracted from the 2000-group to make the data usable. Most of the time, this technique worked acceptably, but in some circumstances the scattering was so much greater than the opacity that clearly inaccurate results were obtained..

These three differences are summarized in the graph of opacity vs. photon energy below. Note how the 14900-group is able to resolve a small peak in the graph that does not show up in the 2000-group. The 2000-group "drops out" near the end when the subtraction of scattering dominates the opacity. Finally, the 14900-group continues for a significant amount, although in this specific graph the greater domain does not show any significant structure.

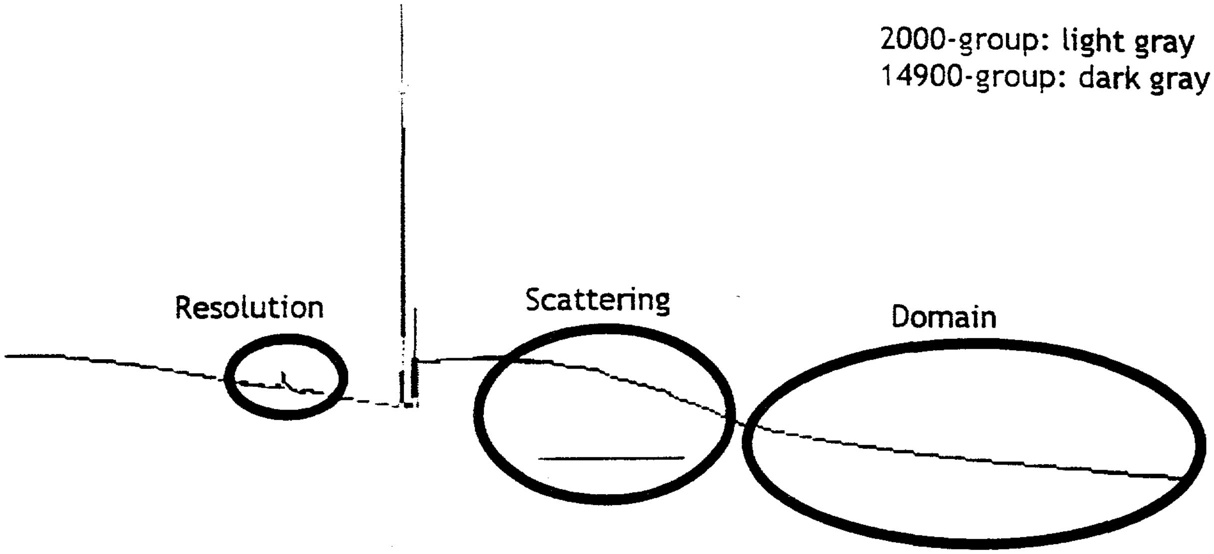

Carbon. 1000eV. 0.0787g/cc

3. Compression

The opacity database. because of its size. had to be compressed to be more readily stored on the server and transmitted over the network. Although extremely accurate data is required for the computer modeling—and the original files are still available on the DEC Alpha for that purpose—the same is not true for data shown in the Java viewer. which is geared towards human-interpreted display. Therefore a lossy compression technique was developed to maintain all of the graph's perceivable structure while reducing the file sizes significantly.

The compression algorithm operates in O(n) time to eliminate all non-structural points; that is, if a line can be drawn between two points such that all points in between lie within a small threshold of the line. those intervening points are non-structural and may safely be removed. The value of 1% was chosen. somewhat arbitrarily, for the threshold. This algorithm yielded a rough average of 20-to-1 compression when applied to the entire database.

3.1 Details of the Algorithm

The compression algorithm operates on a per-graph basis. By compressing each individual graph, the opacity file as a whole is reduced in size. While a more complex algorithm could be developed to share data among graphs of similar composition, the results achieved by the simpler algorithm are acceptable.

The principle behind the compression algorithm developed is that an opacity graph of 14900 or 2000 points can be accurately drawn with fewer points connected together by lines. The heart of the algorithm, then, is deciding which points in the original graph to keep in the compressed version, and which can be safely removed. In areas of great structure the algorithm fails to achieve any compression, but in areas of little structure the compression factor is quite dramatic. In testing of the algorithm, a 14900-group graph with little structure (Silicon, 200eV, eta=-1) was compressed to fewer than 100 points while maintaining a 1% margin of error relative to the original graph. Naturally, in graphs with more structure the compression ratio is less.

The algorithm works by saving a start point and iterating through the points after it. If a point is reached such that a line drawn between the start point and the current point does not correctly represent all of the points between with a 1% tolerance, the start point is saved to the file and a new start point is chosen such that a line drawn between the old start point and the new one would correctly describe the points between. This process is repeated until the end of the graph is reached.

A concern when developing this algorithm was the efficiency of checking each in-between point against each new line. The solution to this is to keep track of two lines of maximum and minimum so that new points need only be checked against these lines for validity rather than against every point. These lines intersect at the start point and form a cone such that a line drawn from the start point that was within the bounds of the cone would be acceptable for every point included in the cone up to that point. Every time a new point was considered, its maximum and minimum allowed values were calculated from the tolerance, forming a cone that included the start point and the current point. The intersection of this cone with the master cone generates the new master cone that can represent all points up to and including the current point. If the two cones do not intersect, a new start point must be chosen.

3.2 File Size and Structure

This algorithm is straightforward and operates by eliminating points that are not necessary to retain the entire structure of the graph. It works extremely well in areas of straight lines and gentle curves, but fails to compress areas of high structure. There is no inherent consequence to using the compression, though, because the worst-case file size is identical to the original file size. The original data uses 64 bits per Y value but does not have to record the X value at every point because the X values are standardized across graphs. The compressed file must record the X values as well as Y values because it does not keep every point and therefore has to record completely each point. Each value is represented in the compressed file with only 32 bits because the loss in precision is negligible compared to a 1% tolerance already assumed.

Further optimizations could be made to the compression algorithm. X values could be stored as 16-bit integers, corresponding to the already known X values (i.e.: X value of 1 in the compressed data maps to 0.00125 in the case of the 14900-group). This would net roughly a 25% reduction in file size as it would store only 48 bits per point rather than the current 64 bits per point. This relatively simple optimization was not implemented, however, because of difficulties in reading integer values written out by the FORTRAN compression program in the Java graph viewer. Floating point values, however, translated without a hitch. A more complicated optimization could fit parabolic curves to the graph rather than lines, as the algorithm does now. This could reduce the number of points because a single curve could replace several lines, especially in areas of high structure where the graph is more curvy than linear. This modification was not attempted due to time constraints in development.

4. Java Viewer

The purpose of the Java viewer is to provide a fast and flexible way to study and compare data from the 14900- and 2000-group data sets at all available element, temperature, and degeneracy points. The interface is designed to be functional and intuitive, and the program's feature set is easily extendible.

4.1 Interface and Capabilities

The Java viewer's interface is divided into five functional areas. Three are input areas that manipulate the two other areas, which are output areas.

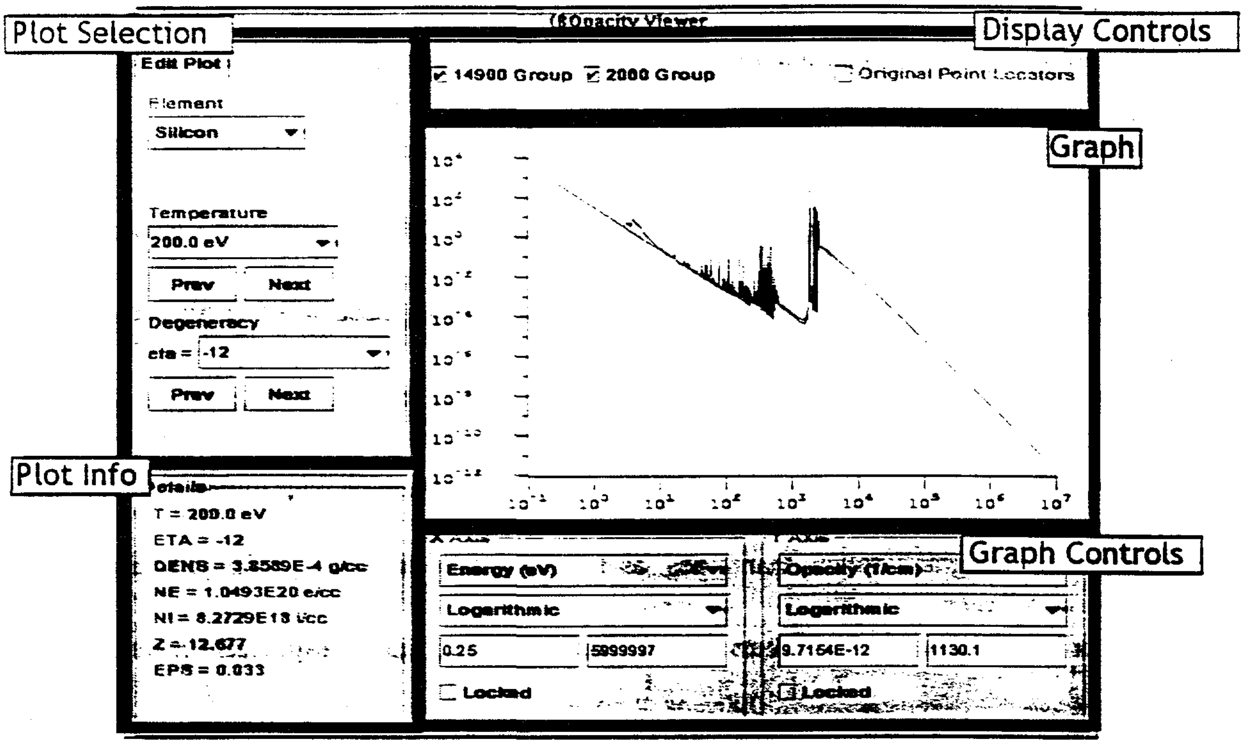

☑ 14900 Group ☑ 2000 Group ☐ Original Point Locators

Element: Silicon

Temperature: 200.0 eV

Degeneracy: eta = -12

T = 200.0 eV
ETA = -12
DENS = 3.8589E-4 g/cc
NE = 1.0493E20 e/cc
NI = 8.2729E18 i/cc
Z = 12.677
EPS = 0.033

X Axis: Energy (eV); Logarithmic; 0.25; 5999997; ☐ Locked

Y Axis: Opacity (1/cm); Logarithmic; 9.7154E-12; 1130.1; ☐ Locked

First of the input areas is the plot selection area, located in the upper left of the window. Three popup menus control the three variables for selecting a plot: element, temperature, and degeneracy. Of these, the latter two are combinations menu/text field, allowing the user to choose a value from the list or input his own. Inputs that are not available in the database are matched to the closest value.

The second input area is located above the graph and controls what is displayed in the graph. It has checkboxes corresponding to the 14900-group and the 2000-group, as well as an "Original Point Locators" option. If a group checkbox is "grayed out" or dim, it means that data for that group is not available for the selected element, temperature, and degeneracy point. The labels for these checkboxes are color-coded to match the colors of the graphs in the graph area. Original point locators are only available when the x unit is h/kT. When this option is selected, light red and blue vertical lines are drawn on the graph at every point in the original data. This feature is useful for diagnosing differences within the data due to sampling rate.

The third input area is below the graph and controls how data is displayed in the graph. For each axis, it offers a choice of several units and either linear or logarithmic scaling. Below these options the user can view and modify the minimum and maximum values for each axis. If an axis is designated "Locked" its range will stay fixed when moving among elements, temperatures, and degeneracies. Changing the units or the scaling will reset all of the axis back to the default best-fit for the entire graph.

Of the output areas, the first is located below the plot selection area and gives useful information about the selected element, temperature, and degeneracy, including the mass density and the average number of free electrons per atom.

The second output area, and the focus of the program, is the graph. This area displays the plots selected in the first two input areas in the form chosen from the third input area. 14900-group data is always drawn in red, and 2000-group data is always drawn in blue. The graph will always try to present the data using the most logical scales on the X and Y axis. Zooming in on an area of interest can be accomplished by clicking and dragging on the graph. The two vertical green lines define the boundaries of the area. To zoom out, simply double-click on the graph.

4.2 Systems Overview

The opacity viewer is a Java application, which means that it requires a Java Virtual Machine to be installed on the client computer but, unlike an applet, it runs outside of a web browser. To get to the opacity data, the application must be able to access the /opacity directory over the NFS network. It has been tested successfully on Solaris workstations, but has not been tested yet on the Windows machines at the Laboratory. Getting the program to work on these computers is the next immediate step in implementing the Java opacity viewer.

5. Notable Findings

The main advantage of having an interactive viewer for the opacity data is that differences between the 2000- and 14900-group data sets can be easily found. This capability will help ease the transition from the 2000-group to the 14900-group in LLE.

In general, the 14900-group graphs have significantly more structure than the 2000-group graphs, for two major reasons noted before. First, over the same domain, 14900-group graphs have a higher sampling rate, up to eight times higher than the rate of the 2000-group graphs. This means that 14900-group graphs better resolve spikes that are only mild plateaus in the 2000-group graphs. Secondly, the 14900-group data has a greater domain, with X values from 0.00125 to 30 000, rather than 0.01 to 20 like the 2000-group. In most cases, all significant structure is found in both data sets, but for elements of larger atomic number and at certain temperatures and densities there is meaningful information past 20 on the X axis.

Additionally, the 14900-group seems to contain some structures that are not found in the

2000-group. This is partially because of sampling rate but also speaks to a difference in the theoretical model used to generate the database. For example, the notched peak shown below is seen in other 14900-group graphs but not in 2000-group graphs.

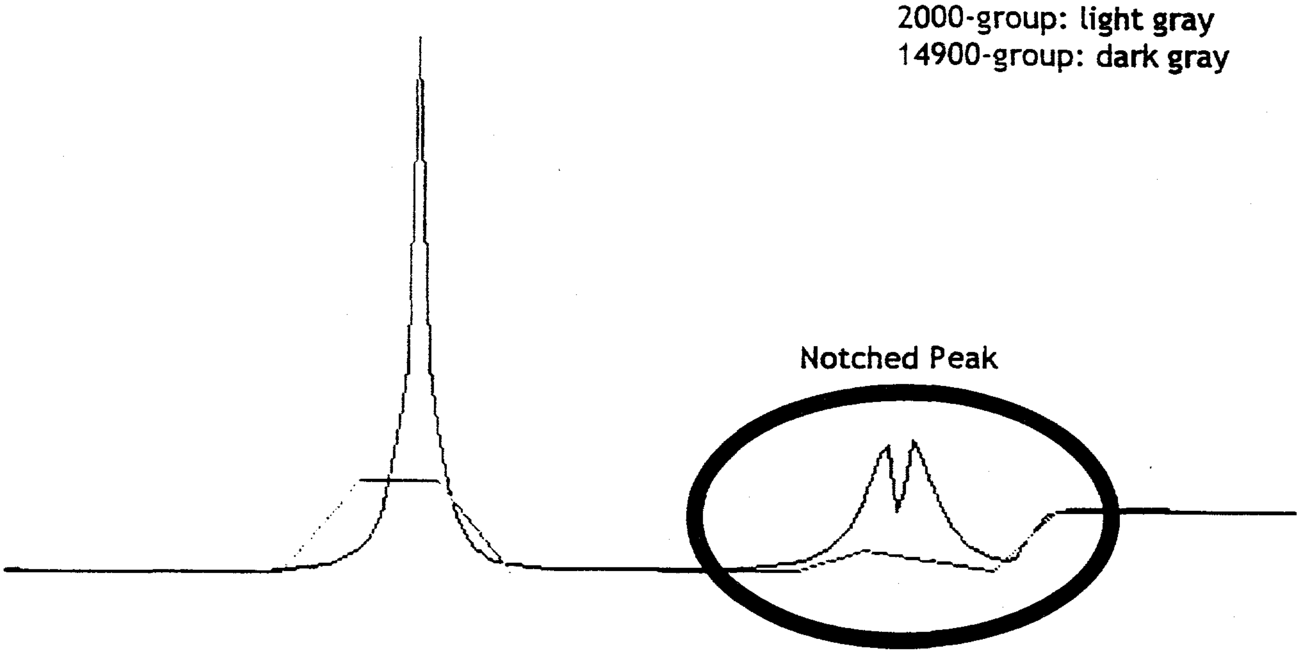

Carbon, 1000eV, 0.0787g/cc

As mentioned during the discussion of domain, the 2000-group graphs will sometimes miss out on major structure in elements of larger number such as titanium, shown in the following example.

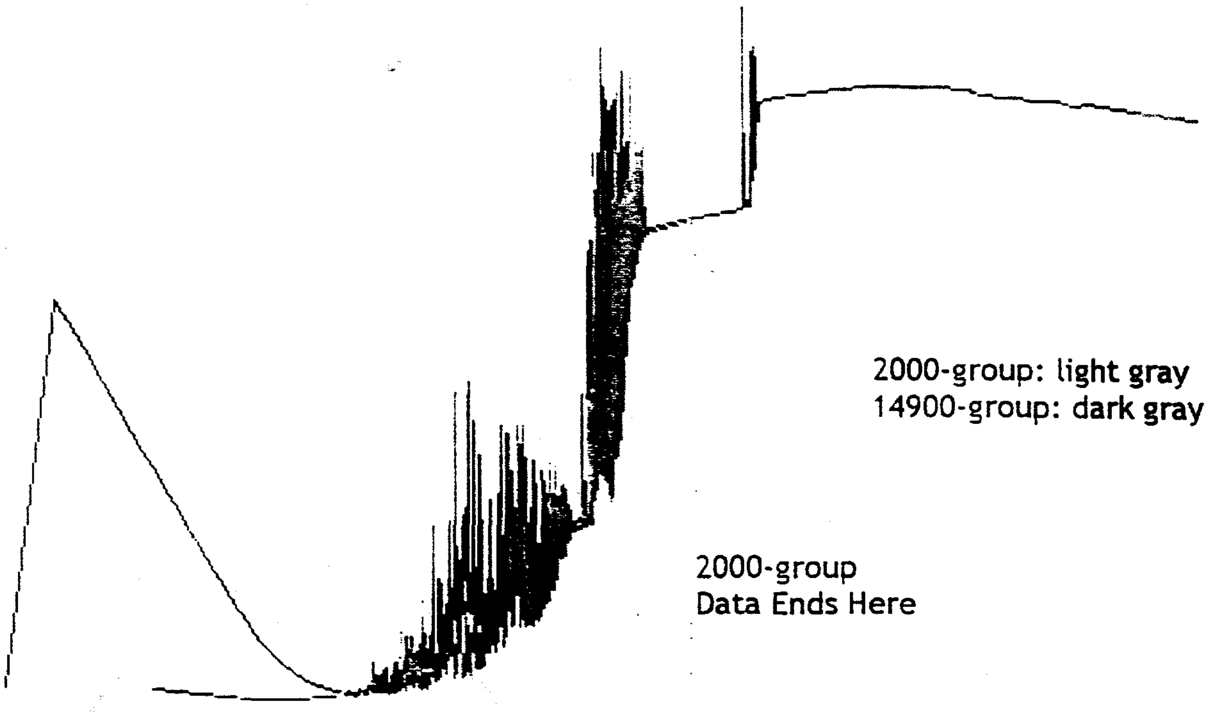

Titanium, unknown temperature and density

6. Conclusion

The Java opacity viewer can provide a valuable tool for identifying differences between 2000-group and 14900-group opacity data. These differences arise from the greater range and domain of the 14900-group, the lack of scattering in the 14900-group data, and the changes in theoretical model from the 2000-group to the 14900-group.

7. References

1. W.F. Huebner, A.L. Merts, N.H. Magee, Jr., and M.F. Argo, Los Alamos National Laboratory Report LA-6760-M, 1977.

Statistical Properties of Continuous and Discrete Distributed Phase Plates

Jyoti Kandlikar

Advisor: Dr. Reuben Epstein

LABORATORY FOR LASER ENERGETICS
High School Summer Research Program
6 July–27 August 1999

University of Rochester
250 East River Road
Rochester, NY 14623-1299

Abstract

Continuous distributed phase plates (DPP's) have replaced discrete DPP's because of their ability to more effectively focus the energy of the OMEGA laser onto the fuel pellet in the University of Rochester's Laboratory for Laser Energetics study of inertial confinement nuclear fusion. Fourier transforms and PV WAVE analysis programs have been employed to study the actions of continuous DPP's. Using the properties of continuous DPP's, this paper evaluates the extent to which continuous DPP's are characterized phenomenologically by existing formulas for discrete DPP's. These formulas for discrete DPP's are used in numerical 1-D simulations of fusion implosions. Through this analysis, it was determined that continuous and discrete DPP's have similar properties, such as similar correlation functions, and the formulas for discrete DPP's do provide a rough characterization of continuous DPP's.

I. INTRODUCTION

Humans currently depend on limited natural resources, such as fossil fuels, to produce energy that fuels the world. Because there is a limited supply of these resources and their burning creates pollution that is detrimental to the environment, there is a search for alternate forms of energy. Although nuclear fission has partially replaced fossil fuels as an energy source, fission requires fuels that are limited in quantity and outputs end products that are radioactive, which produces health concerns and requires complex storage methods.

The Laboratory for Laser Energetics at the University of Rochester houses the OMEGA laser, which is used to study inertial confinement fusion. The OMEGA laser is used to compress and heat deuterium and tritium, two isotopes of hydrogen, in order to fuse them together and produce neutrons, alpha particles, and energy. The fuel must be radiated uniformly on the target: if the radiation is nonuniform, Raleigh–Taylor instabilities will occur and cause the fuel to mix with the fuel container, resulting in significant decreases of output energy.

Much effort has been spent to uniformly irradiate the fuel, such as the OMEGA's 60-beam design to illuminate the fuel pellet from all sides. However, each laser beam contains intrinsic nonuniformity due to the imperfections in the optics as well as the turbulence in the air through which the beams pass. In order to make the beam more uniform before it focuses onto the target, devices called distributed phase plates, or DPP's, are used. DPP's are clear plates of glass approximately 30 cm in diameter through which the laser beams pass. As shown in Fig. 1, DPP's reduce the nonuniformity of a laser beam from large-scale nonuniformity to small-scale, finer speckle, which can later be further smoothed by the process known as smoothing by spectral dispersion (SSD).[1]

As illustrated in Fig. 2, there are two types of DPP's: discrete and continuous. The Laboratory of Laser Energetics' old 24-beam OMEGA laser used discrete DPP's, while its current 60-beam OMEGA laser uses continuous DPP's. Discrete DPP's are composed of approximately 15,000 interlocking hexagons which either give the incoming beam a phase shift of zero or pi radians, or a shift of zero or half a wavelength.[4] As the beam passes through a discrete DPP, the hexagonal elements divide the beam into a number of "beamlets," of which a randomly chosen half contain a pi phase shift. The power and uniformity resulting at the image plane can be determined by studying the interference of all the beamlets.[2]

Continuous DPP's produce a similar result, but they are structurally different. Unlike discrete DPP's, continuous DPP's are not composed of distinct elements. Rather, they have a smooth surface, designed in a process known as simulated annealing, that is rippled to produce a phase shift of up to 50 radians.

Continuous DPP's focus energy more efficiently than discrete DPP's. Discrete DPP's lose a large amount of energy in side lobes while focusing the beam on the target while continuous DPP's lose much less energy to side lobes. Discrete DPP's can only bring 78% of the incoming energy onto the target while continuous DPP's are able to bring 99% of the energy onto the target. However, the beams are aimed so that their radius at the target is slightly greater than the radius of the target, which ensures that all parts of the target will get illuminated. Due to the small loss of the energy that falls outside the target, in actuality 95% of the energy is focused onto the target when a continuous DPP is used.[3]

Unlike discrete DPP's, continuous DPP's are not made of distinct elements whose interference can be studied. However, discrete and continuous DPP's produce similar effects as they both are used to change the large-scale nonuniformity of the beam into finer speckle patterns of nonuniformity. Since their functions are similar, but only the properties of discrete DPP's have been analyzed mathematically, continuous DPP's were evaluated with the existing statistical models that described discrete DPP's to determine their correspondence with these models and the accuracy to which these models describe the nonuniformity of the continuous DPP.

II. METHODS AND PROCEDURE

The intensity pattern of a beam passing through a discrete DPP is expressed in Epstein[4] as the product of a smooth envelope and a function that modulates it. This modulation function takes the form of the Fourier series with coefficients given by the correlation function C(Δx),[2]

$$C(\Delta\mathbf{x}) = \iint_A e^{-i\phi(\mathbf{x})} e^{i\phi(\Delta\mathbf{x}+\mathbf{x})} d^2x, \qquad (1)$$

where $\Delta\mathbf{x}$ is the separation length of two points on the DPP, A is the area of the DPP, and $\phi(\mathbf{x})$ is the phase delay at $\mathbf{x}$.

Creating the correlation function for the continuous DPP requires the use of fast Fourier transforms, or FFT, in the Visual Numerics data analysis software, PV Wave. FFT was used because of the relationship between Fourier transforms and the correlation function,

$$C(\Delta x) = \overline{\overline{e^{-i\phi(\mathbf{x})}} * \overline{e^{i\phi(\mathbf{x})}}} \qquad (2)$$

where $\overline{f(\mathbf{x})}$ indicates the Fourier transform of $f(\mathbf{x})$.[5] The function was performed on the array which depicted the phase delay caused by the continuous DPP. The square array contained the values of the circular DPP's phase delay, while the regions outside the circle A were eliminated by using a weighting function set to zero, as there was no illumination outside the DPP.

It was necessary, due to the PV Wave's limitations in raising numbers to complex powers, to use Euler's Theorem to convert the imaginary exponential to sine and cosine notation.

$$f(x) = e^{-i\phi(x)} = \cos\phi(x) + i\sin\phi(x) \qquad (3)$$

The FFT function assumes that the array repeated itself an infinite number of times in all directions, but a zero weighting function was used and the values of the array were zero outside the area of the DPP. To prevent this repetition from distorting values, the original array was padded with zero weighting extending for a distance equal to the length of the original array. For correlation separation lengths less than or equal to two diameters of the DPP, the repetitions were too far away to affect the data, and the function used only the original data.

For most separation lengths, there were many values where one or both ends of the separation length were in the zero padded region outside the circular DPP. As shown by Eq. (3), the value of the function being correlated was equal to one when the phase of x, or $\alpha(x)$, was zero. All the separation lengths located outside the circle contributed a large number of ones to the data. To prevent these false values from adding to the correlation, it was necessary to implement a masking function or weighting function which ignored values of the separation length in which one or both of its ends were not a part of the continuous DPP.

Transforming the $e^{-i\alpha(x)}$ into the frequency domain and multiplying it by its complex conjugate revealed the intensity projected onto the far field, or target plane. Figure 3 shows the relative intensity patterns for the cross section of the phase plates in the x and y directions. The intensity pattern can be seen as a uniform envelope modulated by a random function which accounts for the spikes and speckle produced.

The correlation function was obtained by then taking the Fourier transform of the intensity. The correlation function can be more easily visualized and understood by plotting the square root of the absolute value of the correlation function.

The correlation function created from the entire set of data, as shown in Fig. 4, is marked by two small maxima evident at large separation lengths that are slightly less than the diameter of the DPP. This is not predicted, as the envelope function should trail off slowly and steadily to zero. However, the correlation function taken of the data when the outside values, or values with a large distance to the center of the DPP, were removed produced a correlation function without the end maxima and with values that smoothly and regularly went to zero. As seen by their disappearance when the outside data was masked, the maxima were most probably an edge effect of the FFT function created in the correlation function of large separation values.

In Fraunhofer optics, when light of a uniform intensity passes through two rectangles, the frequency of the diffraction pattern is greater when the rectangles are farther apart. Discrete DPP's can be evaluated as the sum of the interference pattern of all pairs of individual elements, where the pairs of individual elements act like two rectangular openings. The weight of importance of each specific separation length can be considered by taking the overlap of two circles, one whose center has been displaced by a separation length Δx. The overlapping region corresponds to the number of element pairs in the circle with a separation length Δx, which also corresponds to the relative importance of the frequency created by the diffraction of two rectangles with a separation of Δx.[1] The average correlation function squared for a discrete phase plate is given in Eq. [26(a)] in Epstein[1] as

$$\left\langle |C(\Delta\mathbf{x})|^2 \right\rangle = \frac{2}{\pi N}\left[\cos^{-1}\left(\frac{\Delta x}{2R}\right)-\left(\frac{\Delta x}{2R}\right)\sqrt{1-\left(\frac{\Delta x}{2R}\right)^2}\,\right] \tag{4}$$

where **Δx** is the vector of the separation, Δx equals |**Δx**|, N is the number of elements in the discrete DPP, and R is the radius of the DPP. The relative values of the average correlation function for a discrete DPP are shown in Fig. 5.

III. RESULTS AND DISCUSSION

Figure 6 shows the result of plotting the square root of the average correlation function for a discrete DPP and fitting it onto the plot of the average correlation of the continuous DPP. It can be seen that the two functions look similar, and that the average correlation for a continuous phase plate appears to be similar to the average correlation function for a discrete DPP.

While the average correlation function deals with the speckle from the correlation function, a large spike was also part of the correlation function (Fig. 7). This large spike, which is centered over a separation length equal to zero, is caused when the data is shifted by a length close to zero. At these small shifts, each point in the function is being correlated with itself and is constructively adding up to produce the peak. As the separation length increases, each point of the function is shifted by that larger length, and it no longer interacts with itself. Instead, it interferes randomly with the random phase of the element it is paired with.

According to Epstein,[4] the correlation function is created by the transform of two functions, the envelope function, $F(p)$, and the modulation function, $G(p)$. In one dimension, these are

$$F(p) = \frac{\sin^2 p}{p^2} \tag{5}$$

and

$$G(p) = 1 + \sum_n \left[g_n \cos 2np + h_n \sin 2np \right] \tag{6}$$

where p is the variable dependent on the angle from the DPP to the target plane, n is the index indentifying all points on the DPP, N is the number of elements in the DPP, $g_n = \frac{2}{N} \sum_{j=1}^{N-n} \cos \phi(j) \cos \phi(j+n)$, and $h_n = \frac{2}{N} \sum_{j=1}^{N-n} \sin \phi(j) \sin \phi(j+n)$. The transform of

F(p) is a triangle function, centered at zero with a base of 4 and a height of pi. The transform of *G(p)* is three delta functions.[6]

$$\frac{\overline{G(k)}}{2\pi} = \delta(k) + \sum_n \frac{g_n}{2}[\delta(k-2n) + \delta(k+2n)] + \sum_n \frac{h_n}{2i}[\delta(k-2n) - \delta(k+2n)] \qquad (7)$$

The convolution of the two functions, which is equal to the transform of the product of each function's Fourier transform[5]

$$\overline{F(p)G(p)} = \frac{1}{2\pi}\int \overline{F}(k-k')\overline{G}(k')dk' \qquad (8)$$

causes each of the delta functions to become triangles. The first triangle, caused by the $\delta(k)$ function has a base centered at zero and a height of pi, is the coherent spike. The other delta functions are turned into triangles centered at 2n with a height of $(\pi/2)(g_n + h_n/i)$. These triangles create the speckle, and, using random statistics of Epstein,[4] are shown to have an average height of $\pi/N_1{}^{1/2}$, where N_1 is the effective number of beamlets emerging from the continuous DPP. Since the height of the spike is π, the ratio of the spike to the speckle is

$$\frac{\text{Height of Spike}}{\text{Height of Speckle}} = \frac{\pi}{\frac{\pi}{\sqrt{N_1}}} = \sqrt{N_1} \qquad (9)$$

Therefore, the ratio of the coherent spike to the value of the speckle is $1:\frac{1}{\sqrt{N_1}}$. Using the numbers obtained by the continuous phase plate, the value of this N_1 was approximately 140,000.

Another value for the effective number of elements N_2 in the continuous DPP is acquired by studying the width of the center spike at half its height. At the separation distance of either end of this width, the element has an equal probability of interacting with itself as it does of interacting with a distinct, random, neighboring element. The value at the half peak is approximately equal to four radii of the distinct elements, but it needs to be corrected slightly to account for the elements being circular and therefore overlapping in a slightly different shaped spike.[6] The effective number of elements in the continuous DPP is obtained by dividing the total area of the DPP by the approximate area of each element, obtained from the effective radius of each element. In the continuous phase plate, using these calculations, the effective number of elements, or N_2, was 55,000.

In a discrete DPP, each distinct element creates its own beamlet, and the number of elements equals the number of beamlets created, or $N_1 = N_2$. However, the values obtained for a continuous DPP, while within a factor of three, were not equal.

IV. CONCLUSION

The continuous DPP was analyzed using Fourier transforms and PV Wave programming. Based on the resulting correlation functions, the following conclusions were drawn.

- Discrete and continuous DPP's have similar properties, such as similar average correlation functions.
- Continuous DPP's are not made up of distinct elements, and estimates of how many effective beamlets they create or elements they are made from are only phenomenological attempts to characterize their behavior.
- The continuous phase plate creates approximately 140,000 effective "beamlets" and is composed of approximately 55,000 effective elements. These numbers vary from the 15,000 elements and "beamlets" of a discrete DPP, but the fact that the numbers exist within the same order of magnitude suggests that it is possible to study continuous DPP's with adjusted models for discrete DPP's.
- Discrete and continuous DPP's have similar, but not identical, statistical properties. The formulas created for discrete DPP's are a roughly approximate description of continuous DPP's and are usable in their current applications, such as simulations for fusion implosions.

Additional work in understanding continuous DPP's is recommended. Study using a more quantitative, rather than qualitative, approach would further reveal the similarities between continuous and discrete phase plates. Procedures such as azimuthally averaging the correlation function, rather than using the cross section, would create more numerical, rather than relative, values. Fitting the average correlation function of discrete DPP's to that of the continuous DPP could be more accurately done by using a least-squares fit.

The results from the present work will go to further the understanding of continuous DPP's. Creating formulae that accurately describe their functions will assist in the accuracy of the hydrocode simulations of fusion implosion and ultimately result in the ability to make the laser beams more uniform, which will create more effective fusion reactions and assist in the goal of nuclear fusion one day becoming an effective power source.

V. ACKNOWLEDGMENT

I would like to express my deep sense of gratitude to Dr. Reuben Epstein for his constant encouragement and support as well as for the countless hours he spent guiding and advising me. I would like to thank Dr. Stephen Craxton for organizing the program for high school students and providing me the opportunity to participate in it. I would also like to thank the other members of the high school summer program for their companionship and the excitement of working with them.

REFERENCES

1. R. Epstein. "Properties of Speckle of Focused. Phase-Converted Laser Beams and the Reduction of Time-Averaged Irradiation Nonuniformity in Laser Driven Plasmas due to Target Ablation." J. Appl. Phys. **82**, 2123–2139 (1997).
2. R. Epstein and S. Skupsky, "Anticipated Improvements in Laser Uniformity Using Distributed Phase Plates with Quasirandom Patterns," J. Appl. Phys. **68**, 924–931 (1990).
3. "High Efficiency Distributed Phase Plate Generation and Characterization," Laboratory for Laser Energetics LLE Review **65**, NTIS Document No. DOE/SF/19460-117 (1995). Copies may be obtained from the National Technical Information Service, Springfield, VA 2211.
4. "Phase Conversion of Lasers with Low-Loss Distributed Phase Plates," Laboratory for Laser Energetics LLE Review **55**, NTIS Document No. DOE/DP/40200-257 (1993). Copies may be obtained from the National Technical Information Service. Springfield. VA 2211.
5. Ronald N. Bracewell. *The Fourier Transform and Its Applications.* (McGraw-Hill, New York. 1986), p. 112.
6. R. Epstein. LLE. private communication (1999).

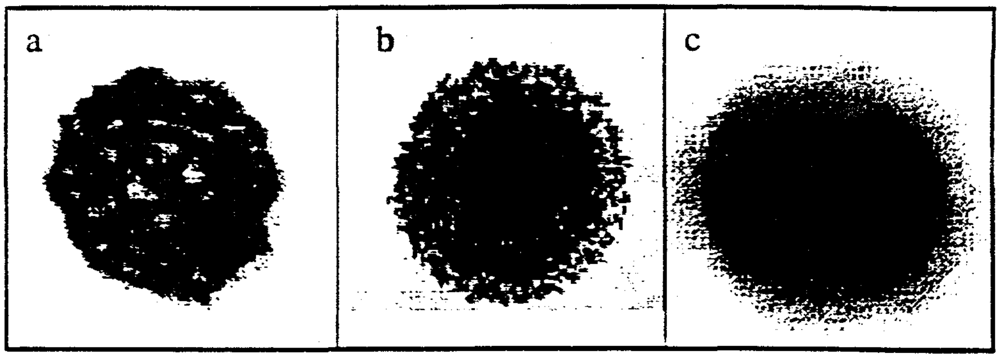

FIG. 1. The non-uniformity of a laser beam (a) from large non-uniformity to small, finer speckle (b), which can later be further smoothed by the process known as smoothing by spectral dispersion (c).

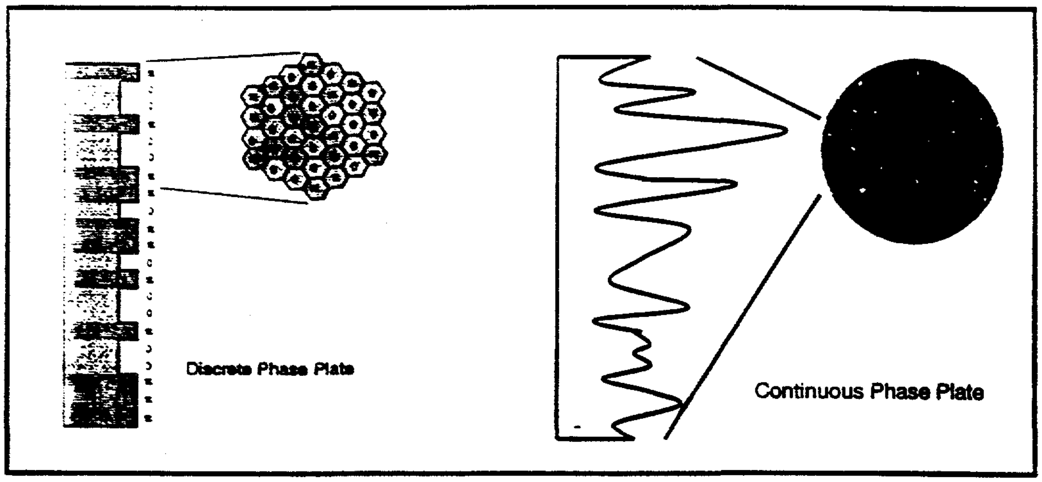

FIG.2. Illustration of a discrete and continuous DPP. Discrete DPPs consist of interlocking hexagons of a pi or zero phase delay, while continuous phase plates smoothly vary in thickness to produce phase delays from 0 to 50 radians

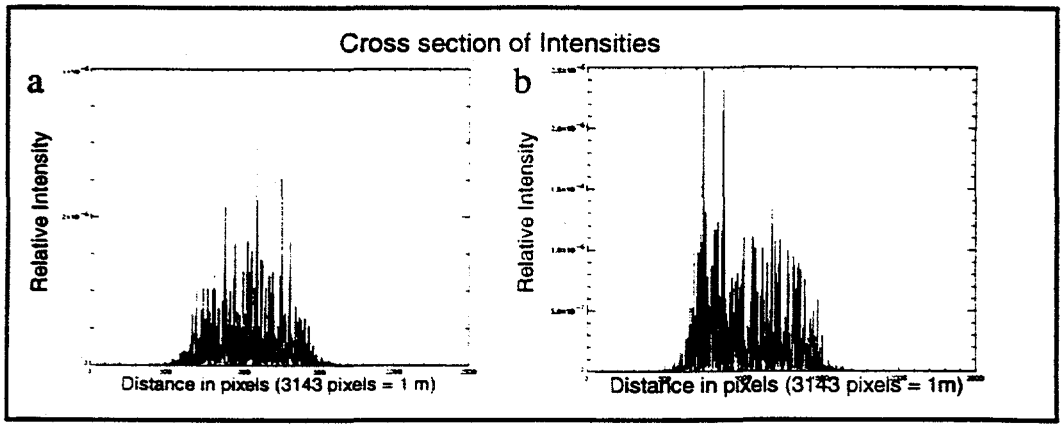

FIG. 3. The relative intensity pattern for the cross section of the continuous DPP in the (a) x and (b) y directions

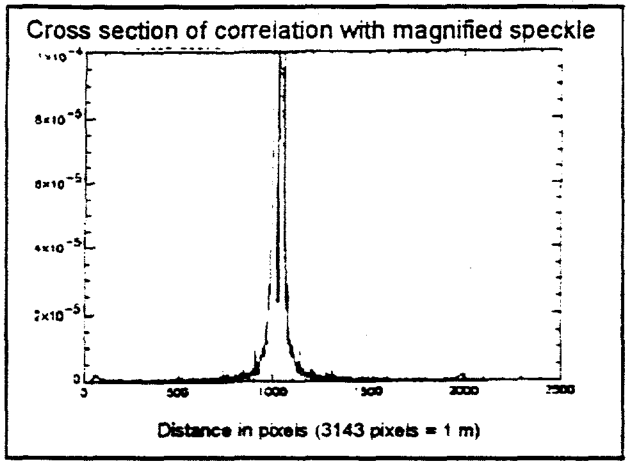

FIG. 4. (a)The correlation function created by using the entire set of data is marked by two small maxima evident at large separation lengths that are slightly less than the diameter of the DPP.

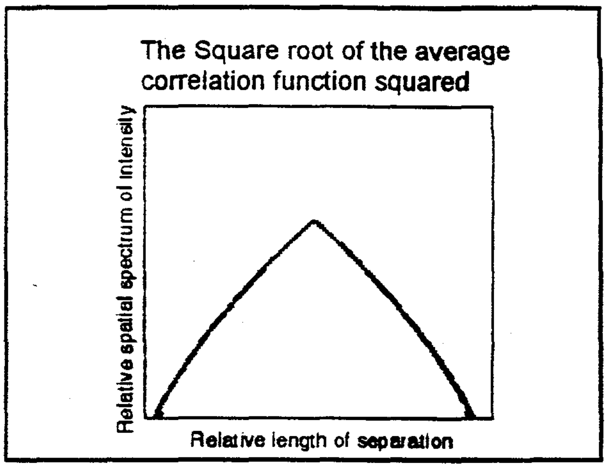

FIG.5. The relative values of the average correlation function for a discrete DPP

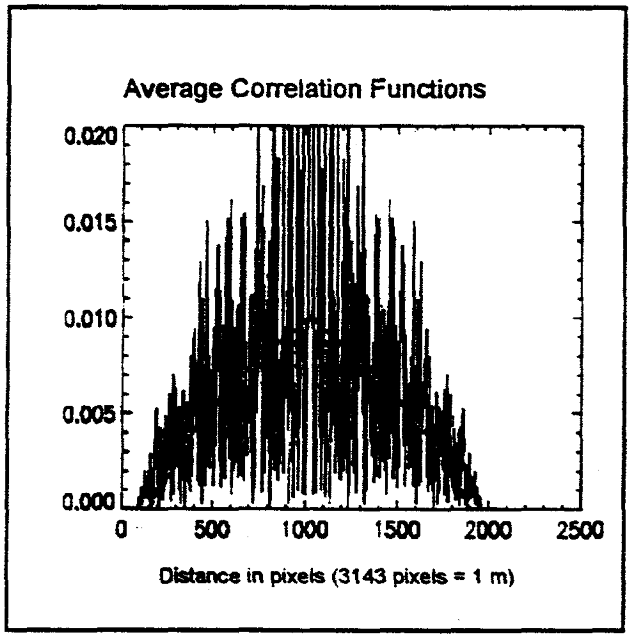

FIG. 6. Plot of the average correlation function for a discrete DPP fit onto the plot of the average correlation function of the continuous DPP

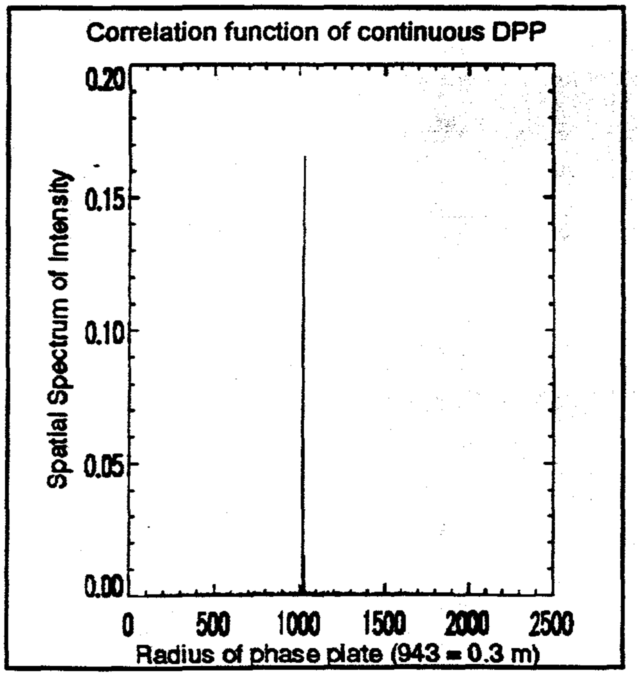

FIG. 7. The correlation function of the continuous DPP, which is characterized by a coherent spike centered around the separation length of zero and speckle caused by the random interference of random elements at greater separation lengths

Bandwidth Measurement of Fiber Optic Bundles

Brian Kubera

Advisor: Robert Boni

Laboratory for Laser Energetics

University of Rochester

Summer High School Research Program

1999

Introduction:

Improvements can only be made to the extent to which they can be observed. This statement, while drastic and, in many cases, wrong, becomes very true when dealing with phenomenon that are not completely understood or in situations where there exist variables that cannot be accounted for. Lasers are capable of producing very narrow pulses of light and also, at times, can behave in ways that are not completely understood. For laser science to progress, it is also necessary for the diagnostic tools used to keep pace with, or ahead of, the field. The Laboratory for Laser Energetics (LLE) is continuously working to improve laser diagnostics to allow for improvements to be made on its laser system, OMEGA.

The OMEGA laser is used primarily for the study of inertial confinement fusion (ICF). ICF is a technique of compressing fuel by exploding a substance surrounding it. The rapid compression of the fuel, caused by the expansion of the shell, forces atoms within it close enough together to result in fusion. Plastic is commonly used to make up the outer shell. The fuel consists of deuterium and tritium atoms, both isotopes of hydrogen. The initialization energy for this event is provided by OMEGA through a method titled Direct Drive ICF. OMEGA's sixty beams are focused directly onto the fuel pellet and provide the energy to explode the shell and heat the fuel.

While a significant amount of power is required to overcome the forces of repulsion between the deuterium and tritium atoms. it is also essential that the power be evenly distributed. A target that is non-uniformly irradiated will not compress efficiently. Much like squeezing a ball of play-doh in one's fist, a poorly irradiated target will compress least where the intensity of irradiation is least and will tend to "squeeze through" at those points. This results in less force transferred to the fuel within the center of the pellet and in turn reduces the probability of the occurrence of fusion.

Recent effort has been put into achieving greater on-target uniformity. One break-through that has significantly improved beam uniformity is smoothing by spectral dispersion (SSD). SSD actually does little to correct instantaneous errors, but by rapidly wiggling the beam, uniformity is achieved over a period of time. However, the beam movement utilized by SSD introduces a potential problem. Optical devices called pinholes are used to clean-up the laser wave front periodically through out OMEGA. If the beam is slightly misaligned, the movement SSD induces can cause the beams to be obstructed temporarily by the pinholes. This result in amplitude modulation of the beams at between 3.3Ghz and 10.4GHz, SSD's operating frequencies.

To ensure power balance between the sixty beam lines it is essential that the output be constantly monitored for errors caused by SSD or other problems that would result in distortion of OMEGA's pulse shaping. An instrument called a streak camera is used for this purpose.

Streak cameras are used to measure optical signal intensity over time. They have a very high bandwidth, 100GHz is typical, but can only operate at a low rate of repetition. This makes them ideal for measuring the single, short output event of OMEGA.

To produce accurate streaks, an image taken by a streak camera, the cameras must be located away from OMEGA's target chamber to eliminate neutron-induced noise. This creates the need for a medium to transport the beam sample from OMEGA to the streak cameras. A fiber optic bundle is used for this. The bundle was chosen over a single fiber because a single fiber could only sample a small cross section of the beam. A large sampling area is justified by the law of large numbers; more speckle, points of different intensities which make up the beam, can be sampled on a larger input surface. The movement of speckle in a small sampling will produce more amplitude modulation that is not representative of the beam than the same speckle movement in a larger sample.

The quality with which the fiber bundles can be produced limits their bandwidth. Small variations in the length of each individual fiber within the bundles cause the signal to leave the fibers at slightly different times. It is desired to keep the bandwidth limit induced by length variation greater then 30GHz. 30GHz would allow for the observation of any amplitude modulation caused by SSD. To ensure this goal is met the bandwidth of every fiber bundle produced must be measured. To expedite testing a computer program was written to perform many of the required tasks.

Bandwidth Measurement:

Bandwidth can be found by comparing the full width at half max of the output pulse to the full width at half max of the original pulse. The square of the original pulse width is subtracted from the square of the pulse being measured to give the square of the difference between the two pulses. The difference in picoseconds divided into 330 gives an approximate bandwidth in gigahertz.

The setup used to test the fiber bundles consisted of a short pulse laser, pre-amp, frequency doubling crystal, launcher box, and a P510 streak camera. (Figure 1) A 90 ps Gaussian pulse in the infrared was sent into a pre-amp from the REGEN and amplified so that the light could easily be attenuated to an intensity that could be measured by the streak tube. The beam from the pre-amp was frequency doubled with a second harmonic generating (SHG) crystal to produce a beam containing both the infrared and green wavelengths, 1053 and 527nm respectively. The measurement was originally intended to be made using the UV wavelength, 351nm, the wavelength that the fibers would be used for, however an optics module for the streak camera that would transmit UV was unavailable at the time that testing began.

To test the bandwidth due to error in the fiber length it was necessary to account for any distortion introduced by the fiber optic material. A single fiber, from the same preform and of the same length as the fiber used in the test bundles, was used in parallel with the test bundle to act as a control. The output from of this fiber would be distorted in the same ways that the output from a perfect fiber bundle would be.

Measurement Software:

A computer program was written to integrate all processes required for the collection and analysis of the bandwidth measurement data. Initially, all of the programming was done with Microsoft Visual Basic so that a graphical interface could be easily created. However, it was found that a number of computations ran slowly while coded in basic so the more problematic ones were later rewritten in C++. The program can be described as being composed of five blocks; streak camera control, data acquisition, data analysis, data storage and retrieval, and data display.

The streak camera contains two separate units that require communication with the computer, the stre camera control module and the CCD camera. The streak camera control module controls the voltages on t streak tube, the enabling of the triggers and all of the features supported by the present optics module. It communicates with the computer via an RS-232 serial connection. The CCD camera is controlled through one of the computer's PCI ports. Besides sharing a common trigger and supplying the shutter's trigger, the CCD camera is isolated from the rest of the streak camera.

For reasons of practicality, exploitation of the numerous commands supported by the streak camera control module was limited. To preserve simplicity and to avoid problems resulting from the use of contro modules with different command sets, an individual command set for the control module was not included in the program. Instead, a terminal window was included. Commands can be entered in the command line and an above window displays a record of all commands sent to the control module and any responses for the control module.

Control of the CCD camera is performed solely by the software. Default settings for the CCD camera are programmed into the software. There are a handful of settings that can be specified by the user, such as gain, shutter mode and trigger mode.

The data acquisition process is composed of a series of communications between the computer, the CCD camera and the streak camera control module. When acquiring test data, the streak images must be accompanied by a background image that must later be subtracted from the foreground to compensate for the dark current in the streak tube. The background image must be acquired under the same conditions that the streak occurs but with the shutter closed. This means that if the streak has to wait for an external trigger then so must the background and also the mode of operation must also remain constant.

To begin the acquisition process the streak camera control module is sent a command to begin operating in its operating mode. In this mode all high voltage supplies are activated and the sweep trigger i enabled. The CCD camera is then put into the correct operating modes by the computer. This includes size of image to acquire, gain, shutter mode, trigger mode and exposure time. The particular shutter mode that i read out to the camera is dependent on whether the camera is taking a background image or a foreground image. The camera is then given a command to capture an image. When in the trigger mode used for testing fibers, the capture command only enables the camera to accept a trigger. The camera will take a frame when a pulse arrives. The computer will then download the image from the CCD and process it. If multiple images are taken. as commonly are, the CCD is enabled to take another frame once the computer has received an image.

Storage of the data is important so that an accurate record of each cable's bandwidth properties can be kept; data records are also helpful to identify problems in the test setup. By default every image received from the CCD camera is saved, backgrounds and foregrounds are saved as separate images. The file names of every image saved includes the year, month, day, hour, minute, second of when it was taken and also a root name common to all of the images taken within a single loop. The root name is specified by the user and may be repeated. To catalog groups of images an index file is made for every group, the index file contains the file names of all of the images in that group and provides the file names of the background files for every foreground file. With the index file, an entire group of streaks can be recalled into the program quickly for review. A single streak can also be recalled by specifying the foreground and background files.

When using the program to perform bandwidth tests it became common practice to take about one hundred streaks for a particular cable at a time. The images were then saved as a group in its own folder with an index file. A second index file was then created containing only selected streaks (see below). This was stored along with its complete set.

The data is analyzed using the method described earlier. When the foreground image is received the most recent background image is subtracted from it. The data is then split into three channels to represent the three inputs of the streak camera. The user is able to specify the boundaries of these channels by positioning them graphically over a bitmap image of the previous streak. The subtracted image is the reduced to three line outs by averaging the data vertically within each channel to produce a single value for each column within each channel. The maximum value in each channel is then determined. Each line out is then followed down from the maximum value until a value that is less then 35% of the max value of the channel is reached and that point was noted, this is done on all channels and down both sides of the max. A Gaussian pulse is then fitted to the values above the 35% mark in each channel. A chi-squared value is calculated for each fit. The Gaussian fits are used to find a more meaningful max value for each channel and those values are in turn used to determine the half-max level. Using the half-max value for each channel and the channel lineouts, the full-width at half-max (FWHM) is determined between two parabolic fits. In each channel on both sides of the curve, six data points are taken from directly below the half-max line and six from directly above the half-max line, and a parabolic curve is fitted to each of the two clusters of twelve points. The points are found on the curves that intersect the half-max and the distance between the two curves is determined to be the FWHM in terms of CCD pixels. The width can be found in this manor at any level and also at multiple levels at once. This was included so that the pulse widths around th 10% level could be observed to identify any possible fibers with a length significantly different from the mean length. The FWHM values are then converted to picoseconds by multiplying them by a user supplied constant that specifies the number of picoseconds that each pixel represents. The difference in quadrature i then found between the reference and the test piece and then that value is divided by 330 to give the bandwidth approximation.

It is common for unusable streaks to be taken. This occurs because jitter within the electronics causes variation in the moment that a streak is taken relative to the moment that the pulse arrives. Unusable streak also occur when the high power supply fails. Because of this, the user is given the option of selecting desirable streaks, which can then be saved with a separate index or viewed exclusively. The selections can be made while streaks are being taken and the program can also select streaks automatically by determining if a Gaussian can be fit to any of the channels.

Once a streak has been analyzed it is displayed graphically. Both a channel lineout plot and a bitmap o the image received from the CCD camera are given. The bitmap image is actually the log of the CCD camera image. This step was taken so that low order features could be identified from the image. The channel lineout plots were capable of displaying the Gaussian fits, each of the parabolic fits and the half-max level in addition to the channel lineout. By dragging the cursor over either the channel lineout or the CCD image, values could be obtained for that particular position within that set of data. All final calculated values are displayed to right of the corresponding channel lineout.

A method a of navigating through a data group is provided. Up and down buttons are used to move through the streaks one at a time. Moving through the data can be done selectively if desired. A "goto" function can also be used to recall a specific streak.

Fiber Test Results and Future Development:

The initial fiber bandwidth tests were unable to produce consistent bandwidth values for the fiber bundles on hand. In many cases the pulse produced by the fiber bundles was interpreted to be narrower then the control fiber's output. All fiber bundles tested produced outputs very near to the control output. They have been tentatively said to have a bandwidth due to length variation between 20 and 50 GHz.

There were several problems that were evident during the testing. The optics module available limited the testing to the use of 527nm light. The use of 351nm light would be required to obtain the true bandwidth limit that would be experienced while measuring OMEGA. The UV light does not propagate through the fibers as quickly as the green light used so the bandwidths would be expected to be slightly lower.

Another problem was encountered with the sweep speed. By plotting the center of each pulse against the distance between two pulses (Figure 4) it was found that the streak speed was not linear. This could have been the caused by the pulse arriving at a moment when the plates were either just beginning a sweep or just completing a sweep; instances where the rate of voltage change between the deflection plates is far from linear. This problem can be corrected by adjusting the internal delay of the camera so that the deflection plates are sweeping linearly when the laser pulse arrives.

A shorter pulse laser is essential if bandwidths are to be accurately determined. The 90ps laser used for all tests, so far, has not produced consistent results. This can be attributed to the small variations in the FWHM that must be observed to calculate the proper bandwidth. The differences in pulse width between the control and the test piece are on the order of one or two CCD pixels, barely noticeable. If a short pulse were to be used, 10 ps would be desirable, the distortion introduced by the bandwidth would be more evident.

Acknowledgments:

I would like to extend my gratitude first and foremost to my advisor Robert Boni. I am grateful for his unselfish commitment of time towards the development of my project and also for the vast amount of knowledge that he chose to share with me. He was happy to show me around the labs and explain how things work. His teaching went far beyond what was required just to satisfy my curiosity. I would also like to thank Dr. Paul Jaanimagi for his input regarding the behavior of the streak tube and advice pertaining to the analysis of the streaks, Dr. Andrey Okishev for his assistance with the laser used during testing, Matthew Millecchia for providing the fibers used for testing and for showing me how assemble fiber optics, Matthew Pandina for providing programming assistance, and lastly, Dr. Stephen Craxton for his efforts to organize the summer program.

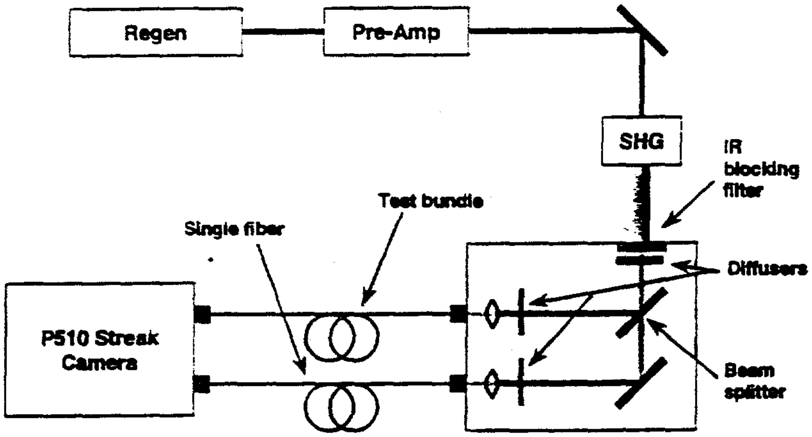

Figure 1: A 90 ps pulse is injected into the REGEN and then amplified and frequency doubled. The 527 nm light is launched into both the test fiber and a control fiber. A P-510 streak camera is used to measure both pulses.

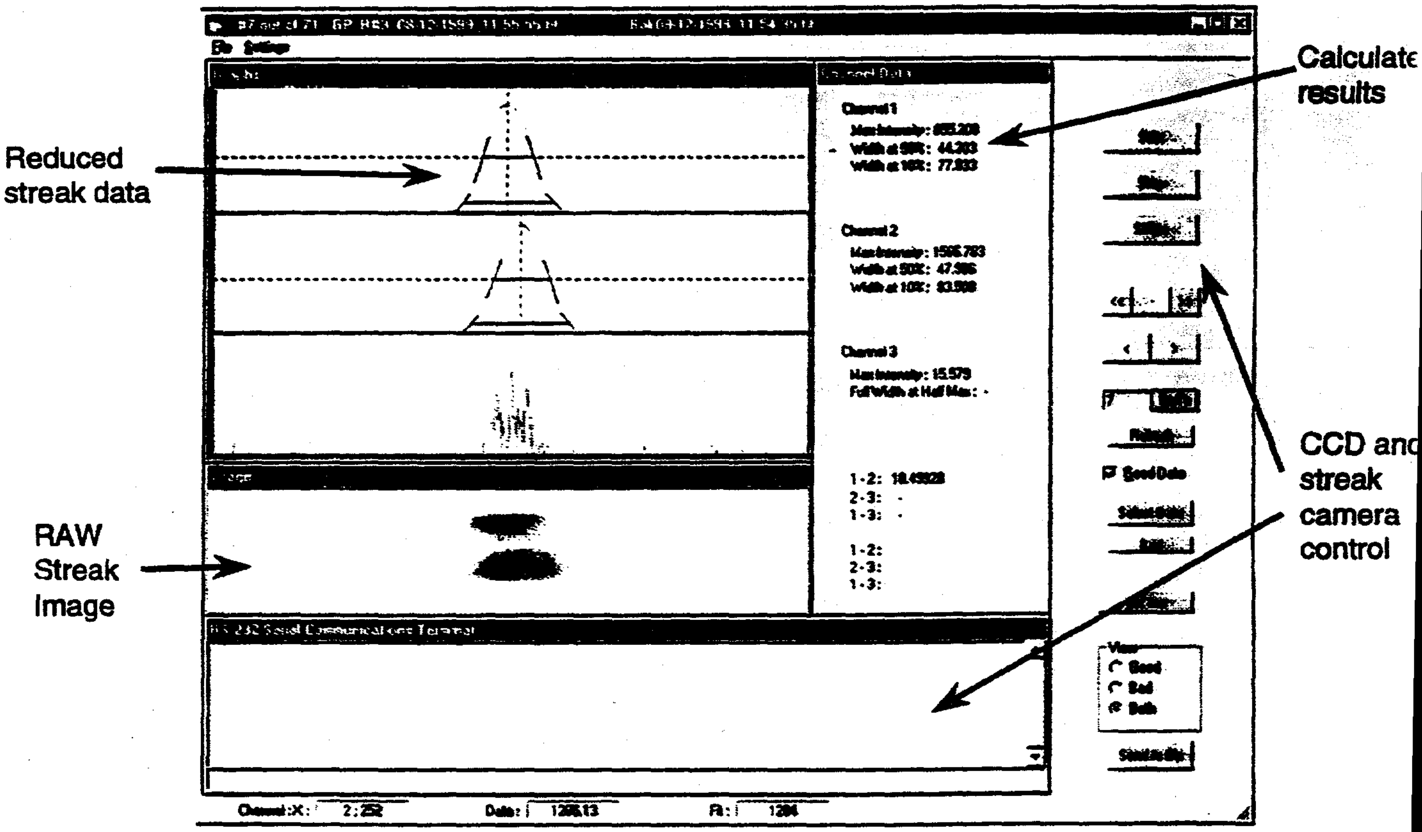

Channel 1
Max Intensity: 855.208
Width at 50%: 44.283
Width at 10%: 77.833

Channel 2
Max Intensity: 1506.783
Width at 50%: 47.586
Width at 10%: 83.508

Channel 3
Max Intensity: 15.579
Full Width at Half Max: -

1-2: 18.45928
2-3: -
1-3: -

1-2:
2-3:
1-3:

Channel:X: 2:252 Data: 1206.13 R: 1284

Figure 2: The graphical user interface displays data in a comprehensible manor.

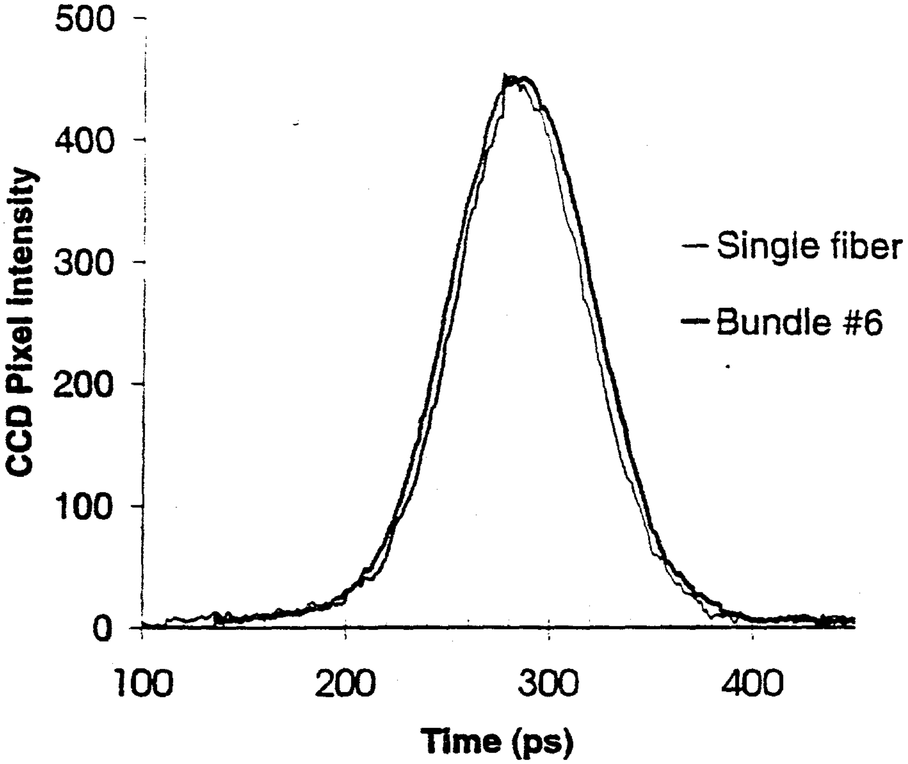

Figure 3: Example lineouts from a control fiber and a test bundle superimposed on top of each other.

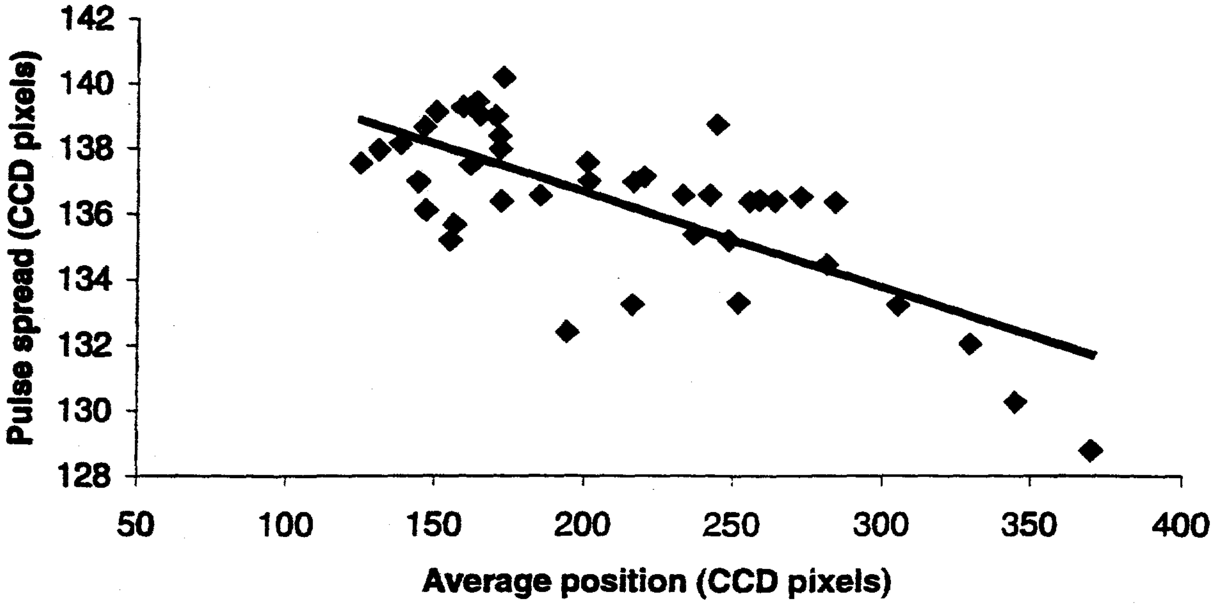

Figure 4: The average time of the arrival of two pulses relative to the sweep is plotted on the x axis in terms of CCD pixels (roughly 1.1 ps per pixel) and the time between them is plotted on the y axis in terms CCD pixels. This indicates that the sweep speed is decreasing as time progresses.

Analysis of the 3 ω SSD Spectrum of an OMEGA Laser Beamline

Aman Narang

The Harley School
Rochester, NY

Advisor: W. Donaldson
Scientist

1999 Summer High School Academic Research Program

Laboratory for Laser Energetics
University of Rochester

3 ω SSD Spectrum of an Omega Beamline

Summary

I performed research in laser fusion by developing a computer program to simulate the experimental ultraviolet laser spectrum near the end of the OMEGA laser system. By using Fourier Transform routines, I have found it possible to accurately simulate the spectrum. This is the first time a theoretical model of the laser spectrum has been made, and it will serve a number of important purposes for OMEGA.

Abstract

A computer model of the ultraviolet laser spectrum of an OMEGA beamline has been constructed that can accurately predict experimental results. Fourier Transform routines (FFT) are used by the model. It is shown that the measured response of the spectrometer that is used to measure the experimental spectrum must be convolved with the Fourier components of the electric field that describe the laser beam. Our results provide confidence in the use of this model to analyze the spectra of all sixty beams that comprise OMEGA. The model will confirm that all the bandwidth is successfully passing through the system. and that none of the frequencies on the pulse are cut off by the pinholes that the laser beam passes through. It will also help monitor the alignment of the potassium dihydrogen phosphate (KDP) frequency conversion crystals, and aid in analyzing the effects associated with the phases of the modulators.

Introduction

At the OMEGA laser system, inertial confinement fusion (ICF) is used to develop a method for harnessing the power of fusion. ICF is performed by heating the shell of a spherical pellet, the core of which is composed of deuterium and tritium (1). The energy transferred to the shell ionizes the atoms in it, and creates a dense layer of plasma surrounding the fuel core. The heated plasma expands, until it is torn free from the pellet at a speed of about 1000 kilometers/second. The materials inside the plasma layer (in accordance with Newton's third law of equal and opposite forces) are accelerated inwards. The resulting high temperature and density cause fusion inside the core which may ultimately be a source of energy if the work done on the system is less that the energy released at ignition (1).

It is critical that the target be illuminated uniformly so that different parts of the target are accelerated inwards at the same speed. By compressing the target uniformly, we can achieve the highest density. For this reason, the OMEGA laser system has 60 beams, all of which are superposed at the same time on the target, so that the the overlap between the beams averages out the imperfections in the different beams.

The OMEGA laser system starts in the infrared ($\lambda \approx 1$ micron) as a single nanosecond pulse. It is then amplified and split, and converted to the ultraviolet using a series of potassium di-hydrogen phosphate (KDP) frequency conversion crystals (Fig. 1). This is done because the fuel pellet absorbs the laser energy more efficiently at shorter wavelengths. Two frequency conversion crystals are used to convert the laser beam from the IR to the UV. The first crystal, a doubler, is used to double the frequency of approximately two-thirds of the energy in the laser beam, thereby reducing its wavelength by a factor of two. The second crystal, a tripler, combines the remaining one-third of the energy in the beam with the other two-thirds whose frequency has been doubled, thereby tripling the frequency of the laser and reducing the wavelength to approximately one-third of a micron.

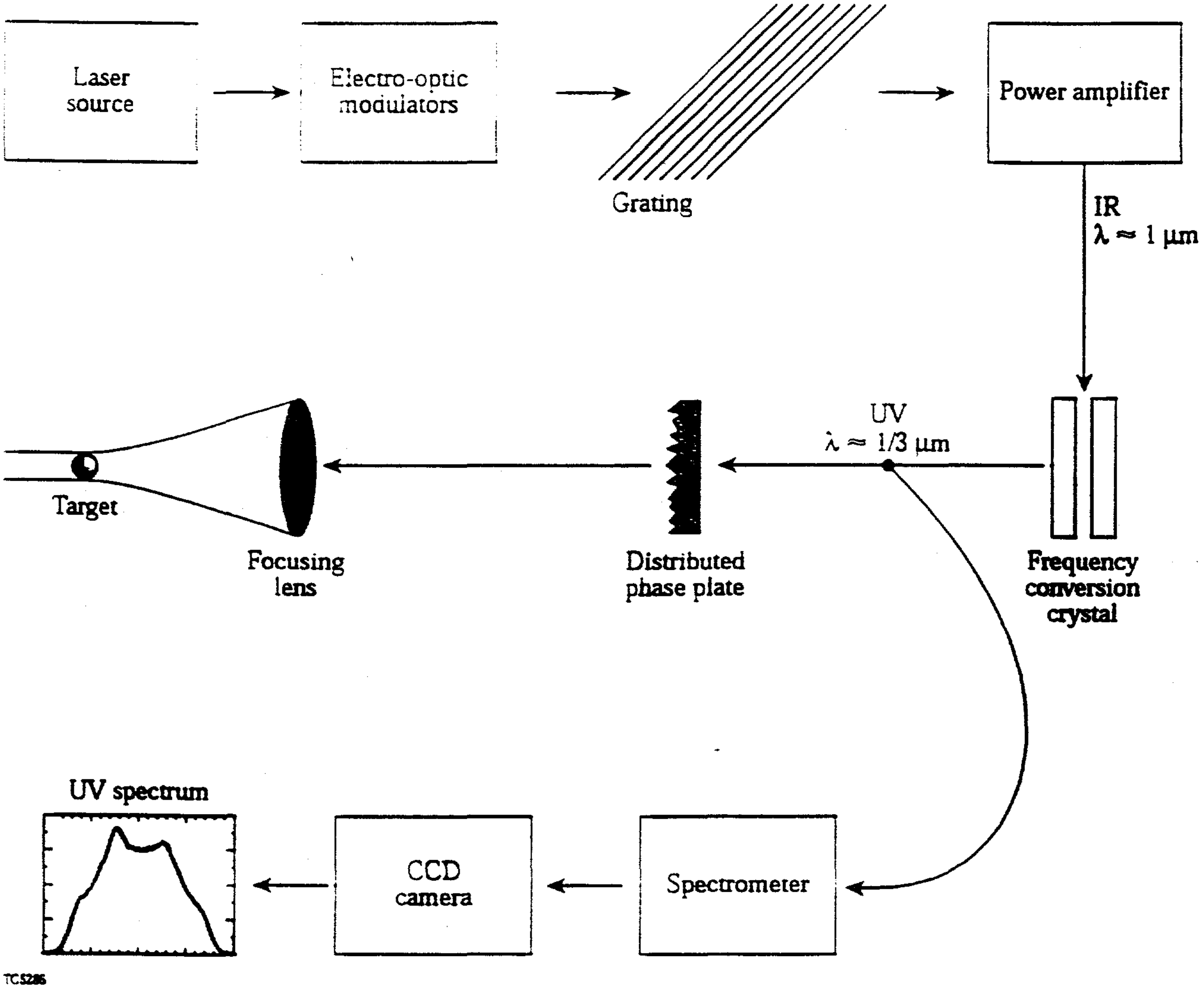

Fig. 1. Schematic of the experimental layout of OMEGA.

Once the laser beam has gone through the frequency conversion crystals, it goes through a distributed phase plate (DPP). A DPP uses frosted glass to smooth out some of the nonuniformity on target that would otherwise be present by producing a highly modulated intensity structure (speckle pattern), formed by the interference of light that has gone through different portions of the phase plate (Fig. 2 a) (2).

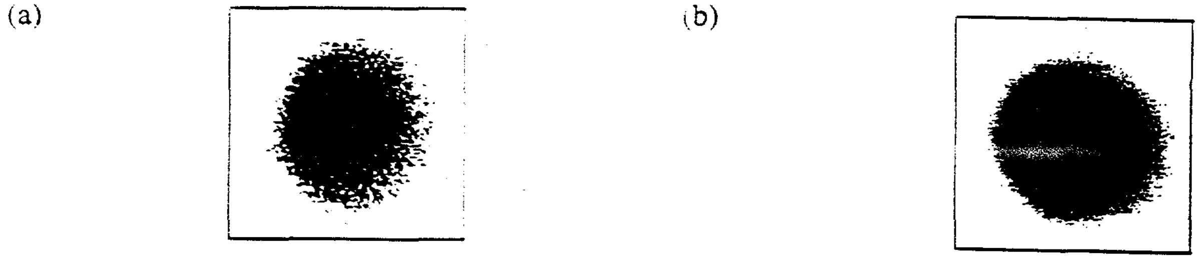

Continuous phase plate

2-D SSD

Fig. 2. (a) Spot uniformity on target using only the phase plates. The speckle structure evident in (a) is smoothed by SSD in (b).

Smoothing by spectral dispersion (SSD) is the primary mechanism used to average out these speckle patterns produced by the phase plate (3). SSD may be described as time-averaged smoothing (Fig. 3); the peaks of some speckles fill in the valleys of others to produce a smooth curve over a period of time.

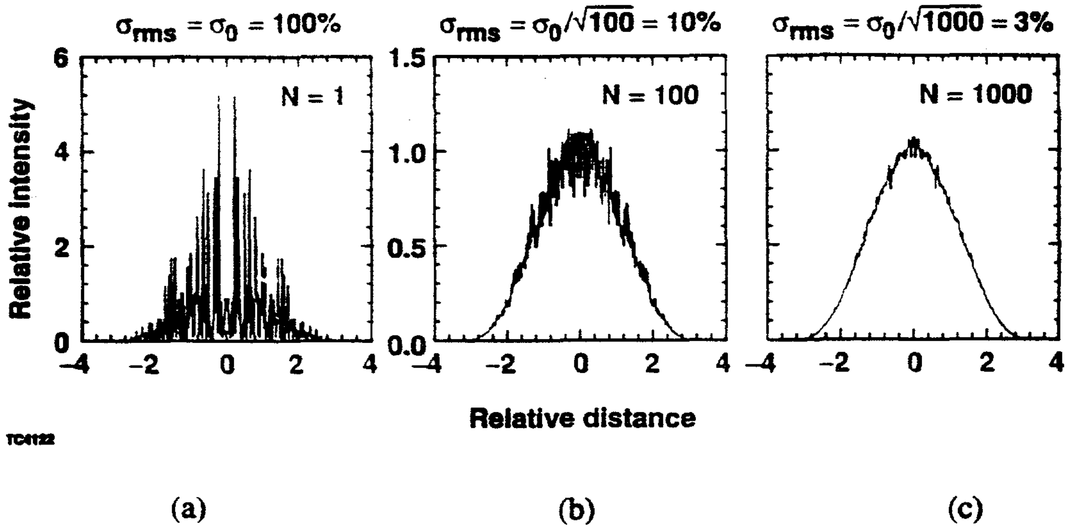

Fig. 3. Uniformity is proportional to $1/\sqrt{N}$, where N represents the number of speckle structures that have been overlapped. (a) shows the original speckle structure, (b) shows the uniformity achieved by overlapping 100 speckle structures and (c) shows the uniformity as a result of overlapping 1000 speckle structures.

To further understand SSD, refer to Fig. 1 where the laser beam is passed through an electro-optic modulator, which imposes a narrow spread of frequencies (bandwidth) upon the beam. This bandwidth is then spectrally dispersed using diffraction gratings. As the laser is frequency modulated by the system (the wavelength is sinusoidally oscillating in time about the fundamental wavelength), the speckle pattern moves about on target at rapid speeds, thereby averaging out the nonuniform speckle structure. In contrast with the speckle structure seen in Fig. 2a, the pattern in Fig. 2b is a lot more uniform as a result of SSD.

Currently, a diagnostic on three of the laser beams on OMEGA is used to measure the experimental spectrum (Fig. 1) after the laser beam has gone through the KDP frequency conversion crystals. Part of the laser beam is picked off using an optical fiber, which is then passed through a spectrometer which breaks up the beam into all of its individual frequencies. The final spectrum, which measures the intensity of each wavelength in the beam, is then imaged on a CCD camera.

For the first time, a theoretical model of the UV experimental spectrum with SSD has been constructed. This model is based on parameters measured at the beginning of the system and will serve three main purposes for the OMEGA laser system: 1) It will ensure that all the bandwidth put on the beam by SSD is successfully passing through the system. 2) At various stages through the system, the laser is passed through pinholes which intercept rays not following a straight path. When the laser beam goes through the diffraction gratings (Fig. 1), each individual frequency in the beam gets a different angle or tilt, consequently giving each beamlet its own path. Some of these beamlets can be cut off by the pinholes if they are not following the correct path. These frequencies that are cut off by the pinholes can now be measured by comparing the experimental spectrum with the theoretical model, as each angle corresponds to a specific wavelength on the spectrum. 3) When the laser beam is converted from the IR to the UV, the efficiency of conversion changes with changing wavelength. It is important that the KDP crystals are aligned correctly in order to get maximum conversion efficiency. Theoretical models of the laser spectrum that incorporate the correct electric field after it has been frequency converted will help monitor the alignment of the frequency conversion crystals.

Theoretical modeling of the UV Laser Spectrum

Two different approaches were tried to simulate the UV laser spectrum. the histogram method and the Fourier Transform method. The histogram method describes the laser beam as a cylinder of light: each point in the beam has its own wavelength and frequency. This program is useful to see how the spectrum evolves in time. The Fourier Transform method describes the laser beam as a complex electric field. This model gives a much more accurate fit to the experimental spectrum.

(a) Histogram method

In the first method, the laser beam is considered a cylinder of light: it can then be divided into a large number of spatial and temporal elements. The OMEGA system is not a single-frequency laser when SSD is on; the pulse has a range of frequencies across it and each distinct point in the beam has a different frequency and consequently a different wavelength. The model program scans across the laser beam spatially and temporally and computes a frequency and a wavelength at each point.

$$\Delta\lambda = \Delta\lambda_x + \Delta\lambda_y, \text{ where} \tag{1}$$

$$\begin{aligned} \Delta\lambda_x &= \Delta\lambda_{x0} * \cos(\omega_x * t + \alpha * x + \phi_x) \\ \Delta\lambda_y &= \Delta\lambda_{y0} * \cos(\omega_y * t + \beta * y + \phi_y) \end{aligned} \tag{2}$$

In Eq. (2), $\Delta\lambda_{x0}$ and $\Delta\lambda_{y0}$ are the bandwidths in the x and y directions, ω_x and ω_y are the two modulation frequencies that SSD imposes on the laser beam. α and β are proportionality constants that give the variation of wavelength across the beam, and ϕ_x and ϕ_y represent the absolute phases of the electro-optic modulators. The final model of the spectrum is a histogram of the different wavelengths across the whole pulse, and the spectrum describes the intensity of each wavelength present in a given beam.

The program has eight important input parameters: $\Delta\lambda_{x0}$ and $\Delta\lambda_{y0}$, ω_x and ω_y, α_x and α_y, and ω_x and ω_y. A triple nested loop is used to scan over time and the two spatial coordinates to compute a λ at every point in the laser beam. The final model of the UV spectrum is the aggregation of the different λs across the whole beam. To get reasonable accuracy, the laser beam must be divided into at least 500 time intervals, and into more than 100 elements in each spatial coordinate (x and y). For each time division, the program scans through the spatial coordinates and returns an array of computed λs across the beam. These arrays are then individually weighted by the temporal and spatial intensity profiles, and plotted using a histogram function. By using this algorithm, we can see how the spectrum is evolving in time as the pulse shape and the modulation frequencies are varying. The simulated model is then weighted by theoretical models of KDP conversion efficiency.

I have described that the laser beam has a spatial and temporal intensity profile. The temporal profile is dependent on the pulse shape being used and can be measured experimentally; the spatial intensity profile is modeled using a high order Gaussian function:

$$I\,(x,y) = \exp\ \{\ -(r/r_0)^{(1+\Lambda)}\ \}, \tag{3}$$

where $\Lambda = 10.0$, r describes the radius of the laser beam and r_0 is a given point in the beam.

A comparison between theory and experiment as shown in Fig. 4 shows that the two spectra have fundamentally similar shapes. The model simulates the two peaks of the spectrum at the same wavelengths with reasonable accuracy, and predicts the correct amount of bandwidth, as seen in the experimental spectrum. The model, however, doesn't account for three important properties of the experimental spectrum. 1) The experimental spectrum has a certain asymmetry between its peaks whereas the simulation does not, 2) the two peaks of the model are much sharper and narrower than what is experimentally observed, and 3) the model predicts a much sharper drop at the two ends of the spectrum, but the experiment has a gradual drop-off to zero.

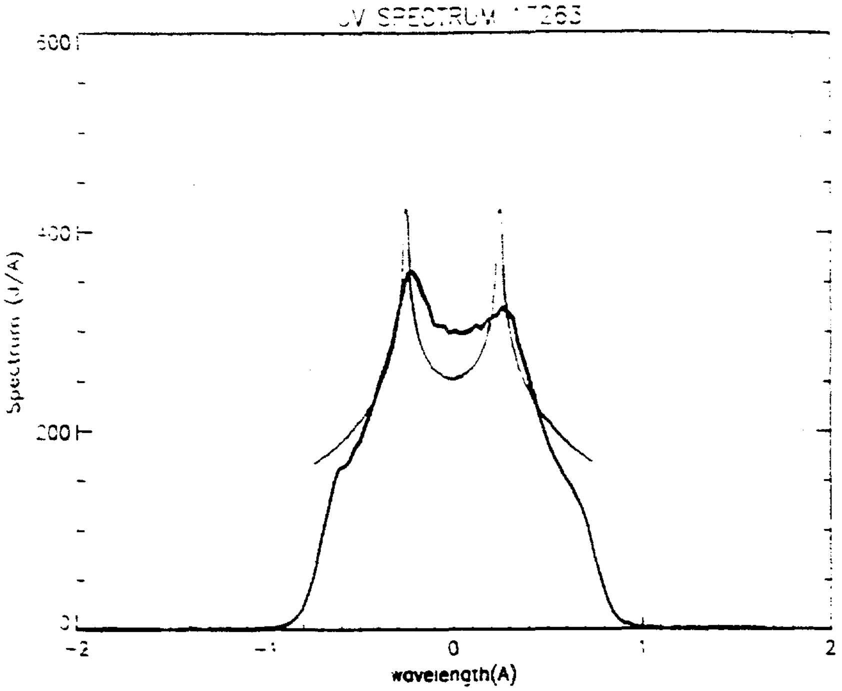

Fig. 4. The computer simulation (thin line) using the histogram method and the experimental UV spectrum (heavy line) . Notice that although the two seem to have fundamentally similar shapes, the simulation does not account for certain important features observed in the experiment.

(b) Fourier Transform method (FFT)

In the Fourier Transform method, the laser beam is described as a complex electric field as shown in Eq. (4):

$$E(t) = A(t) * \exp \{ i (3\delta_x * \sin(\omega_x * t + \phi_x) + 3\delta_y * \sin(\omega_y * t + \phi_y)) \} \qquad (4)$$

where the real part of the electric field A(t) is a function of the temporal intensity profile (pulse shape) I(t), given by:

$$A(t) = (2 * I(t) * c * \eta)^{1/2}. \qquad (5)$$

Here c is the speed of light, and η is a proportionality constant. The imaginary part of the electric field is dependent on δ_x and δ_y which represent the modulation depths of the laser. In Eq. (4), ω_x and ω_y represent the modulation frequencies and ϕ_x and ϕ_y are the absolute phases of the modulators. The individual Fourier components of the laser spectrum are described as the FFT of the electric field (4) into the frequency domain:

$$E(\omega) = \int E(t) * \exp(-i*\omega*t)\, dt \qquad (6)$$

As shown in Fig. 5 in black, the Fourier Transform of the electric field gives us the individual Fourier components that describe the spectrum. To simulate the experimental spectrum from these Fourier components, one must account for the response of the instrument being used to measure the experimental spectrum.

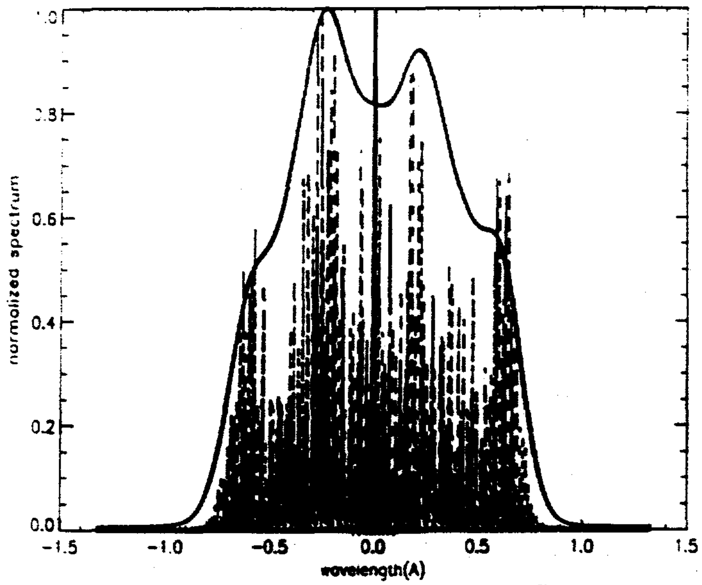

Fig. 5. Fourier components (dotted lines) of the complex electric field in the time domain. The Fourier components are convolved with the instrument response (heavy vertical line at λ 0.0 A) to give the UV spectrum. The instrument response is quite narrow for a given experimental set-up. It may change if the experimental layout is adjusted.

When a beam of light with bandwidth is passed through a spectrometer, it breaks up the beam into all the different frequencies present. The experimental spectrum measured by the spectrometer describes the intensity of each individual frequency. While simulating the spectrum, one must account for the way the spectrometer measures a single frequency, which may change drastically based on the experimental set-up being used to measure the spectrum. For example, if the focussing lens used to focus the beam into the spectrometer is adjusted slightly, the beam will come to focus at a slightly different spot inside the spectrometer, thereby changing how the spectrometer measures each frequency present in the beam.

The most important component of the algorithm, therefore, is to convolve the measured response of the system with the individual Fourier components of the electric field to simulate the spectrum (Fig. 5). The instrument response must be measured on the spectrometer being used to image the experimental spectrum to ensure accuracy. Trying to model the response of the instrument can be a major source of error as the response can change drastically for even small changes in the experimental set-up. Initially, the instrument response was modeled as a sinc function for a particular alignment of the lenses used to image the experimental spectrum, but it was later found that this only works for that particular set-up.

When using a Fourier Transform routine, it is important that the number of data points chosen be a power of two, as FFT algorithms are most efficient this way. Also, it is important to choose enough data points so that the calculated spectrum converges.

The results show that there is close agreement between experiment and theory (Fig. 6). This is the first time a theoretical model of the ultraviolet OMEGA laser spectrum has been made. It can accurately simulate the spectrum for any shot on OMEGA given the parameters at the beginning of the system, and it can account for nuances such as the gradual drop-off to zero near the ends of the experimental spectrum. This is of importance because it confirms that all the bandwidth on a pulse is successfully passing through the system, and that none of the frequencies are cut off by the pinholes that the beam has to pass through. The new system to be implemented on OMEGA is moving to higher bandwidths by adding a second tripler to the KDP frequency conversion crystals (5,6), using a sheme proposed by Eimerl (7). When the bandwidth is tripled, the computer simulation will be even more valuable as it will be a primary diagnostic to check if the extra bandwidth is successfully passing through the system.

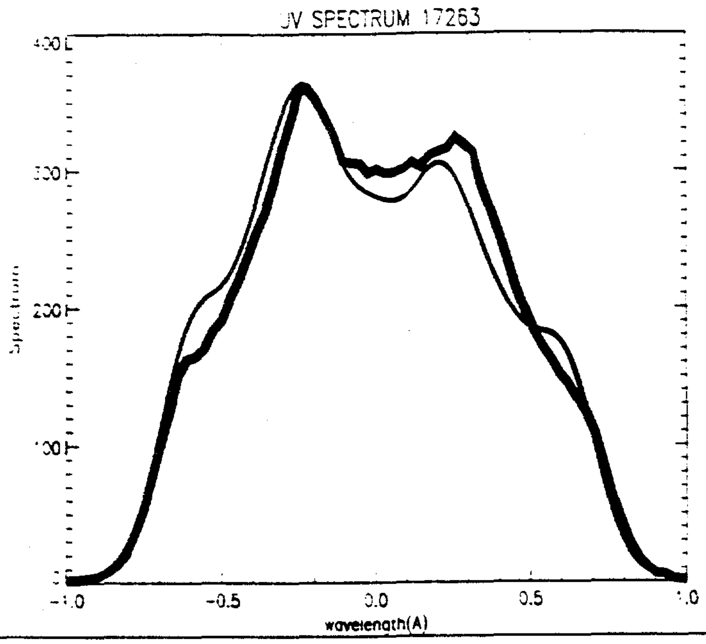

Fig. 6. Comparison between theory (heavy) and experiment (thin) using FFT routines for the 1-ns flat pulse on OMEGA.

In Fig. 6, the peak at the shorter wavelength is higher compared to the peak at the longer wavelength. The simulation model accounts for this asymmetry in peaks by taking into account the effect of frequency conversion while simulating the spectrum. I describe this in greater detail in a later section. I have found that by adjusting the phases of the modulators, the shape of the spectrum may change. I have used this to find the model that best fits the experimental spectrum.

Effects of the Phase Modulators

An interesting result of the simulations using FFT routines is the effect of the phases (ϕ_x and ϕ_y) of the modulators. From Eq. 4, the imaginary part of the electric field that describes the laser spectrum is a function of δ_x and δ_y (modulation depths), ω_x and ω_y (modulation frequencies) and ϕ_x and ϕ_y (absolute phases of the modulators). Currently on the OMEGA system, the modulators are not synchronized to the laser (time zero corresponds to the start of the laser pulse), thereby producing a set of random phases on every shot. The modulation depths and the modulation frequencies, however, are measured on each shot at the beginning of the laser system. It is generally believed that phase-locking the modulators has no effect on the final spectrum. Results, however, have shown that this is not always true. The phase does seem to average out for relatively long pulses (< 6 nanoseconds), but for a short pulse such as the 1-ns flat pulse used frequently on OMEGA, the phase of the modulators can make a prominent difference (up to 4 %) to the shape of the spectrum (Fig. 7). This finding suggests that the modulators should be phase-locked for the shorter pulses.

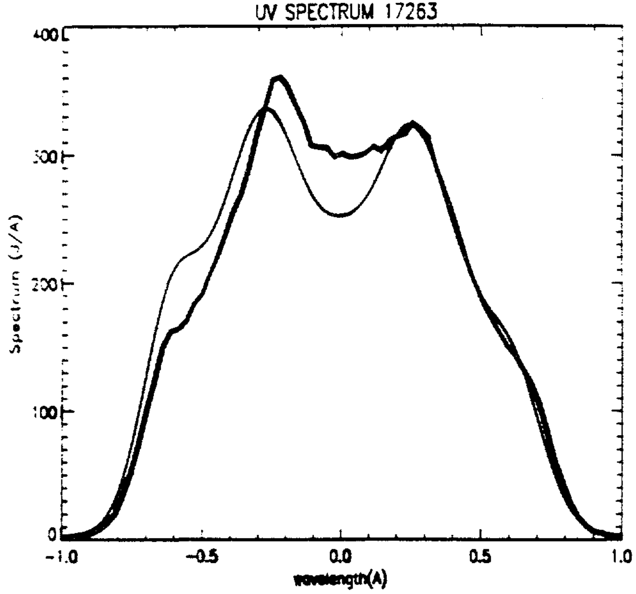

Fig. 7. As Fig. 6 but with different phases of the modulators. The model (thin line) changes considerably when the phases of the modulators are varied. Here the model uses ϕ_x = 1.33 radians and ϕ_y = 5.45 radians, whereas in Fig. 6, ϕ_x and ϕ_y were both 0.0 radians.

Frequency Conversion

The OMEGA laser system uses KDP frequency conversion crystals to convert from the IR to the UV. Two KDP crystals, a doubler and a tripler both with a 12 mm. thickness, are adjusted to achieve maximum efficiency in frequency conversion. On the new system to be implemented on OMEGA, a second tripler will be added so as to frequency convert three times more bandwidth than is converted on the current system (5). My results are based on a beamline on which the dual triplers have been implemented. As the tilt between the crystals is related to the frequency conversion efficiency for a given wavelength, FFT routines that incorporate the correct electric field after it has been frequency converted can help monitor the alignment of these KDP crystals by comparing experimental spectra with computer simulated models.

Frequency conversion efficiency on OMEGA is different at different wavelengths (Fig. 8, taken from Ref. 8). Recent shots on OMEGA show that the peak in the spectrum at the shorter wavelength (-0.3 angstroms, see Fig. 6) is always higher than the peak at the longer wavelength (0.3 angstroms). Computer simulations (Fig. 8) concur with experiment; the frequency conversion efficiency decreases by approximately 12 % between -0.3 angstroms and 0.3 angstroms for the beam-lines with a second tripler, thereby imposing a skew in the spectrum (Fig. 6).

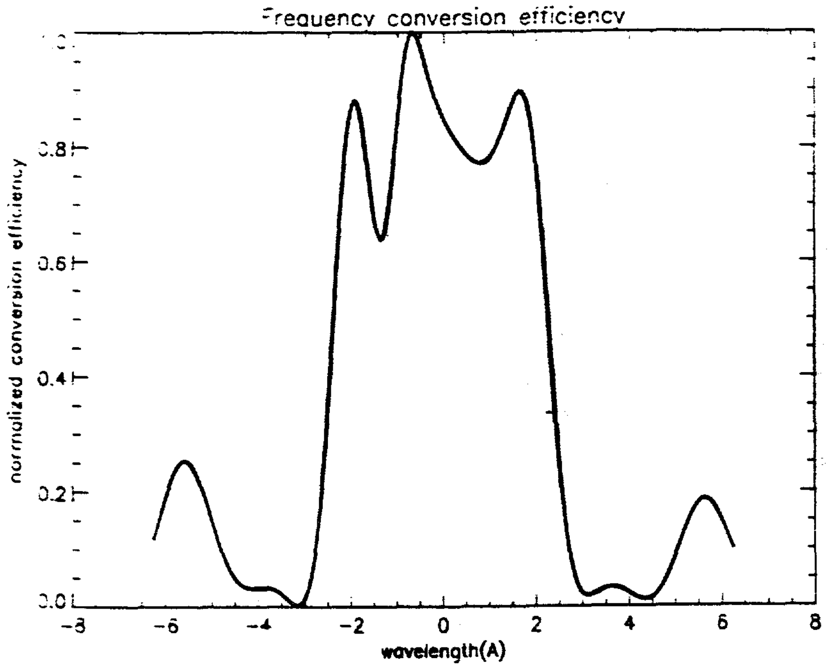

Fig. 8. Predicted frequency conversion efficiency for a representative intensity on OMEGA for the dual triplers implemented on some of the beamlines.

The effect of frequency conversion efficiency (≈ 12 % difference between the 2 peaks on the spectrum) dominates the effect of the absolute phase of the electro-optic modulators (≈ 4 %). Thus, when frequency conversion is accounted for in the simulation model, the peak at the shorter wavelength is always higher than the peak at the longer wavelength in agreement with what is observed.

Future Work

The close agreement between theory and experiment provides confidence in the use of Fourier transform algorithms to simulate and compare with experiment the ultraviolet laser spectrum with SSD of all sixty beams that comprise the OMEGA laser system. Currently, the spectrum for only three of the sixty beams in OMEGA is measured using a spectrometer. I have done research into designing an optical system that can measure the spectra for all the beams using the minimum number of spectrometers possible, and I have found that all sixty beams can be measured using only two spectrometers. Unfortunately, however, the CCD camera used to image the experimental spectrum imposes some distortions on the spectra imaged away from the central axis of the camera. These optical distortions can possibly be corrected by designing programs that can characterize and undo the distortion as has been done with some of the streak cameras used in the OMEGA system.

Conclusion

This is the first time that a theoretical model of the ultraviolet laser spectrum with SSD has been constructed. The close agreement between experiment and the computer simulations provides confidence in the use of the model to analyze the spectrum of all sixty beams that comprise the OMEGA system. Ensuring that an accurate spectrum is obtained on every shot will confirm that SSD is functioning correctly, and thus ensure smooth spots on target. We will also be able to verify that all the bandwidth on the pulse is successfully passing through the system, and that none of the frequencies are cut off by the pinholes. Computer simulations will also help in monitoring the alignment and tilt of the KDP frequency conversion crystals and aid in further exploring the effects of the phases of the modulators.

References

1. R. S. Craxton. R. L. McCrory. J. M. Soures. "Progress in Laser Fusion." Scientific American, vol. 255. Aug. 1986.

2. Y. Lin. T. J. Kessler. and G. N. Lawrence. "Design of continuous surface-relief phase plates by surface-based simulated annealing to achieve control of focal-plane irradiance," Optics Letters, vol. 21, 1703, Oct. 1996.

3. S. Skupsky and R. S. Craxton . "Irradiation Uniformity for High-Compression Laser Fusion Experiments," Physics of Plasmas. vol. 6. 2157. 1999.

4. Ronald N. Bracewell. "The Fourier Transform and Its Applications," second edition, (McGraw-Hill Book Company, New York. 1986).

5. Steven Oskoui, "Group Velocity Effects in Broadband Frequency Conversion on OMEGA," 1996 Summer Research Program for High School Juniors at the University of Rochester's Laboratory for Laser Energetics (1996).

6. A. Babushkin. R. S. Craxton, S. Oskoui, M.J. Guardalben, R.L. Keck, and W. Seka, "Demonstration of the dual-tripler scheme for increased-bandwidth third-harmonic generation," Optics Letters, vol. 23, 927, June 1998.

7. D. Eimerl, J. M. Auerbach, C. E. Barker, and D. Milam, "Multicrystal designs for efficient third-harmonic generation." Optics Letters, vol. 22, 1208, 1997.

8. R. S. Craxton, private communication.

Acknowledgments

I would like to specially thank my research advisor, Dr. Donaldson, for spending his time and effort to help me achieve my results and Dr. Craxton for giving me this remarkable opportunity at the

LLE and for helping me with my research project. I also appreciate the help of J.Larkin, R. Bahr, Dr. Perkins and Dr. Marozas. Finally, I would like to tell all the other participants in the program how much I enjoyed their company and friendship; I will miss you all dearly.

Characterization of the Liquid Crystal Point-Diffraction Interferometer

Lutao Ning
Brighton High School

Advised by Mark Guardalben

University of Rochester
Laboratory for Laser Energetics (LLE)
1999 Summer High School Academic Research Program (SHARP)

Abstract

This project analyzes the applicability of the liquid crystal point-diffraction interferometer (LCPDI) as an accurate error detection device. An interferometer is a device that detects wavefront aberrations in light waves. The LCPDI has many advantages over commercial interferometers including common-path design, self-referencing nature, phase stepping ability, and economic efficiency. Before the LCPDI can be implemented on the OMEGA laser system, the largest laser in the world, it must be characterized, calibrated and benchmarked against a commercial interferometer. This study analyzed the inherent error of the LCPDI and benchmarked the LCPDI against the industry standard interferometer Zygo Mark IV XP.

1. INTRODUCTION

With world energy supplies at a limit, a new source of energy must be developed. Scientists at the University of Rochester's Laboratory for Laser Energetics are working tirelessly to develop laser fusion, a possible solution to the finite resources available to the world. OMEGA, the primary laser at LLE, is a 60-beam system that is transmitted and amplified through thousands of optics. The immense power of the laser would destroy commercial optics. Even the special neodymium amplifiers custom made for OMEGA are susceptible to damage with any misalignment or aberrations in the system. Shots on target stress uniformity and any perturbations in the system could cause non-uniform energy distribution on target.

Interferometers, such as the liquid crystal point-diffraction interferometer (LCPDI) can be used to detect such perturbations. LCPDI is small, economic, robust and has built in phase shifting abilities. The LCPDI is of common-path design and self-referencing, making it less sensitive to environmental disturbances such as mechanical vibration, temperature fluctuations, and air turbulence. Before implementing the LCPDI in the OMEGA system, however, it must be calibrated, characterized and compared to an industry standard interferometer. A known aberration was measured using the LCPDI and the Zygo Mark IV XP interferometer. The comparison between the two measurements shows the LCPDI to be an effective substitute to the more expensive Mark IV.

2. The LCPDI

2.1 Physical description and background

An interferometer is a device that splits a light beam into two beams, and then recombines them to form interference patterns. The LCPDI (Fig. 1) consists of two glass windows (G) coated with Indium Tin-Oxide(ITO), liquid crystal (LC) fluid between the two windows, a glass sphere (GS) in the middle of the LC fluid and two leads (E) connected to the windows. Light focused on the glass sphere will split into two beams since the index of refraction around the sphere is different from that of the sphere. The light propagating through the sphere is the reference beam while the light going around the sphere is the object beam. The minute portion of the original wave front that comprises the reference beam represents a point source, a perfect wave front to which the original wave front is compared. In the ideal LCPDI, the reference and object beams are of equal intensity, resulting in perfect contrast in the interferogram. To produce this desired effect, a dye is added to the liquid crystal, which absorbs some of the intensity of the object beam since it is thousands of times more intense than the reference beam[1].

Figure 1 The LCPDI

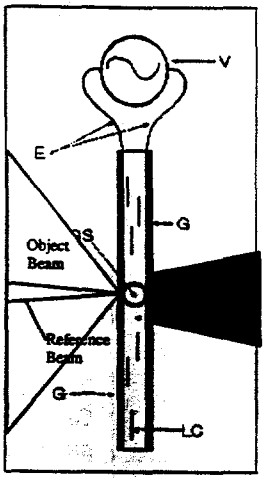

The liquid crystals have two distinct indices of refraction, and rotate between the two indices as a function of voltage. The ITO coating creates a conductive surface on the glass, allowing voltage to be applied to the liquid crystal between the glass windows. With applied voltage (V), the index of refraction of the liquid crystal will decrease, changing the interference pattern, thus giving the LCPDI phase-shifting abilities. The resulting interferogram at a point (x, y) can be represented by:

$$I_{tot}(x, y) = I_r + I_o + 2\sqrt{I_r I_o}\cos(\Phi + \alpha_r) \qquad (1)$$

where Φ is the phase difference between object and reference. I_r=reference beam intensity, I_o=object beam intensity and α_r is the rth phase shift.

2.2 Phase-shifting

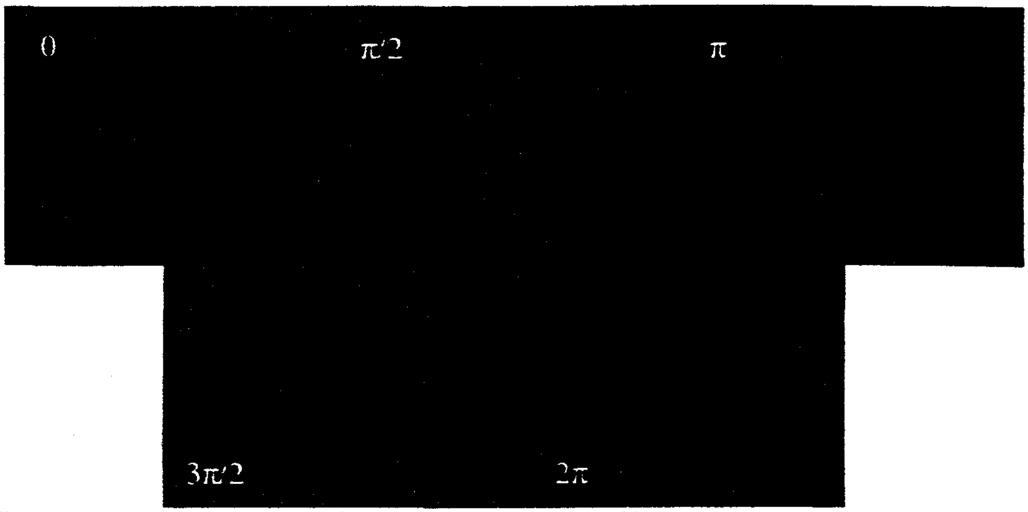

Figure 2 Adjusting the voltage from 0.98V to 1.21V, the fringes move an arbitrary scale of 2π. One interferogram leaves gaps in the fringes but compiling multiple interferograms into a phase plot allows scanning through the entire field of interest, improving spatial resolution

The phase-shifting abilities of the LCPDI coupled with the correct phase-shifting algorithm produces a higher spatial resolution of the wave front. With applied voltage, the fringes of the interferogram will move out or in, as shown in figure 2, depending on which side of focus the LCPDI is placed. The generalized phase shift algorithm to combine the interferograms into a phase plot is shown in equation 2. Specific algorithms depend on number of buckets (m), and algebraically calculated coefficients (a_r and b_r).

$$\Phi = \arctan\left[\frac{\sum_{r=1}^{m} b_r I_r}{\sum_{r=1}^{m} a_r I_r}\right] \qquad (2)$$

These coefficients depend on what kind of error the algorithm is trying to correct. The self-referencing and common path nature of the LCPDI provide for an instrument much less sensitive to environmental sources of error such as mechanical vibration, temperature fluctuation and air turbulence.

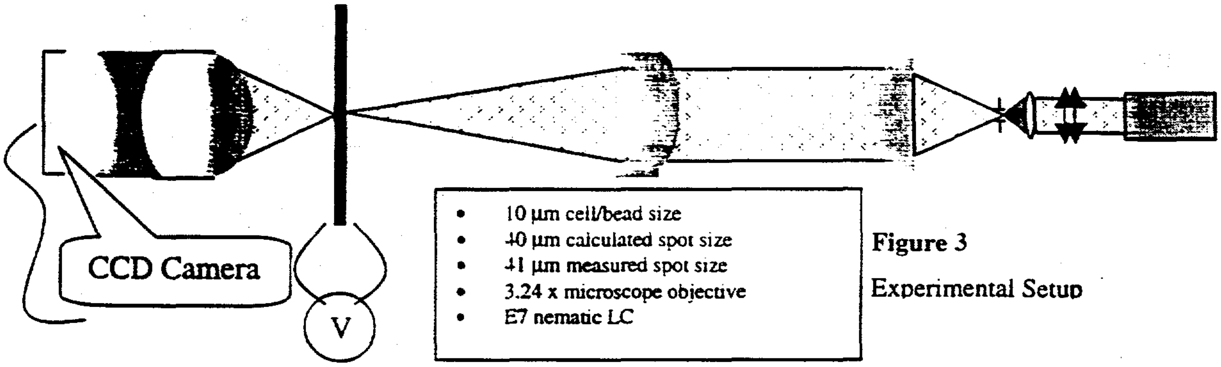

- 10 µm cell/bead size
- 40 µm calculated spot size
- 41 µm measured spot size
- 3.24 x microscope objective
- E7 nematic LC

Figure 3
Experimental Setup

2.3 Experimental Setup

The setup for my experiments is shown in figure 3. It begins with a 543 nm HeNe laser. The laser beam enters two cross polarizers, which are used together to adjust the intensity. A microscope objective focuses the light down to a pinhole, which acts as a spatial filter, filtering out high frequency noise from the light. The filtered light enters a Plano-convex lens, which collimates the beam followed by a doublet, which focuses the beam down to the LCPDI. The LCPDI used in my experiments was made with a 10µm glass bead, E7 nematic liquid crystal and oil red O dye (absorbs 543 nm light). From the LCPDI, the light passes through a zoom lens that images the area between the doublet and Plano-convex lenses. This region of the interferometer is called the cavity. A test piece whose optical wavefront quality is to be characterized is placed within the cavity and measurements were taken, as described in section 3. The zoom lens images the interference pattern onto a CCD camera for later processing by a computer.

3. EXPERIMENTAL RESULTS

3.1 Empty Cavity Measurements

After setting up the experiment, multiple sets of empty cavity measurements were taken. The five-bucket algorithm[2] (Eq. 3) chosen to calculate the wavefront of the empty cavity required five interferograms shifted by $\pi/2$ intervals (middle of fringe to edge or vice versa) from 0 to 2π. Before measurements were taken, the voltage shift required for the fringes to move through each $\pi/2$ interval was determined. Each cavity measurement consisted of five images at each of the five predetermined voltages. To reduce stochastic noise contributors such as thermal fluctuation, mechanical vibration and air currents, the five-bucket image acquisition and subsequent wavefront calculation using equation 3 was

$$\tan\Phi = \frac{2(I_3 - I_1)}{I_4 + I_0 - 2 \cdot I_2} \qquad (3)$$

performed ten times and the average wavefront determined. Five minutes later, ten more five-bucket measurements were captured, averaged, and subsequently subtracted from the previous set's average. What remained was the limit to the accuracy of the LCPDI device. Figure 4 shows the general form of this residual error.

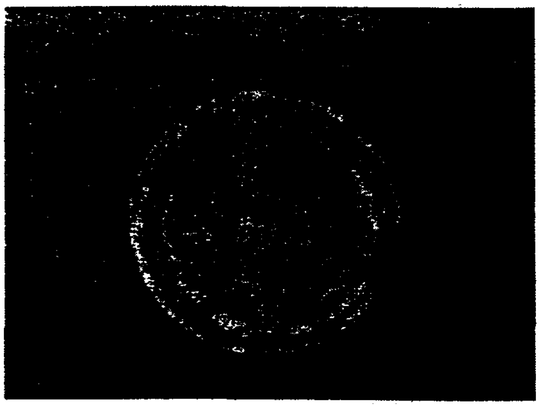

Figure 4 The residual error in the LCPDI system

3.2 Optimizing Experimental Configuration

Several factors determine the accuracy of the LCPDI including focusing condition, lateral position and voltage regime. A series of benchmark tests were conducted to determine which parameters would produce the least residual error. Cavity measurements were taken at three focus distances to determine a focusing condition with the least residual error. The focus distance determines the number of fringes in the interferogram: the farther from focus, the more fringes in the image. After finding the focal point of the doublet lens using a knife edging technique, the LCPDI was moved away from this focal point in the propagation direction until there were 3-4 fringes in the interferogram. Distances for the duration of these experiments were referenced to the focal point of the doublet lens. A set of 10 empty cavity measurements was taken, and then another set was taken 5 minutes later and residual error calculated, as detailed in 3.1. The procedure was then repeated at two other focal distances, one corresponding to 8-9 fringes and the other at the focal point of the doublet lens. The residual error at the different focusing conditions was compared. The set that gave the best results was at 3-4 fringes with a peak-to-valley residual error of 0.049 waves, which was half the peak-to-valley of the other results.

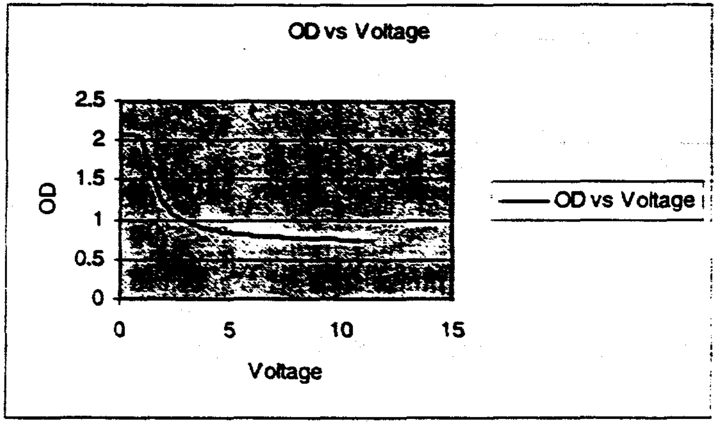

Figure 5 OD significantly drops and levels off at voltages higher than 4 volts.

After finding the most favorable focusing condition, cavity measurements were taken at two separate voltage regimes to determine the voltage regime with the best residual error. The dye inside the LCPDI is dichroic and the optical density (OD) drops to 0.8 at voltages higher than 4 volts (ideally, the OD is 2.0). Two sets of 10 measurements were taken for each voltage regime at the best focusing condition. The lower voltage regime produced a much better result than that of the higher voltage regime, again with a peak-to-valley half as large as the other. The final testing conditions placed the LCPDI at a focus distance between 0.93 and 1.17 cm from best focus at a low voltage regime (under 3 volts).

3.3 Error Correction

After finding the best focusing and voltage conditions, the peak-to-valley of the residual error was 0.049 waves. This was the same as the residual error found with the best focusing condition because all the measurements taken for focusing condition were performed at the lower voltage regime. Although the experiment did not occur on an airbed, we did cover it with a plastic wrap to reduce air currents. The final phase averages had two dominant types of residual error, one that occurred at twice the spatial frequency of the fringes and another that occurred at the same spatial frequency as the fringes. We experimented with several methods to reduce this error. First, a different five-bucket algorithm was chosen[3] (Eq. 4). The new algorithm divided each

$$\tan\Phi = \frac{\Delta I_3 - \Delta I_1}{\Delta I_4 + \Delta I_0 - 2\cdot\Delta I_2} \bullet \frac{\sqrt{I_{0obj}} + \sqrt{I_{4obj}} - 2\cdot\sqrt{I_{2obj}}}{\sqrt{I_{3obj}} - \sqrt{I_{1obj}}} \qquad (4)$$

$$\tan\Phi = \frac{\sqrt{3}(5I_1 - 6I_2 - 17I_3 + 17I_4 + 6I_5 - 5I_6)}{(I_1 - 26I_2 + 25I_3 + 25I_4 - 26I_5 + I_6)} \qquad (5)$$

$\Delta I_r = I_r - I_{robj}$

I_{robj}=Object beam intensity of rth phase step

interferogram by a background image taken at the same voltage, which corrected for intensity change due to voltage change. This produced better peak to valley, but did not eliminate either source of ringing. We then tried a six-bucket algorithm[4] (Eq. 5) designed to reduce the effect of spatially non-uniform phase shifts. The result did not show a significant improvement, although a more careful experimental approach may be necessary. The problem was then approached through Fourier filtering, which removed both sources of ringing, but also removed data from the area of interest. The method cannot be applied since the filtering could be removing an aberration that the device is actually trying to detect. Finally, a phase-offset technique was used to reduce the error occurring at twice the frequency of the fringes. This proved very successful at reducing this spatial frequency component, but the phase error occurring at the fringe frequency still remained. This technique further reduced the peak-to-valley of the residual phase error to around 0.04 waves.

3.4 $\pi/2$ Offset Technique[5]

Consider a sine wave of period π; averaging that wave with one of equal magnitude shifted $\pi/2$ will cause the peaks and valleys of the two waves to cancel each other, leaving a straight line. Since one source of residual error was at twice the fringe frequency, the periodicity of that source of error is π. Averaging a phase plot with one whose ripples are of equal magnitude and offset by $\pi/2$ will eliminate that rippling. By first taking a set of data, then shifting the starting point to the former set of data's $\pi/2$ voltage, this offset is achieved. The method worked very well and virtually eliminated the error occurring at twice the frequency. Figure 6 shows a phase plot before and after correction.

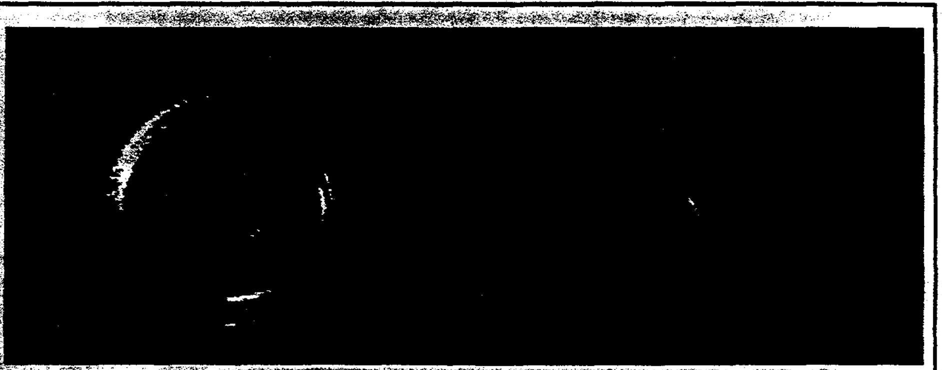

Figure 6 Image 6A shows a phase plot without offset correction while image 6B shows a phase plot with the offset correction. The elimination of the error occurring at twice the frequency of the fringes is evident in the second image.

3.5 Characterization of A Test Piece

The test piece was an optic with a shallow defect polished into it using the magnetorheological finishing technique[7]. The piece was placed in the cavity and ten sets of data were taken and averaged. Immediately after, ten empty cavity measurements were taken, averaged and subtracted from the average of the test piece data. The data collection was repeated to apply the phase-offset technique and the resulting average produced an accurate measurement of the aberration in the test piece. The aberration in the test piece was measured to be 200 nm deep in transmission, which closely compared with the measurement taken by the commercial interferometer Zygo Mark IV XP. The graph (Fig. 7) shows lineouts taken from the center of the defect while figure 8 shows the two images of the aberration generated by the two interferometers. The left side of the lineout for the LCPDI image matches remarkably well with

Figure 7 Lineouts of Commerical Interferometer and LCPDI

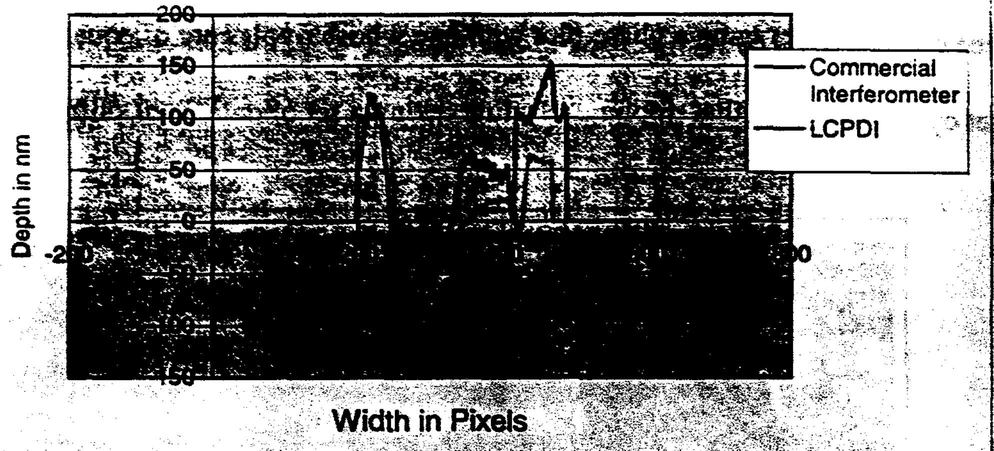

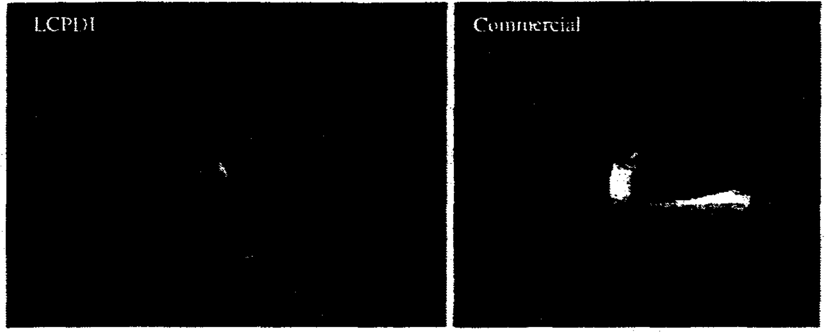

Figure 8 The LCPDI and the Zygo Mark IV XP measuring the same known aberration in a test piece.

that of the commercial interferometer. The high gradient is resolved very well and the depth of the trough polished into the test piece was accurately measured.

Several possibilities could describe why the LCPDI measurement does not match that of the Zygo as well on the right side of figure 7. The LCPDI does not have anti-reflection coating and reflection off the windows could create the erroneous interference. Future LCPDI devices will be made on substrates coated with AR coatings. Although the 2nd harmonic rippling was eliminated with the offset technique. the single harmonic still remained. The effects of the rippling can be seen around the phase plot in the LCPDI image (Fig. 8). The spike on the right side of the LCPDI lineout falls on one of these ripples. If this rippling can be removed without sacrificing data, a new comparison should show the LCPDI matching the Zygo better throughout the image. Finally, the computational method and error correction procedure implemented by the Zygo interferometer is relatively unknown to this study.

4. CONCLUSION

With the promising results obtained with this latest study, the LCPDI looks comparable to the commercial interferometer. It successfully resolved the peak and valley of a phase defect and produced a measurement that closely resembled that of the commercial interferometer Zygo Mark IV. This benchmark comparison suggests that the LCPDI can allow highly accurate wavefront characterization of the OMEGA laser system. The diagnostic system on OMEGA, the final destination of the finished product, operates in the infrared spectrum, at 1054 nm. At the time of the study, a dye that absorbs that wavelength of light was not available but a dye has since been developed and a LCPDI with promising optical density has been made. This LCPDI will be characterized and benchmarked using the same techniques as described in this study and an operational LCPDI will be implemented on OMEGA in the near future.

5. REFERENCES

1. Rao. R. "Computer Aided Modeling of the Liquid Crystal Point-Diffraction Interferometer," UR/LLE Student Research Reports. 1999.

2. Battaglia. D.J.. "Analyzing Aberrations in a Laser System using a Liquid Crystal Point-Diffraction Interferometer." UR/LLE Student Research Reports. 1997.

3. Mercer. C. "Liquid Crystal Point Diffraction Interferometer." NASA Technical Memorandum 106899. May 1995.

4. Jain. N.. "Analyzing Algorithms for Nonlinear and Spatially Nonuniform Phase Shifts in the Liquid Crystal Point Diffraction Interferometer." UR/LLE Student Research Reports, 1998.

5. Schwider. J. *et al.*. "Digital wave front measuring interferometry: some systematic error sources." Appl. Opt. 22. 3421-3432.

6. Magnetorheological finishing, University of Rochester Center for Optics Manufacturing, http://www.opticam.rochester.edu.

6. ACKNOWLEDGEMENT

First and foremost. I would like to thank my advisor, Mark Guardalben. He guided me through the program and gave me enough independence to do my own experiments. I would like to thank Dr. R.S. Craxton for running the program. This was an extraordinary opportunity to produce original research. I would also like to thank Devon Battaglia. the master of PV-wave, for giving me code to work with and helping me figure out this reclusive language. I would like to thank Ryan Brecker for showing me how the LCPDI is made and allowing me to help make one. Thanks to the IAL community of Peter Hopkins. Jyoti Kandlikar. Alice Tran, and Rohit Rao along with the rest of the summer students. This was great fun along with the hard work; plums forever guys. Finally, I would like to thank the sun. because if somebody didn't look up at the sun and think 'fusion'. there would be no laser lab.

LCPDI MODELING

Rohit Rao

Advisor: Dr. R. S. Craxton

Laboratory for Laser Energetics
University of Rochester

Summer High School Academic Research Program 1999

1. Introduction

The Omega laser. for the time being, is the world's most powerful laser. Its sixty beams are designed to deliver 60 Terawatts of power to a tiny target. Scientists use this laser to further human knowledge of laser fusion. Fusion is one of the oldest sources of energy, yet there is still much work to be done before it can be harnessed. The greatest problem faced is that of efficiency; the net output is a minuscule 1% of the energy put into the system. The NIF laser is being built at Lawrence Livermore to increase this efficiency tenfold. However, for the time being, other steps are being taken to improve the efficiency of the Omega laser.

2. Background

The LCPDI. or Liquid Crystal Point Diffraction Interferometer, was first conceived to diagnose aberrations in the beam of the laser. The Omega laser system contains thousands of optical pieces. many lenses and mirrors that all introduce imperfections into the beam. Using the LCPDI, one can theoretically scan the wave front and measure any imperfections in the beam. There are three main components to the LCPDI (see Fig. 1). Two glass windows serve to enclose the inner workings. Between the glass are sandwiched tiny glass spheres. While the glass measures over 1 mm in thickness. these spheres are no more than 20 μm in diameter. Finally, a liquid crystal solution fills in the rest of the space between the glass.

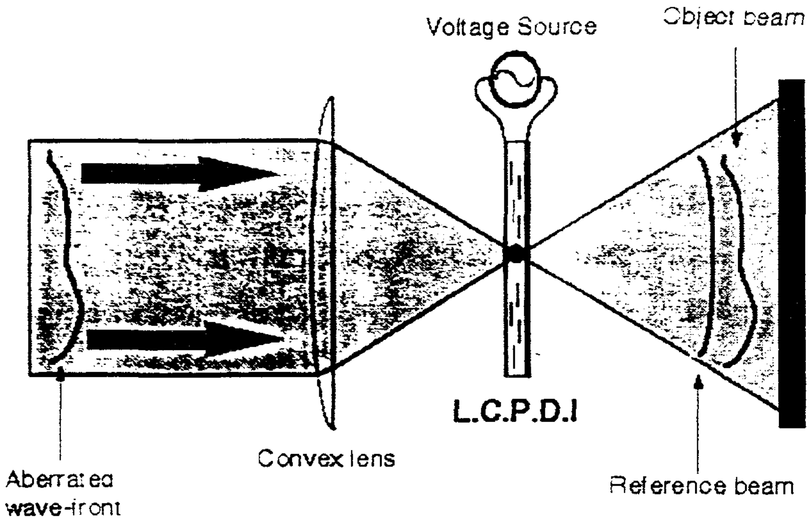

Figure 1: Diagram of the LCPDI—Portions of the incoming beam intersect the microsphere and form the reference beam while the majority miss it and form the object beam. These two beams form the interference patterns seen by the CCD camera.[1]

When light is passed through the LCPDI, it is split into two beams. The light rays that pass through the microsphere diverge greatly and form the reference beam. Since only a very small portion of the beam becomes the reference beam (typically around 5%), it can be assumed that the reference beam is free of aberrations. The other rays pass straight through the liquid crystals and compose the object beam. These two beams travel through space and interfere with each other. It is this interference that creates the circular fringe patterns seen by the CCD camera.

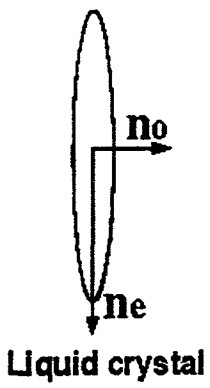

Figure 2: The index of refraction in one direction (N_E) is different than that in the other direction (N_O)[1]

The liquid crystal solution is an integral part of the setup. As the reference rays diverge, they lose much of their intensity. This loss of intensity leads to a loss of contrast in the final image: the interference patterns do not show up as well. The solution to this problem is to mix a dye in with the liquid crystals. This dye absorbs some of the intensity of the object beam, increasing the quality of the final image.

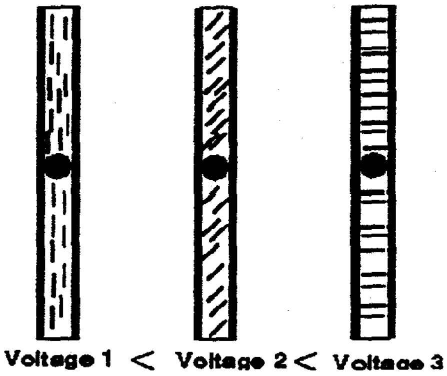

Figure 3: As a larger voltage is applied to the cell, the liquid crystal molecules rotate from, in this case, a vertical orientation to a horizontal orientation.

Liquid crystals exhibit birefringence. The index of refraction of the crystals in one direction is different than the index of refraction in the other direction. In Figure 2, N_E is equal to 1.73 while N_O is only 1.53. Liquid crystals also exhibit dielectric anisotropy. When a voltage is applied, the crystals rotate. By applying a voltage, scientists can phase shift the object beam, scanning its entire surface for aberrations. At one voltage, only portions of the wave can be seen. When the voltage is changed, different areas of the wave come into view. This effect is what makes the LCPDI a substantial improvement over what is currently on the Omega laser system. LCPDIs are also cheaper to produce and smaller than commercial interferometers.

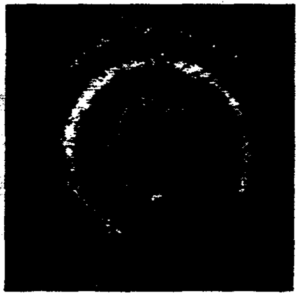

Figure 4: The above picture is a diagram of a wave under different voltages. Areas that were light under one voltage become dark under a higher one and can be scanned for aberrations.[2]

3. Modeling the LCPDI

In the summer of 1998, a program was written by Amy Turner[4] that traced the path of the rays through the LCPDI. The program tracks the rays from their starting point to the spot where they hit the camera. Snell's Law is used at every intersection between two different surfaces to determine the new direction that the ray will take. The program can display the rays graphically or in numerical form. Figure 5 is a graph produced by the program that shows the paths of the rays through the LCPDI. The closely spaced rays form the object beam while the other rays intersect the microsphere, diverge, and form the object beam. Included in the program is the ability to change the parameters of the experiment, which is helpful when comparing experimental and theoretical data.

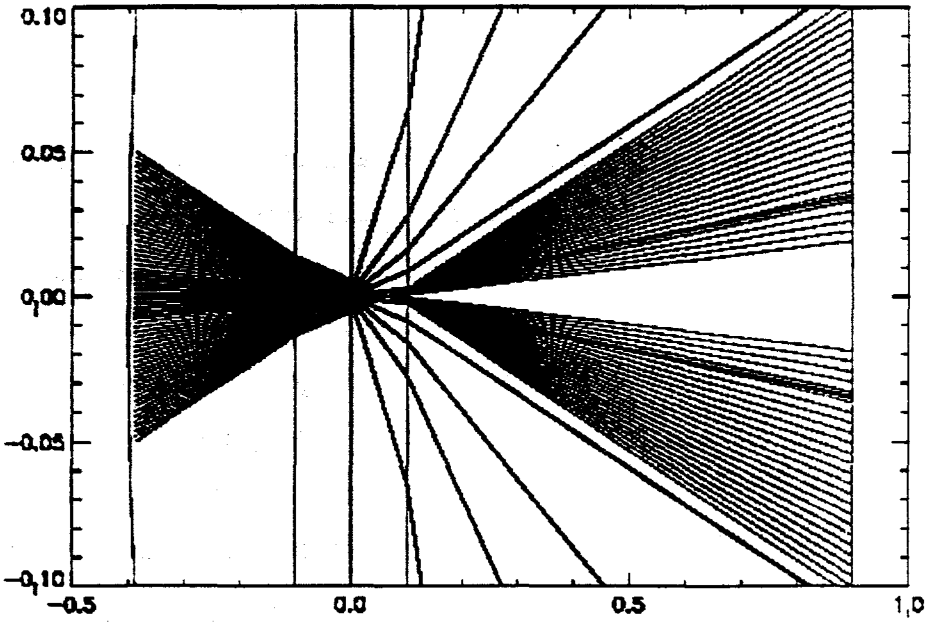

Figure 5: A graph created by Turner's program that displays the paths of the rays through the LCPDI. The closely spaced rays form the object beam while the other rays intersect the microsphere and form the reference beam.[4]

The program used the optical paths of the rays to calculate the interference patterns formed. The optical path of a ray is the sum of the distance traveled in each material multiplied by the corresponding index of refraction. It defines the phase of the ray and is calculated for each ray as it passes through the system. This difference in phase between the object and reference beams creates the interference patterns. The optical path is converted into waves by dividing by the wavelength of the laser. The difference of the path lengths for both beams is plotted by Turner's program and fringes are seen where it equals an integer value.

A problem with Turner's program was that it did not provide an easy way to compare experimental and theoretical data. While the graphs may visually look similar to the photos taken in experiments, they cannot be compared. One is a graph of the optical path difference, while the other is a photo of the intensity of the beam. Therefore, it was necessary to expand the program to calculate the intensity of the beam at each point on the front.

The intensity of the rays was calculated using the following equation:

$$E_{Total} = E_{10}e^{-i\phi} + E_{20}e^{-i\phi} \qquad (1)$$

The electric field of the beam is composed of a real portion and an imaginary portion. The real portion, E_{10}, is calculated from the intensity using equation 2.

$$I = \frac{1}{2\mu_o c}E^2 \qquad (2)$$

The imaginary portion, $e^{-i\phi}$, is calculated easily once it is known that ϕ is equivalent to $\frac{2\pi nz}{\lambda}$, where $\frac{nz}{\lambda}$ is equal to the optical path length. The electric fields of each beam are added together, and then the intensity is found using equation 2.

When plotted against the radius (position on camera), the intensity makes a graph similar to the one in figure 6. A lineout can be taken of the experimental images[3], creating a similar intensity versus radius graph. In this way, experimental data can be superimposed on the same graph as theoretical predictions, providing for an easy way to compare the two. A ratio of .00135 cm per pixel was determined to scale the data in the horizontal axis. The experimental data had to be normalized along the vertical axis, however, since there was no absolute scale of intensity that could be determined from the images. The horizontal positions of the fringes were what were taken into account when comparing data.

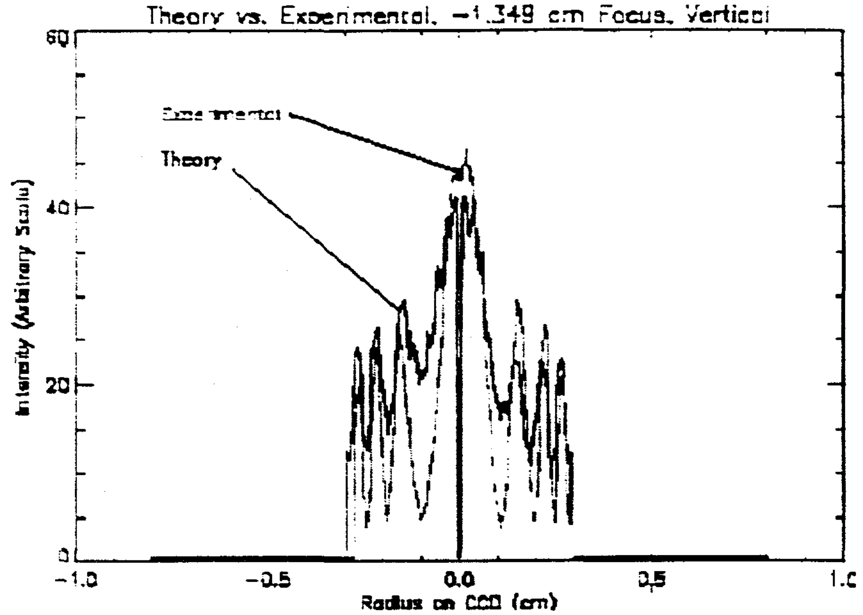

Figure 6: This is a graph of the experimental data plotted over the theoretical predictions. The two match up almost perfectly in terms of fringe positions, though the contrast on the theoretical graph is noticeably lower

4. Comparing Theoretical Predictions with Experimental Results

In order to correctly compare experiments with theory, it was necessary to acquire the parameters for the experiment. These included the focal length of the lens, the distance from the LCPDI to the camera, and the focal distance (the distance from focus to the LCPDI). These were then plugged into the program. The OD (absorption constant) of the dye was found by measuring it at different voltages and then interpolating to find it for the particular voltage used. However, since the OD only affects the contrast of the image, not the position of the fringes, it was not necessary to find the exact value for this.

It was crucial to find the correct index of refraction of the liquid crystal solution, since the shape of the fringe pattern depends heavily on this value. Before the work reported here, there were no measurements of how the index of refraction changed with voltage and accordingly no way to tell what index should be used. This problem was solved by graphing the data using several different values (between 1.6 and 1.7, incremented by tenths) and using the value for which the graph most closely matched the lineouts. In Fig.6, a value of 1.65 was used for the index of refraction.

4.1 Changing the Focal Distance

The first comparisons were done keeping all parameters constant except for the focal distance. Images were captured at nine different focal distances ranging from best focus (0 cm) to a maximum of 1.664 cm. The theoretical data was plotted at each of these distances, and then the experimental data was plotted over it. Some of the results are shown below, as well as in Figure 6.

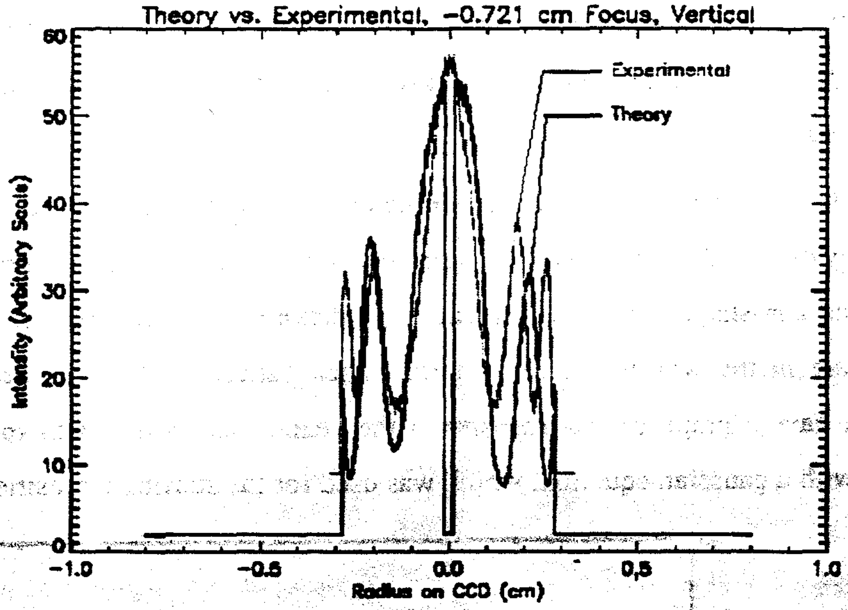

Figure 7: A graph comparing experimental data with the theoretical predictions at a focal distance of −0.721 cm.

As can be seen, the two sets of data do match up rather well. While there are discrepancies in the relative intensities of the two, the horizontal positions of the fringes are the same within a reasonable margin of error. The vertical error can be attributed to the difference in the intensities of the theoretical and experimental beams.

These comparisons were the first that realistically showed that experimental and theoretical data could be compared. They went even further to show that theorists could, in fact, predict what would happen in experiments, paving the way for further studies.

4.2 Spatial Intensity Profile

Though the early results showed that the program did map the horizontal positions of the fringes quite well, it did not account for a few other discrepancies between the theoretical model and the experimental results. One of these is the issue of contrast. The early theoretical predictions had a contrast that was noticeably lower than what was seen in experiments. The probable reason for this is that portions of the object beam may be diffracting around the microsphere and into the center of the beam, where only the reference beam should exist. This would add to the intensity of the reference beam, which would in turn increase the contrast seen in the experimental results. To correct this problem in the theoretical model, it was necessary to artificially increase the intensity of the reference beam by a factor of between one thousand and ten thousand. This increased the contrast of the theoretical predictions to the level of the experimental results.

A second problem was that earlier versions of the program did not account for differences in intensity of the incoming wave. An intensity of one was used for each ray, but the actual beam had a gaussian-shaped intensity profile. A picture was taken of the laser beam with no microsphere in the way to create an interference pattern. When a lineout was taken of this picture, it gave a graph of the intensity of the beam. This graph was then fitted as closely as possible with a gaussian equation, which was used for the starting intensities.

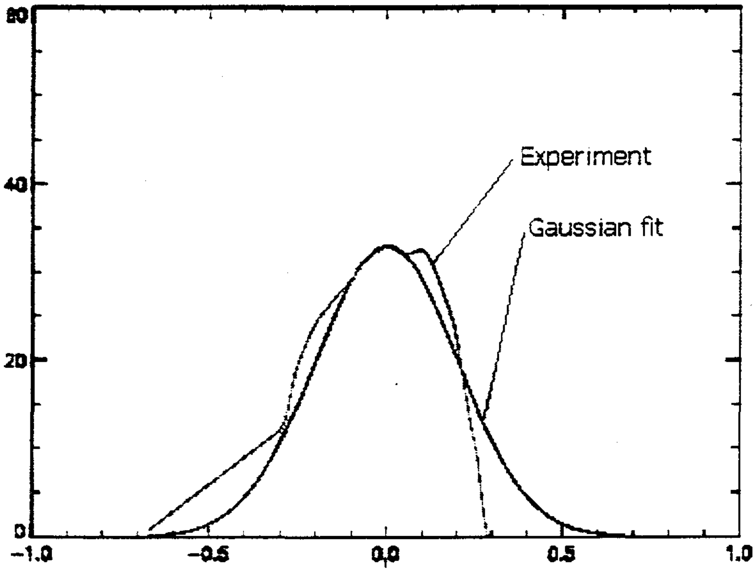

Figure 8: The intensity from the experimental lineout is shown, as well as the gaussian fit. The gaussian curve was used to assign the starting intensities of the rays.

5. Mapping the Change in Index of Refraction

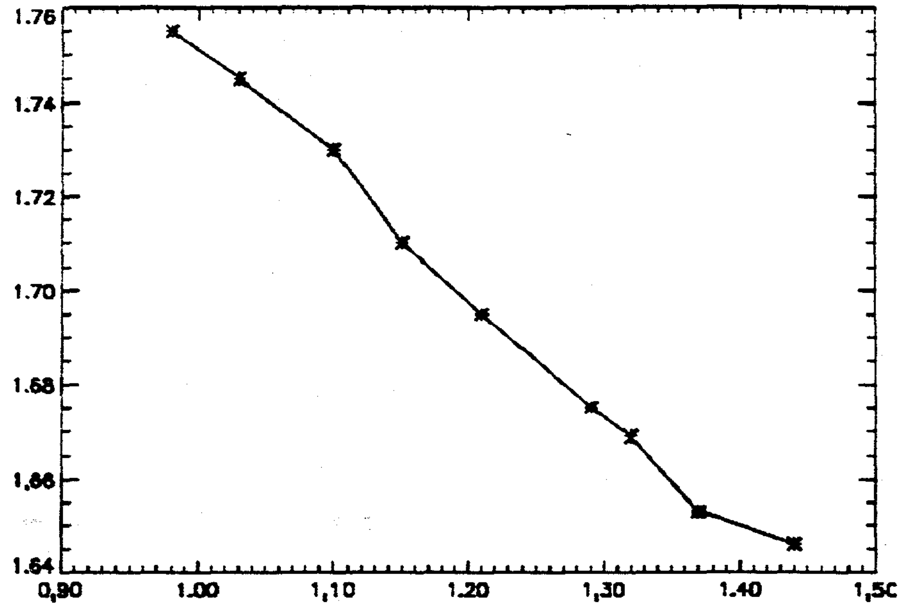

Figure 9: The change in refractive index of the liquid crystals with voltage is graphed here.

The next step that was taken was to determine the index of refraction at different voltages. As voltage is applied to the interferometer, both the OD and the index of refraction change. The change in OD was determined earlier by experimentally measuring it at different voltages. However, the change in index of refraction is difficult to determine in the lab. Therefore, it was mapped theoretically. Data was acquired at a number of voltages between 1V and 1.5V. The index of refraction for each of these voltages was determined in the same way that it was earlier. Graphs were made at a number of different values for n, and the closest one was chosen. The results are graphed in figure 9.

This graph is a compilation of nine separate comparisons under different experimental conditions. When graphed, the data forms a curve with an acceptable amount of error. At this time, this relationship has not been characterized experimentally at the University of Rochester Laboratory for Laser Energetics (aside from figure 9). Studies have been done elsewhere with similar liquid crystals and the results have been comparable[5]. In the future, the change in index of refraction as voltage changes can be determined using more conventional means and the results can be compared with the ones given here.

6. Conclusions

LCPDI modeling has shown that theoretical models can accurately predict experimental results. This has been observed at a variety of experimental conditions. The LCPDI has proved itself to be a promising interferometer and the theoretical model will continue to guide its further development.

7. References

1. Battaglia, D.J. "Analyzing Aberrations in a Laser System Using a Liquid Crystal Point Diffraction Interferometer." *UR/LLE Student Research Reports*. 1997.

2. Jain, Nieraj. "Analyzing Algorithms for Nonlinear and Spatially Nonuniform Phase Shifts In the Liquid Crystal Point Diffraction Interferometer." *UR/LLE Student Research Reports*, 1998.

3. Ning, Lutao. "Characterization of the Liquid Crystal Point-Diffraction Interferometer." *UR/LLE Student Research Reports*, 1999.

4. Turner, Amy. "Ray Tracing Through the Liquid Crystal Point Diffraction Interferometer." *UR/LLE Student Research Reports*, 1998.

5. Turalski, W. and A. Miniewiz. "Calculations of Electric Field Dependence of Effective Refractive Index in Nematic Liquid Crystal Panel." *Mol. Cryst. Liq. Cryst.*, Vol. 325.

8. Acknowledgements

I would first and foremost like to thank Dr. R. S. Craxton, both as my advisor and as the head of the summer high school research program. He spent countless hours explaining what an LCPDI was and poring over pages of code with me to find the one place where I had gone wrong. I would also like to thank Mark Guardalben and Lutao Ning for working with me and providing the experimental data that was crucial to my project. Another thanks goes to Devon Battaglia and John Larkin for helping with any computer-related questions that I had, as well as Ryan Brecker for answering questions I had about the LCPDI. A special thanks goes out to all the summer research students, especially the IAL community, for making this summer a memorable one.

Integrating Hard X-ray Diagnostics into OMEGA Operations

Connecting the Fiducial to the Hard X-ray Detector

Alice Tran

Spencerport High School

Advisor: Christian Stoeckl

Laboratory for Laser Energetics

University of Rochester

Summer High School Academic Research Program

1999

Abstract

The purpose of the project was to connect the fiducial to the hard x-ray detector. In the past the electrical signal was used to measure the relative timing of the the hard x-ray signals. By connecting the fiducial to the hard x-ray detector. the fiducial is used to measure the absolute timing of the hard x-ray signals.

1. Introduction

Today the world depends on sources of energy that not only are depleting the natural resources. but are also polluting the earth. It is clear that we will soon need a new, cleaner, and more efficient means of energy. Therefore, research is being performed on different energy sources which would be either renewable or unlimited. A promising source of energy is fusion.

The scientists at the Laboratory for Laser Energetics at the University of Rochester are currently developing laser fusion. The Laboratory for Laser Energetics (LLE) owns the most powerful ultraviolet (UV) laser in the world. The laser, called OMEGA, has helped fusion research advance. OMEGA is used to create a high temperature, high pressure environment needed for nuclear fusion. The system is about the size of a football field. It takes an infrared laser pulse, splits it into sixty beams, amplifies the individual beams, and then converts them into UV light. Experiments at LLE are pursuing the path of Inertial Confinement Fusion (ICF). ICF at LLE is performed by compressing a small spherical fuel pellet of one millimeter diameter using the OMEGA Laser. The pellet has an outer shell comprised of either glass or plastic, and is filled with a gaseous mixture of hydrogen isotopes, deuterium and tritium. In a technique called direct drive, the sixty UV beams are focused symmetrically onto the small fuel pellet. The energy of the laser beams cause the outer layer to become a plasma and ablate away from the pellet at speeds of 1000 km/s. The ablating plasma acts like a rocket. Obeying Newton's third law, the remainder of the shell implodes at a similar speed toward the center. As a result, the fuel is heated, so that the free nuclei come close enough to fuse. This fusion produces alpha particles (helium nuclei) and energetic neutrons. The goal is to eventually output more energy than the input energy necessary for fusion.

During the implosion, radiation is emitted in a large energy range, including hard x-rays. Hard x-rays are produced when the laser heats the plasma electrons strongly. Understanding the hard x-rays is important, because fast electrons preheat the target, preventing an efficient compression. Since the hard x-rays are proportional to the fast electrons, knowing the amount of hard x-rays, allows the scientists at LLE to determine the amount of fast electrons.

Hard x-rays are measured by the hard x-ray detector. A problem that arose with the hard x-ray detector, was that the electrical trigger was inadequate for timing the fast hard x-ray detector. Since the fiducial can be used to time the hard x-ray detector to less than 50 pico second (ps), the fiducial would be sufficient for measuring the absolute timing of the hard x-ray signals.

2. The Hard X-ray Detector

The hard x-ray detector has a simple design (figure 1). First, the hard x-rays are filtered to a specific energy range. The hard x-rays then enter the scintillator, which transfers them into visible light. The microchannelplate-photomultiplier then converts the visible light into an electrical signal, and amplifies it.

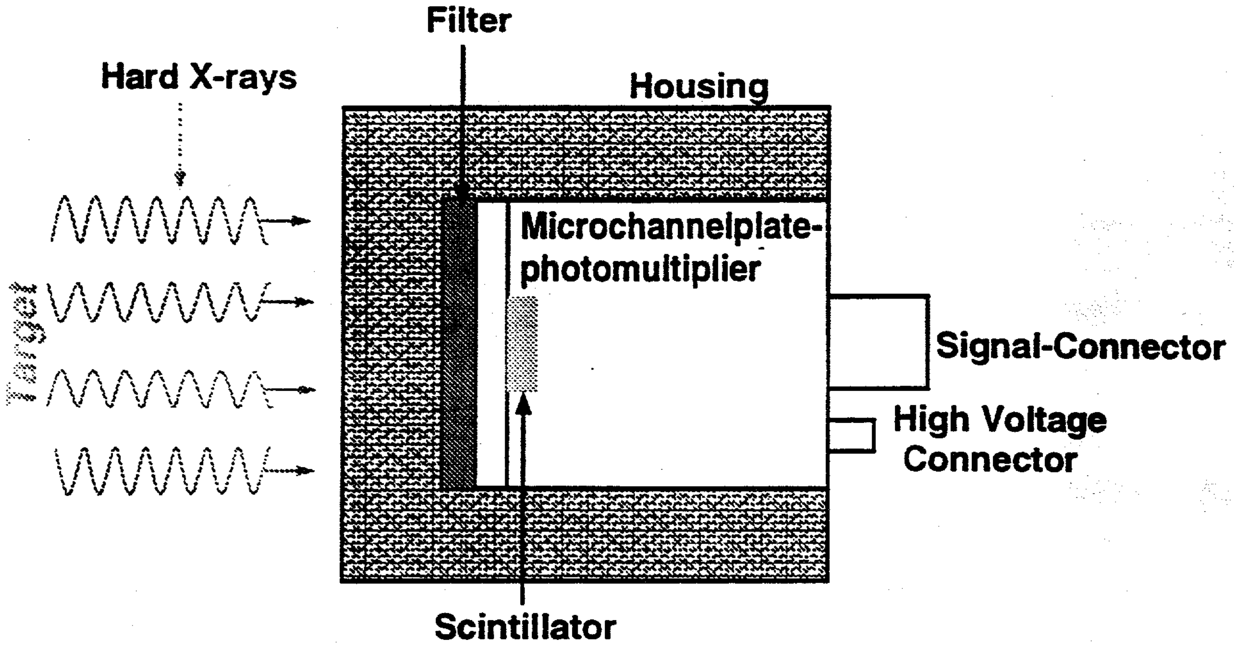

figure 1

Hard X-ray Detector: Radiation emitted from the target enters the hard x-ray detector. The radiation is first filtered, turned into visible light by the scintillator, and changed into electrical signals by the microchannelplate-photomultiplier.

3. Fiducial

The fiducial pulse was used to measured the absolute timing of the hard x-ray detector. Because the electrical trigger was insufficient for the fast hard x-ray detector, the fast and more reliable fiducial needed to be connected to the hard x-ray detector. The formation of the fiducial is quite simple (figure 2). A pulse first originates at the laser oscillator. The pulse is then directed toward the lithium niobate modulator. The lithium niobate modulator is at the same time being electrically fed by a sine wave generator. This produces the fiducial pulse train which is later amplified. The fiducial pulse normally has an eight hump sine wave type pulse, however the oscilloscope used to detect the fiducial was not fast enough to detect all eight humps. Thus the oscilloscope displayed a more square like pulse (figure 3).

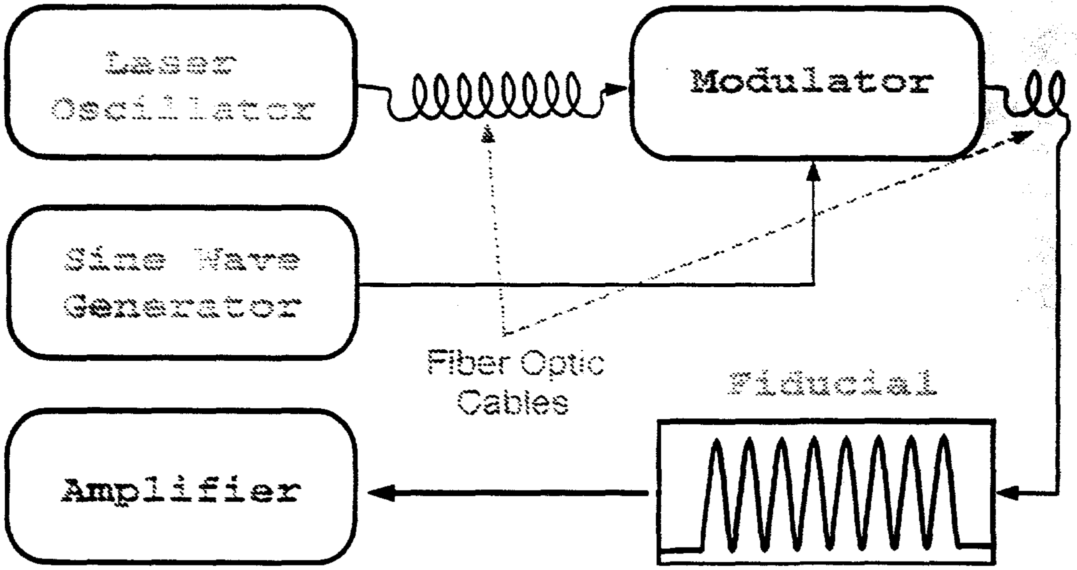

figure 2

Diagram of how the fiducial is formed

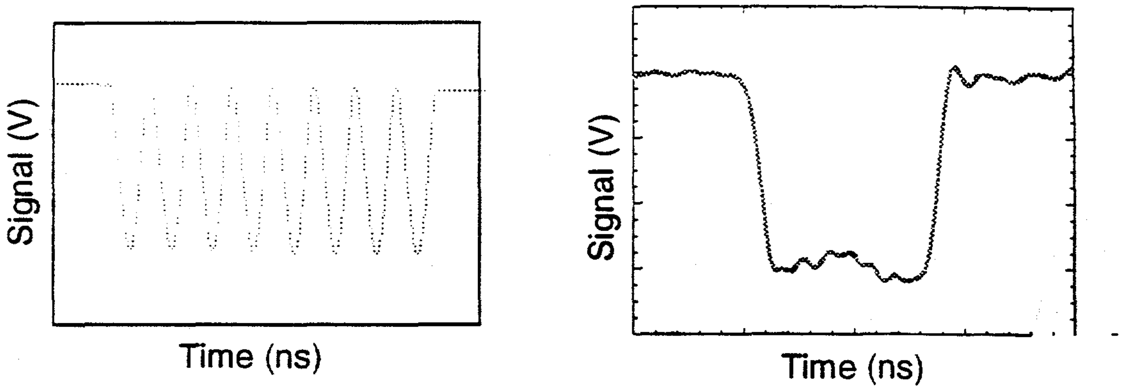

figure 3

Comparison of actual fiducial graph to the fiducial graph obtained by oscilloscope

3.1 Fitted Fiducial Curve

Analysis of the fiducial is important, in not only understanding the fiducial, but also the stability of the fiducial. By understanding the fiducial, measurement errors can be accounted for. For analyzing the fiducial, several programs were written in PV-Wave. One of these programs was used to fit a fiducial curve to a fiducial pulse. The program was proven to be very accurate, because the falling edge of the fitted fiducial curve, was close to the falling edge of the actual fiducial pulse (figure 4). The reference point of the fiducial was defined to be the falling edge's 50% point. The fiducial is measured by an oscilloscope that had a sampling rate of 5 GHz, measuring in 200 ps intervals. Since the oscilloscope was not fast enough, data points on the falling edge were spread apart. The spread out data points would cause an inaccurate account of the reference point. Instead of obtaining the reference point at exactly the 50 % point (figure 4), the inaccurately obtained reference point would be the point nearest to the

50% point. If several data sets were analyzed with this method, there would be low precision. However with the fitted fiducial curve, the reference point can be found more accurately. Instead of choosing the nearest 50% point, the fitted curve can be used to find the relative 50% point. The point would not be exact, since the fitted fiducial curve is not an absolute match to the fiducial pulse, but the accuracy of the reference point using the fitted fiducial curve is within 100 ps. Not only can the fitted fiducial curve be used for the reference point with high accuracy, but if several data sets are analyzed, the reference points obtained with the fitted fiducial curve would also be extremely precise.

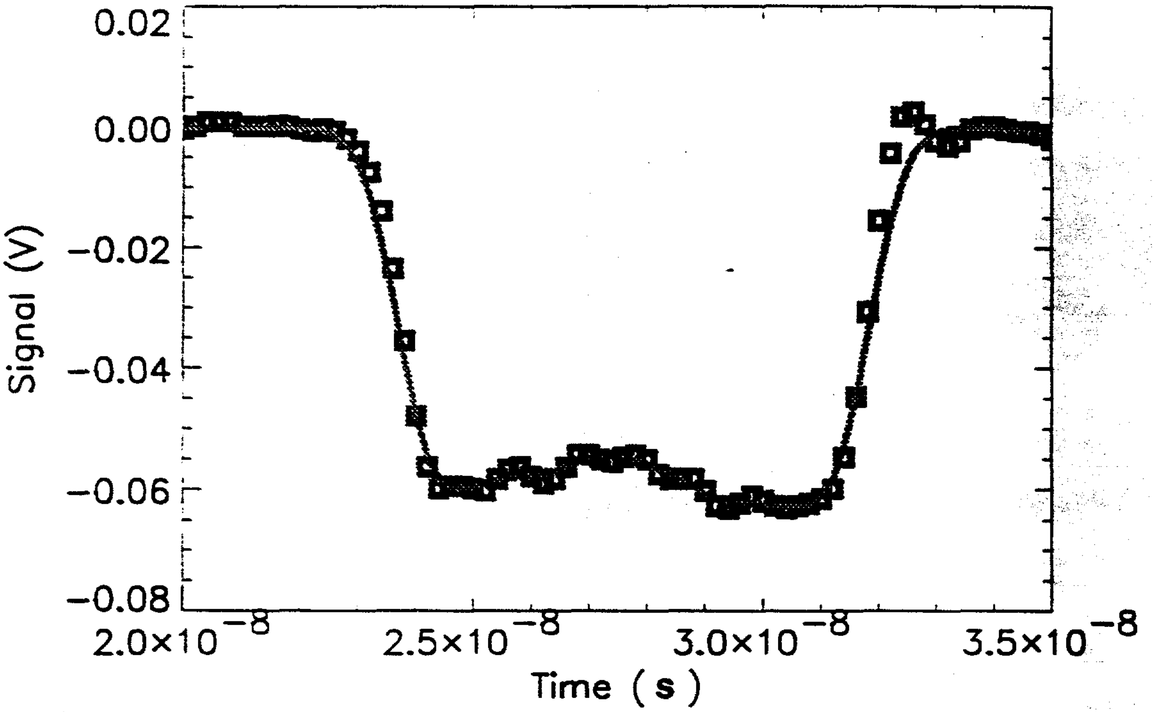

figure 4

Fitted fiducial curve is necessary to determine the falling edge of the fiducial pulse with high accuracy

3.2 Jitter of the System

Another program written in PV-Wave was used to determine the jitter of the system. Understanding the jitter is an important part of measurement. The jitter of a system is defined as the movement of a pulse (figure 5).

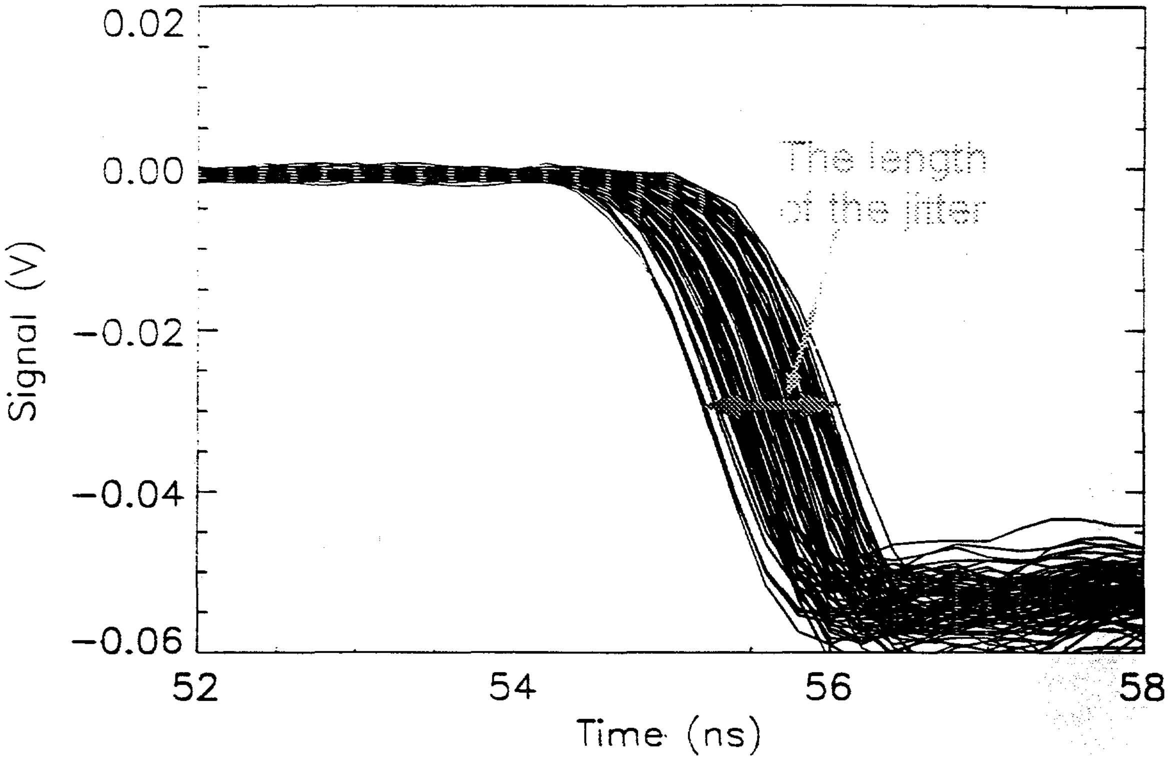

figure 5

***This** graph is an over plot of the falling edge of several fiducial pulses.*

***The** jitter of the system is relative to the electrical trigger.*

The jitter of the system was actually very large (figure 6). The program found that the jitter of the system was approximately two nano seconds (ns) long. Since the jitter was so large, the program showed that an electrical jitter was insufficient for the fast hard x-ray detector. Instead, it proved that the fiducial is even more adequate, since the fiducial had only a 50 ps jitter.

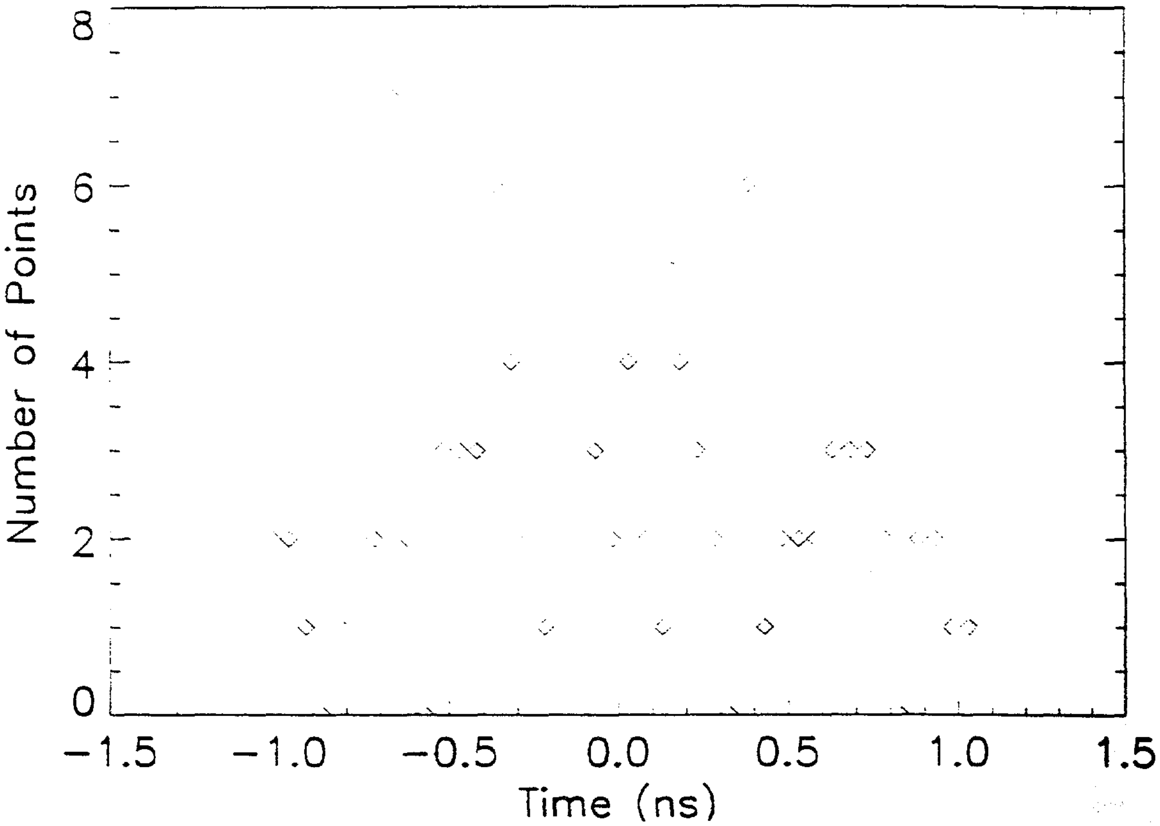

figure 6

The jitter of the system can be seen through a histogram. Zero is the average of several fiducial pulses, thus the histogram is relative to the average of the fiducial pulses. This histogram shows the high jitter of the system relative to the electrical trigger.

4. The Process of Connecting the Fiducial to the Hard X-ray Detector

Connecting the fiducial to the hard x-ray detector was necessary, because the fiducial was capable of measuring the absolute time of the hard x-ray signal. Without the fiducial as a time reference, the hard x-ray detector would have a signal with a relative time base only.

Connecting the fiducial involved several intermediate steps (figure 7). The laser oscillator is a pulse generator, that periodically outputs a pulse. The pulse from the oscillator is split equally into two. The first pulse is shaped, then split and amplified several times, until 60 equally uniform beams are formed. These sixty beams are focused onto the target, to induce fusion. During this process, hard x-rays are emitted from the target. These hard x-rays are collected by the hard x-ray detector. The second pulse is shaped into the fiducial pulse, which was connected to the photo diode to be converted from light to an electrical signal. The fiducial then converged with the hard x-ray signal in the splitter, where they were to be recorded on the oscilloscope.

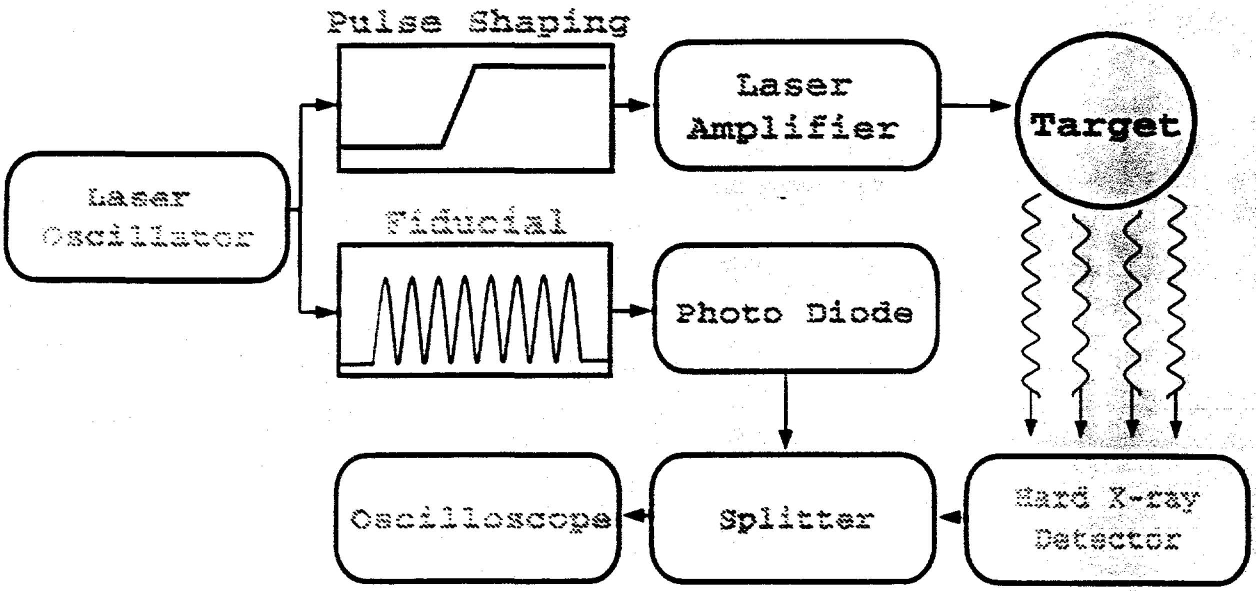

figure 7

A simplified diagram of the process of connecting the fiducial to the hard x-ray detector.

4.1 Photo Diode

The fiducial is converted from light signals to electrical signals through the photo diode. The photo diode used to connect the fiducial to the hard x-ray detector was an established design used at LLE (figure 8). Since the hard x-rays signals were negative, it was necessary to reverse the polarity of the photo diode. By reversing the polarity, the fiducial and the hard x-ray signals can be compared with optimum resolution using the oscilloscope (figure 9).

The fiducial light signal firsts travel through a fiber optics cable toward the fiducial connector (figure 8). The light enters the photo diode container, and travels through the small coil of fiber optics. The fiber optics cable directs the fiducial light signals toward the photo diode (figure 8). The photo diode is powered by several standard watch batteries. The fiducial electrical signal then exits the photo diode through the output connector.

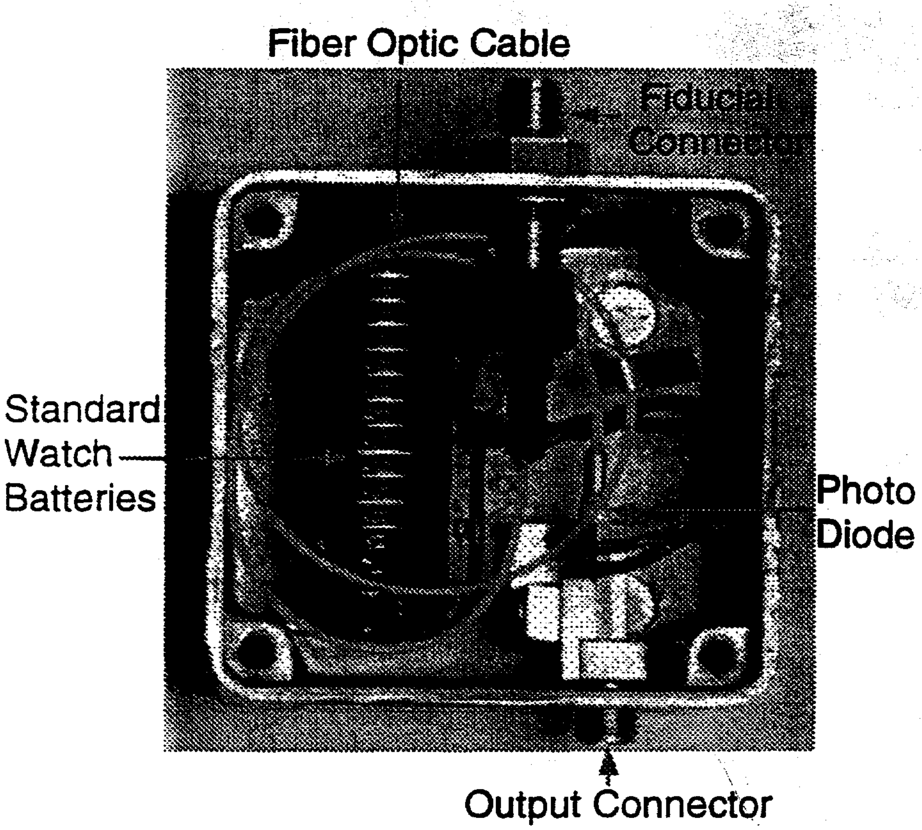

figure 8

The photo diode is necessary for converting the fiducial light signals to electrical signals. The fiducial enters the photo diode container, through the fiber optic cable, toward the photo diode. The batteries lined in a row on the left, power the photo diode.

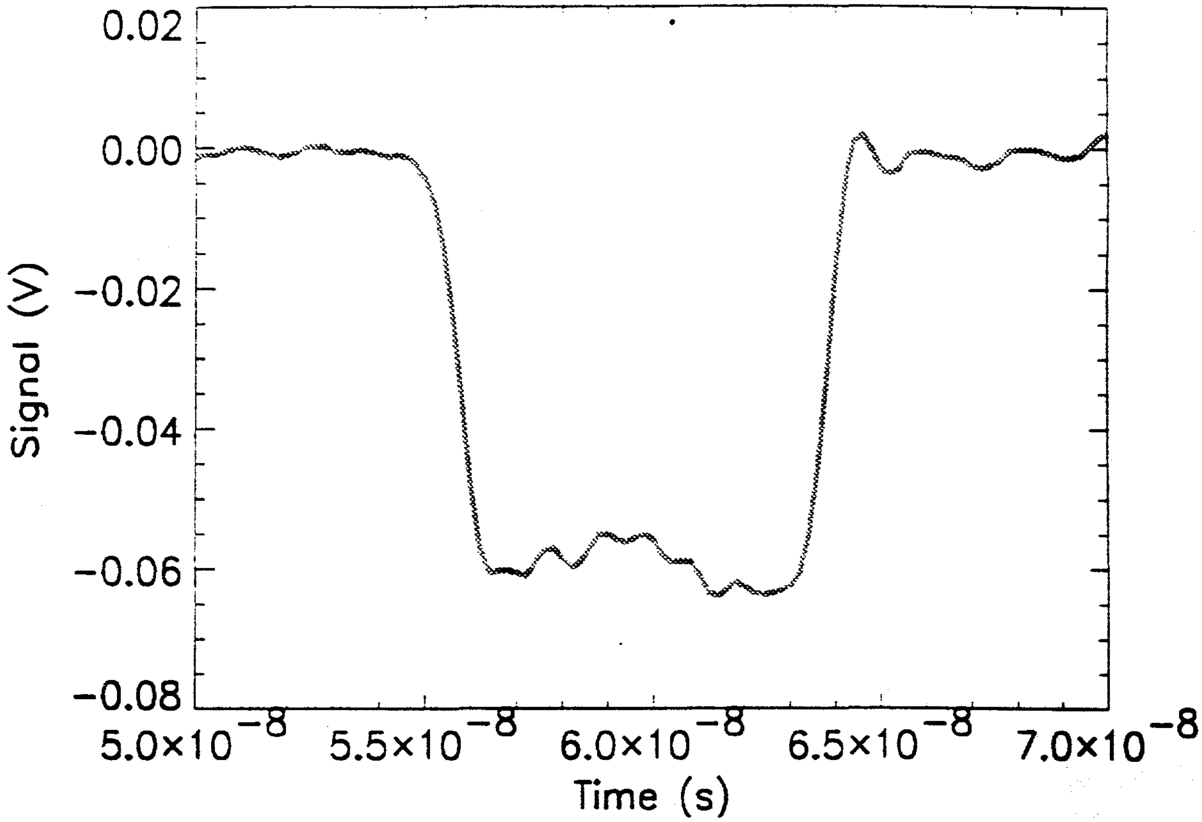

figure 9

The fiducial pulse as seen on the photo diode.

4.2 Splitter

The splitter is essential to connecting the fiducial to the hard x-ray detector. The purpose for the splitter is to converge the fiducial pulse, and the hard x-ray signals onto the oscilloscope that then can be compared (figure 10). The splitter is especially effective because the splitter system consisted of resistor and cables, which had negligible jitter.

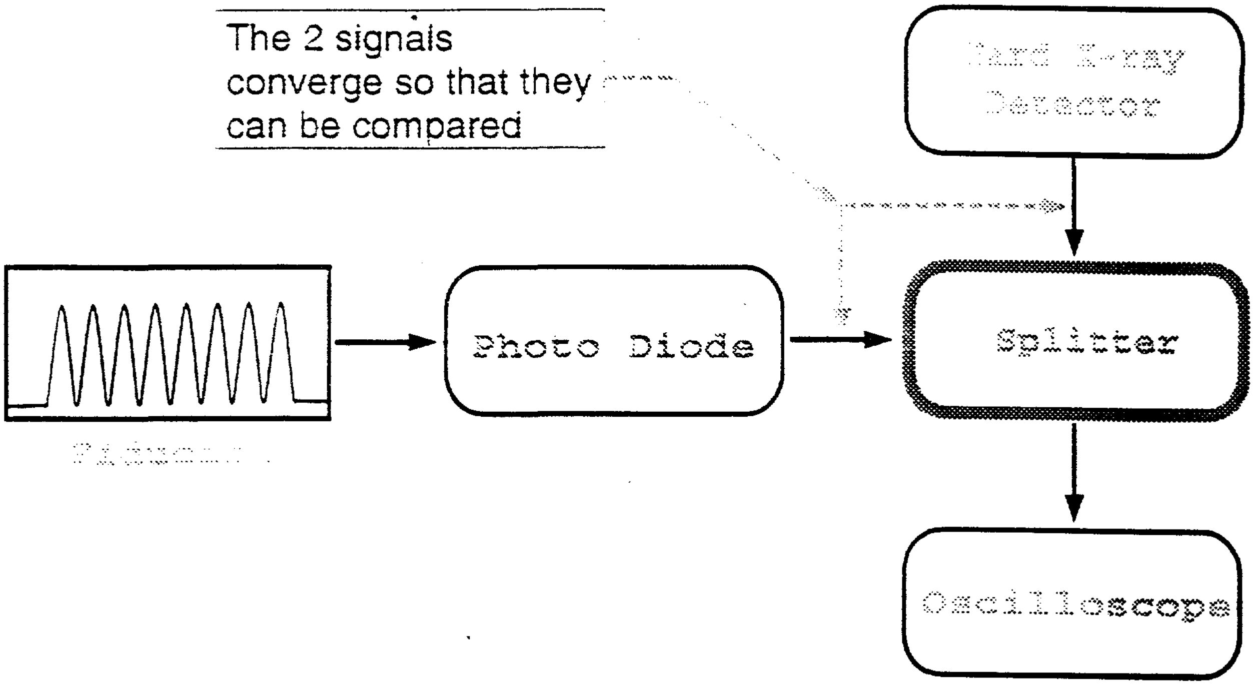

figure 10

A diagram of the splitter's purpose

The splitter has a very simple yet effective design (figure 11). The splitter consisted of three resistors, all equal in resistance of about 50 ohms. The symmetrical design of the three resistors allows for more flexibility, and allows for a pulse to split equally, to converge uniformly.

figure 12

design of the splitter

and its three resistors.

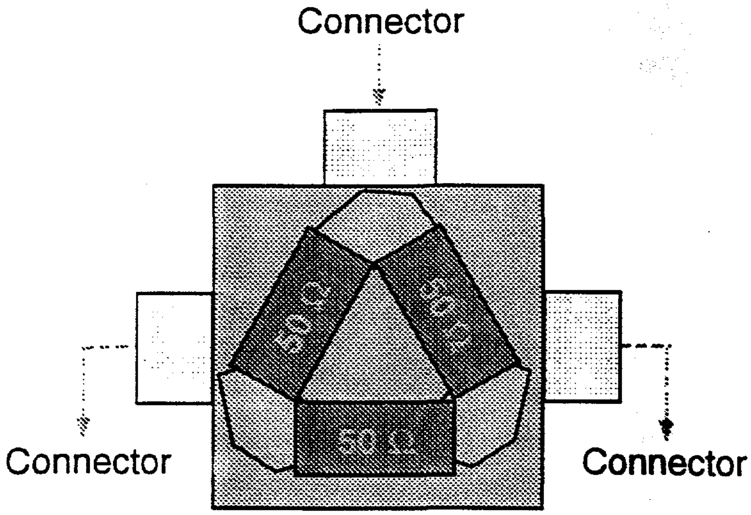

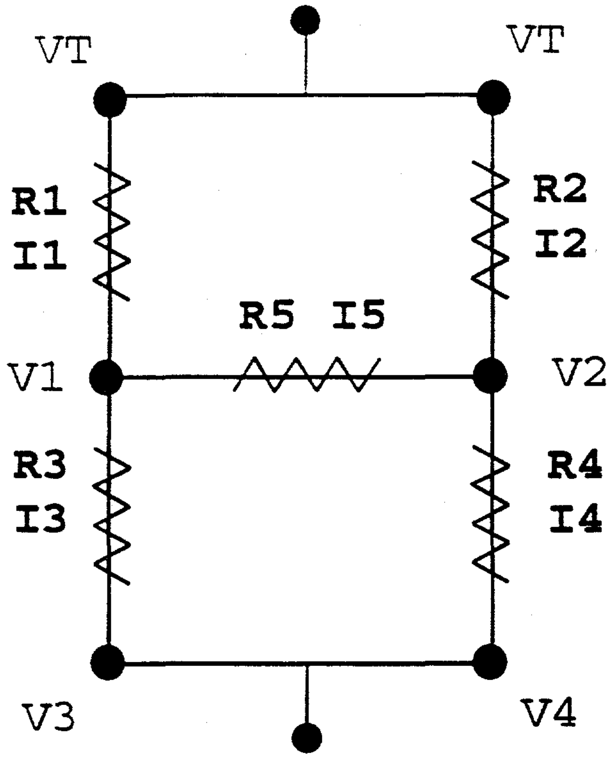

Ra = R1 = R2 = R5
Rb = R3 = R4 = 50

I2 + I4 + I5 = 0
I1+ I3 + - I5 =0

VT - V1 = I1•R1
VT - V2 = I2•R2
V3 - V1 = I2•R3
V4 - V2 = I4•R4
V1 - V2 = I5•R5

$$\frac{VT-V1}{Ra} = I1$$

$$\frac{VT-V2}{Ra} = I2$$

$$\frac{V3-V1}{Rb} = I3$$

$$\frac{V4-V2}{Rb} = I4$$

$$\frac{V1-V2}{Ra} = I5$$

$$I2 + I4 + I5 = I1 + I3 - I5$$

$$\frac{(VT-V2)}{Ra} + \frac{(V4-V2)}{Rb} + \frac{(V1-V2)}{Ra} = \frac{(VT-V1)}{Ra} + \frac{(V3-V1)}{Rb} - \frac{(V1-V2)}{Ra}$$

$$\frac{-3(V2-V1)}{Ra} = \frac{Ra(V2-V1)}{Rb}$$

$$-3Rb(V2-V1) = Ra(V2-V1)$$

$$-3RbV2+3RbV1 = RaV2 - RaV1$$

$$-3RbV2 - RaV2 = -3RbV1 - RaV1$$

$$V2(-3Rb-Ra) = V1(-3\ Rb-Ra)$$

$$V2 = V1$$

figure 13

Resistor design of the splitter with the proof of the flexibility

5. Results

The fiducial was successfully connected to the hard x-ray detector. At first reflections occurred (figure 14), but the reflections were easily eliminated with an attenuator. Although the attenuator diminished the fiducial pulse, the over all connection was successful. The fiducial is now used as a reference for the hard x-ray detector that measures the absolute time of the hard x-ray signal (figure 15).

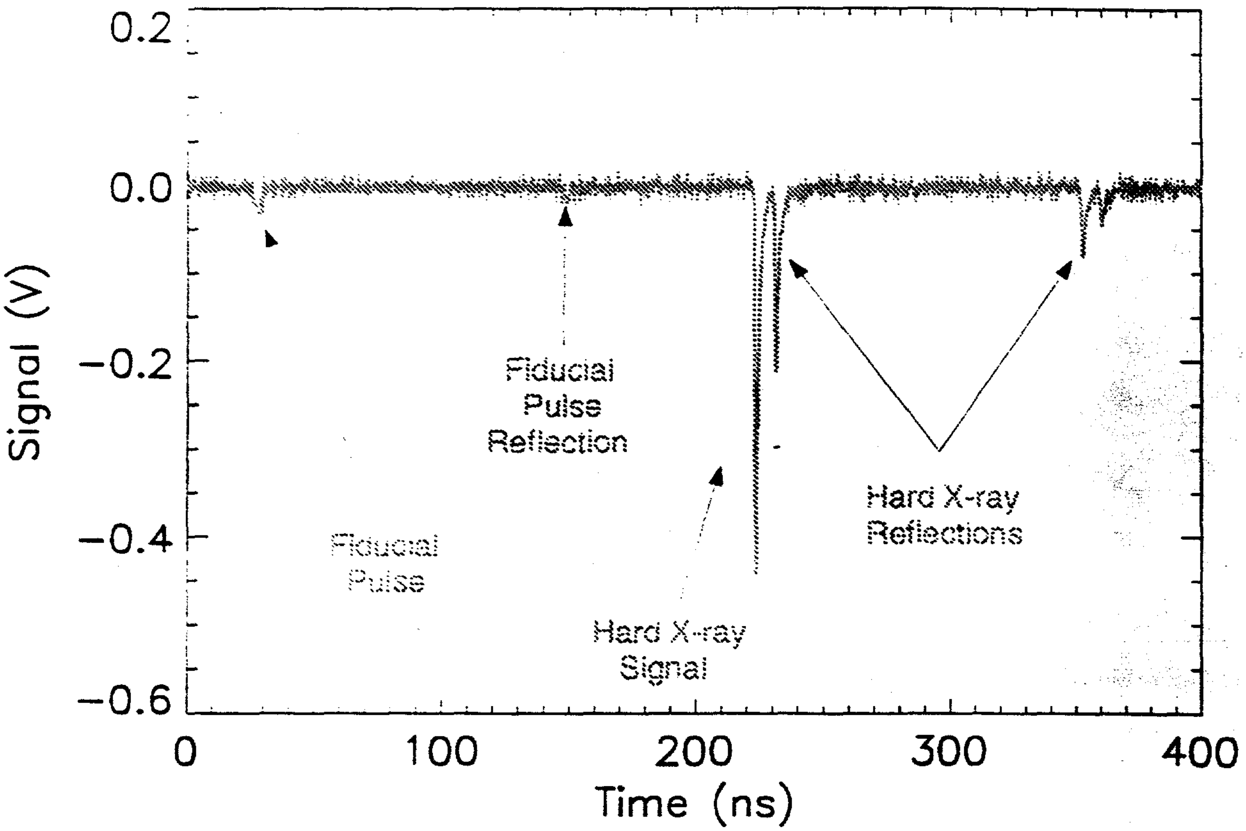

figure 14

The fiducial pulse and the hard x-ray signals with reflections

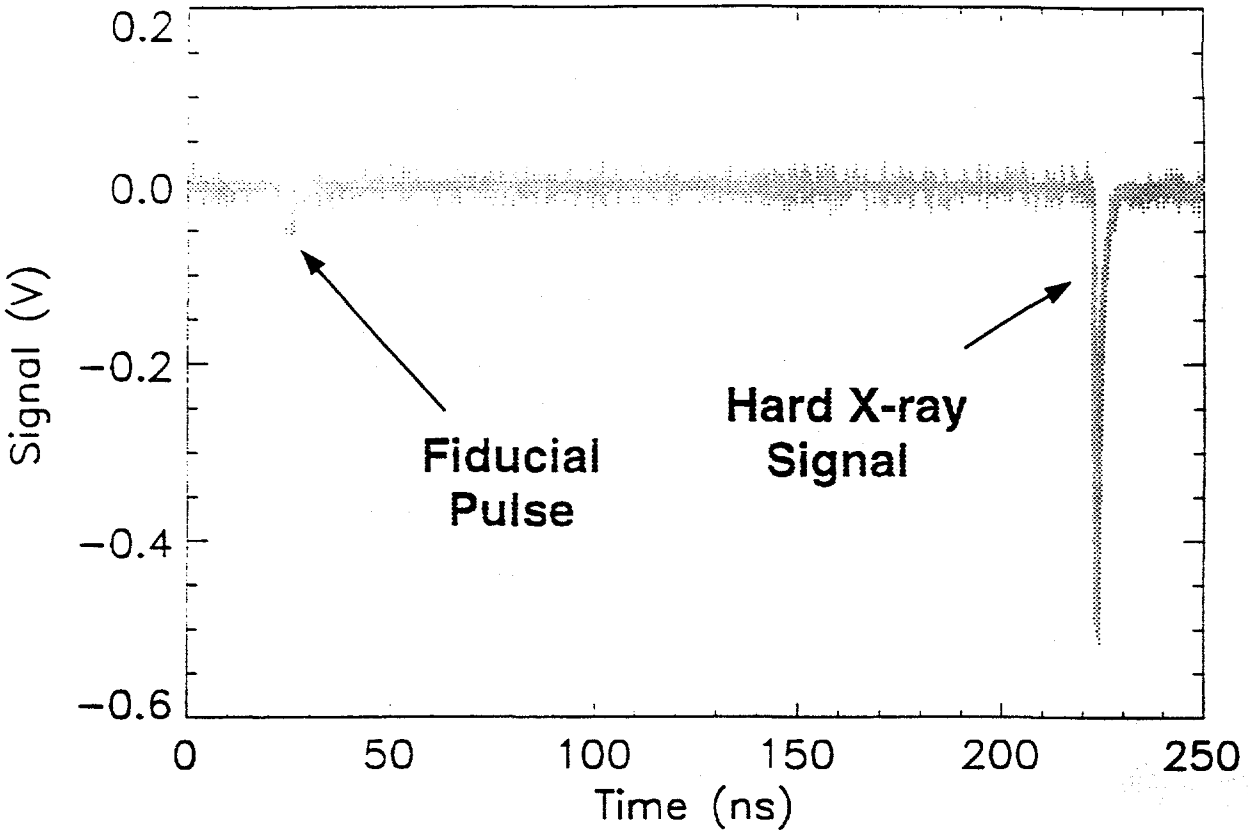

figure 15

the fiducial pulse and the hard x-ray signal

6. Conclusion

Although the fiducial was successfully connected to the hard x-ray detector, some improvements can be made. The best results would be if the fiducial pulse and the hard x-ray signals had similar magnitude. By having similar magnitudes, the fiducial pulse as a reference time for the hard x-ray signals would be easier to compare. A solution to increase the fiducial's magnitude would be to increase the energy of the fiducial pulse.

Acknowledgments

I would like to thank Christian Stoeckl for all of the time he has spent with me, and giving me the guidance I needed. I would also like to thank Dr. R.S. Craxton for running the High School Program, and for allowing me the chance to work here at LLE. I wish to express my gratitude for John Larkin, who spent his precious hours answering my questions, and teaching concepts. I would also like to thank Devon Battaglia, Lutao Ning, and Rohit Rao for their essential help with programming, and with the problems from the Suns. I want to say thanks to Tony Brancato for all of his help when the computer froze, or when it just didn't work. I want to thank Jyoti Kandlikar and Peter Hopkins for their advice and opinions. Especially Peter who made me laugh with his great impressions. Finally, I want to thank for all of the other students for all of the great times we had.

Predicting the Optical and Dielectric Anisotropy of Liquid Crystalline Systems

Jordan VanLare

Project Advisor: Kenneth Marshall

Laboratory for Laser Energetics
University of Rochester

1999 Summer High School Research Program

Abstract:

Advances in quantum chemistry and computer technology have led to the development of software that is capable of accurately predicting the structure, chemical, and physical properties of molecules. This process, termed molecular modeling, can be used to calculate the optical and dielectric anisotropy in liquid crystalline systems. Using data from a molecular modeling package and formulas by Vuks. Lorentz. Lorenz. Onsager. Maier and Meier, the optical and dielectric anisotropy of both mesogenic and oligomeric liquid crystalline systems was predicted. Trends were noted for mesogens having a high dielectric anisotropy and those with the greatest values were coupled with polyacrylate backbones. The optical and dielectric anisotropy was then calculated for the latter oligomeric systems.

1. Introduction

A liquid crystal (LC) is in an intermediate mesophase between a solid crystalline lattice structure and an isotropic or liquid phase. The LC phase is characterized by a degree of intermolecular orientation, as in a crystal, while exhibiting the fluid properties of a liquid. A liquid crystalline phase can be induced by increasing either the solvent concentration (for *lyotropic* LC's) or the temperature (for *thermotropic* LC's), as shown in Fig. 1. Three main mesophases can be found in calamitic (cigar-, or rod-shaped) LC's, distinguished by varying degrees of order. The smectic phase, which has the highest degree of order, has parallel layers with both directional and orientational order. The cholesteric phase is characterized by layers of LC's with directional order. Each subsequent layer's director is rotated slightly so that the directional vectors of multiple layers form a helix. The LC phase with the least amount of order, the nematic phase, has only directional order, with the molecules analogous to logs floating down a river. The optical and dielectric properties of LC's are largely a result of their rod-like shape. Because of their asymmetric structure, LC's exhibit both unique refractive indices and dielectric constants parallel and normal to the molecular axis. These multiple values of refractive index and dielectric constant give rise to anisotropy in these state properties depending on the molecular orientation. The dielectric anisotropy, which allows a liquid crystal to reorient in an applied electric field, provides for unique applications. Thus, the use of liquid crystalline systems in precision optical devices and LC displays in televisions and computer monitors is prevalent.[1] Optical applications for LC polymers are also being developed.

Liquid crystals polymers can be either main chain polymers or side chain polymers. Main chain polymers, not investigated in this study, are simply mesogenic units lined head to tail and connected by spacers consisting of several alkyl groups. Side chain polymers are composed of backbones consisting of carbon-carbon, silicon-oxygen, or other repeating segments. Mesogens are attached to the backbone with alkyl spacers (usually three to five carbons) and protrude from the backbone. Polymeric LC's have several advantages over their low molecular weight counterparts. Polymers with a high glass transition point are more thermally stable and environmentally robust than single mesogens and can also form free-standing thin films. A polymer's high viscosity, however, slows electro-optic response time making application for many compounds impractical. Polymeric LC systems having a high dielectric anisotropy ($\Delta\varepsilon$), however, can have sufficiently fast response time for use in some types of electro-optic devices because the larger difference in dielectric constants results in a greater force on the molecule to reorient to an applied electric field.[2]

The measurement of $\Delta\varepsilon$ in polymeric LC systems is both challenging and often inaccurate, as the high viscosity of these systems and the intramolecular orientation of the mesogens makes alignment difficult (Fig. 2). Applying the techniques for calculating the optical anisotropy, or birefringence (Δn), in LC's using molecular modeling proposed by M. Klasen, *et al.*[3] to polymers allows the prediction of the optical and dielectric anisotropy of such systems. Modeling the compounds before synthesis is helpful for several reasons. The synthesis of all the permutations and combinations of a series of compounds is expensive and time consuming. Modeling allows one to target first for synthesis those molecules that exhibit the most ideal predicted properties. As the measurement of $\Delta\varepsilon$ in polymeric LC's is so difficult, synthesizing and measuring the properties of those compounds with a high $\Delta\varepsilon$ first will serve to reduce the number of compounds that must be synthesized.

It must be noted that the values calculated from structures for $\Delta\varepsilon$ and Δn are only predictions to be taken qualitatively, since certain assumptions must be made when optimizing molecular geometry with semiempirical methods. Because these calculations are purely theoretical, the compounds of interest must still be synthesized and measured to obtain and verify precise experimental values.

2. Method

Candidate molecules were constructed graphically using Wavefunction, Inc.'s *Spartan* v.5.1.3, a computational chemistry software package running on a DEC Alpha Server under the UNIX operating system. Merck energy minimization was performed before optimizing the geometry with the semiempirical method and the AM1 parameter set. Geometry was optimized at 0 °K. All values for the polarizability and the dipole moment were calculated at zero point energy.

2.1.1 Calculation of Δε

The dielectric anisotropy is calculated using the Maier – Meier theory, given by[3]

$$\Delta\varepsilon = \frac{NFh}{\varepsilon_0}\left(\Delta\alpha - \frac{F\mu^2}{3k_B T}(1 - 3\cos\beta)\right)$$

where

$$F = \frac{1}{(1 - f\alpha)}$$

$$f = \frac{\varepsilon - 1}{2\pi\varepsilon_0 a^3(2\varepsilon + 1)}$$

$$h = \frac{3\varepsilon}{2\varepsilon + 1}$$

and ε_0 is the permittivity of a vacuum. k_B is Boltzmann's constant. N is the molecular density, T is the absolute temperature. S is the order parameter of LC compounds. β is the angle made between the director and the dipole moment. $\Delta\alpha$ is the anisotropy of polarizability, a is the radius of the spherical cavity surrounding the molecule, and μ is the magnitude of the dipole moment. The values for N, T, and S were taken to be 1000 kg/m^3, 293 ^{o}K, and 0.7 respectively. The static permittivity, ε, is derived algebraically from the Onsager theorem[3].

$$\varepsilon - 1 = \frac{NFh}{\varepsilon_0}\left(\alpha + \frac{F\mu^2}{3k_B T}\right)$$

where α is the mean polarizability.

2.1.2 Calculation of Δn

The birefringence, $\Delta n = n_e - n_o$, was calculated with values from the Vuks equations[3]

$$\frac{n_e^2 - 1}{n^2 + 2} = \frac{N}{3\varepsilon_0}\left(\alpha + \frac{2\Delta\alpha S}{3}\right)$$
$$\frac{n_o^2 - 1}{n^2 + 2} = \frac{N}{3\varepsilon_0}\left(\alpha - \frac{\Delta\alpha S}{3}\right)$$

while the Lorentz – Lorenz equation

$$\alpha = \frac{3\varepsilon_0(\varepsilon - 1)}{N(2\varepsilon + 1)}$$

gives values for ε at optical frequencies, where $\varepsilon = n^2$ as above.[4]

2.2 Reproduction of Data

The data published by M. Klasen *et al*[3] was reproduced to verify the validity of the structures generated by *Spartan*. The *Spartan* software obtained excellent agreement for both $\Delta\varepsilon$

and Δn (Fig. 3). The modeled structures had a broad range of predicted $\Delta\varepsilon$, from 0.5 to 47.9. The greatest source of error between theoretical (calculated) and experimental (published) values was due to a lack of correlation for β. Much better agreement was obtained between the theoretical and experimental values for the dipole moment magnitude and the polarizability. Better correlation was obtained between theoretical and experimental values for Δn than for $\Delta\varepsilon$, as β is not required in the calculation of the former.

3. Modeling of Low Molar Mass Mesogens

A total of 17 low molar mass mesogens were modeled to determine the molecular characteristics of molecules with high $\Delta\varepsilon$. Data for each mesogen along with its 2D molecular structure can be found in Table 1 and Fig. 4, respectively. The data suggests that as the terminal group grows in length the polarizability decreases, resulting in a lower $\Delta\varepsilon$. Mesogens with a positive $\Delta\varepsilon$ that use an ether linkage to connect the alkyl terminal group to the phenyl ring show a slight increase in polarizability and a 12% increase in the magnitude of the dipole moment as compared to similar structures where the ether linkage is absent. Although the ether linkage also increases the value of β, the effect is not large enough to outweigh the effects of the larger dipole moment and polarizability of the ether linkage, with the result that the ether-containing compounds have a higher $\Delta\varepsilon$ than their alkyl counterparts. If required, this increase in β can be compensated for by placing a second alkyl group between the alkoxy (alkyl-ether) group and the phenyl ring. In general, lengthening the molecule along the director reduces the angle between the molecular axis and the dipole moment. The polarizability is also larger in such molecules, as the electronegativity of the oxygen is strong enough to influence π electrons in unsaturated structures such as the alkynes (C≡ C central linkage groups) in Fig. 4.

Addition of a terminal naphthalene group greatly increases $\Delta\varepsilon$. The large number of delocalized electrons in such fused ring systems, when coupled with highly electronegative terminal groups, shows a very large increase in both the polarizability and the magnitude of the dipole moment when compared to mesogens with otherwise similar features. While an increase in polarizability is noted when a phenanthrene is substituted for a naphthalene terminal group, the mesogen also exhibits a decreased dipole moment magnitude, and an increased molar mass, volume, and β. Further investigation must be done with molecules containing multiple fused ring groups to have a more complete understanding of behavior; however, current data show an increase in $\Delta\varepsilon$ for mesogens with two naphthyl groups compared to those with only one.

Mesogens whose phenyl and naphthalene ring systems are connected by an alkyne group tended to have a lower $\Delta\varepsilon$ than those connected by an ester. The reason for this behavior is that while an alkyne is rich in π electrons, it is a relatively non-polar functional group. The ester contributes to both the polarizability and the dipole moment because of oxygen's high electronegativity. Dielectric anisotropy was highest in molecules whose bridging group contained the ester preceded by an alkyne. The electronegativity of the oxygen is strong enough to attract the alkyne's π electrons, strengthening the molecular dipole moment and increasing the polarizability.

Cyano groups were the most successful terminal groups because of their low mass, high electronegativity, and 180° bond angle between the C and N atoms. The optimal placement for the cyano groups on the rings depended largely on the bridging group used. For compounds with alkoxy and cyano terminal groups, those with an alkyne bridging group had the highest $\Delta\varepsilon$ when the cyano group was at the 3 and 4 carbon positions of the ring, while those molecules with an ester in the bridging group performed better in the 4 and 5 positions. This is a result of a combination of inductive and "resonance" interaction of the ester and cyano groups with the π-electron system of the aromatic phenyl and naphthalene rings.

4. Modeling of Oligomers

Three types of oligomers (very small polymers with only 1-3 repeat units) were modeled: polyacrylates, polysiloxanes, and cyclosiloxanes. Only those compounds with a polyacrylate backbone were successfully modeled with *Spartan*, as the software is not capable of handling larger molecules or polymers. Oligomers with one, two, and three repeat units were modeled successfully. As the number of repeat units increases from 1 to 3, $\Delta\varepsilon$ also increases. The strength of the dipole moment increases as each mesogen is added and β decreases a great deal because of the symmetry in the molecule. Thus, in oligomers $\Delta\varepsilon$ varies directly with the number of repeat units for the samples modeled. Dielectric anisotropy also increases in an oligomer as the $\Delta\varepsilon$ of its mesogenic component increases. The dielectric properties of oligomers are being further investigated with new software. The results of these experiments will be useful in determining which polymers would be best for use in electro-optic devices.

5. Summary

A valuable method for predicting dielectric anisotropy and birefringence in LC compounds was successfully developed and applied to many molecules. The results published by M. Klasen *et al* were reproduced with great accuracy. Experimental mesogens were modeled successfully and several were found to have relatively high theoretical values for $\Delta\varepsilon$. Oligomers with two and three repeat units were also modeled. Because the available software used was not designed for large molecular systems, only oligomers with less than three repeat units could be studied. While the available software used for this experiment only allows limited modeling capabilities in oligomeric systems, molecular modeling packages capable of handling macromolecules could be used to model and determine the optical and dielectric properties of larger LC polymers. The latter topic is the subject of an ongoing investigation.

Acknowledgements

I thank the University of Rochester's Laboratory for Laser Energetics and the Summer High School Research Program for both providing the facilities for conducting these experiments and making participation in this program possible. I also gratefully acknowledge the assistance of the following individuals; Kenneth L. Marshall, my project advisor, for conceiving the project and guiding my efforts; Tanya Kosc for her instruction and guidance throughout the research process; Dr. Melanie Klasen from E. Merck Darmstadt, Germany for valuable discussions and computational support; Anthony Brancato and Steven Corsello for assistance with *Spartan* software and the UNIX system; and Dr. R. Stephen Craxton, the Summer High School Research program director, for helpful discussions and encouragement.

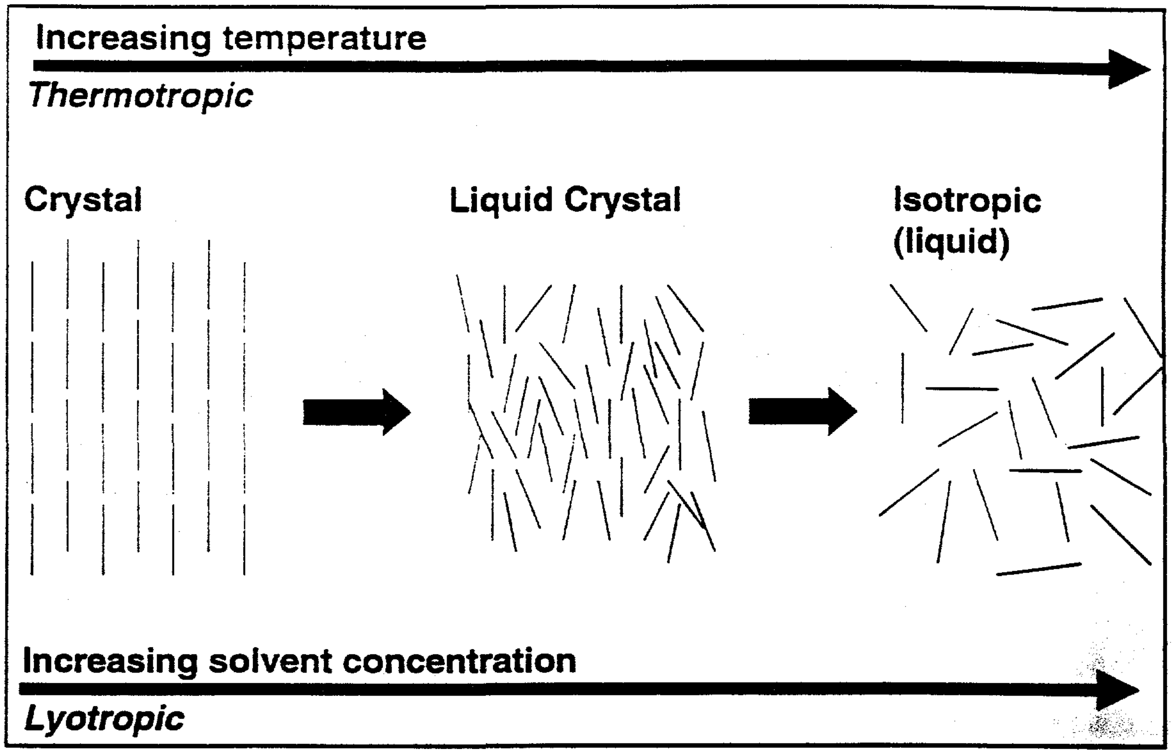

Fig. 1: Increasing the temperature or solvent concentration from a crystalline phase can induce a liquid crystalline phase.

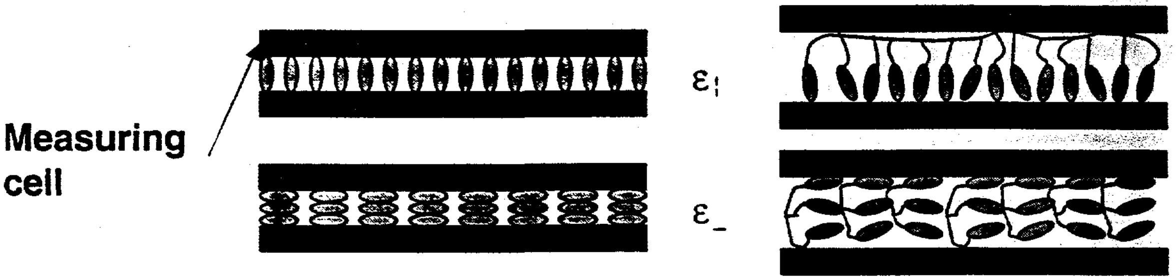

Fig. 2: Single mesogens align in a measuring cell (a capacitor) easily for calculation of the dielectric anisotropy. Alignment of LC polymers in a measuring cell is difficult and measurements can be inaccurate.

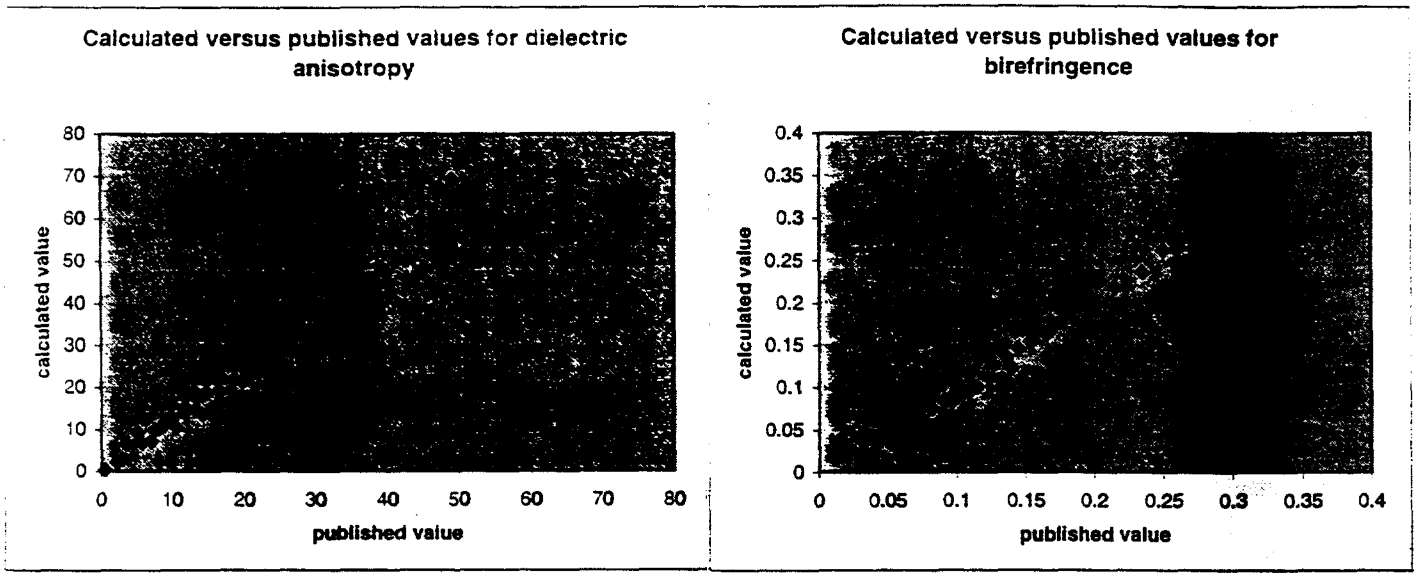

Calculated versus published values for dielectric anisotropy

Calculated versus published values for birefringence

Fig. 3: Excellent agreement was found between published values for dielectric anisotropy and birefringence and those calculated by *Spartan*.

Compound #	α (A.U.'s)	$\Delta\alpha$ (A.U.'s)	β (degrees)	μ (debyes)	Volume	$\Delta\varepsilon$	Δn
1	257.015264	390.4	11.07	4.979064	373.99	42.5161	0.4474
2	265.880082	391.96	11.59	4.982163	394.54	39.3077	0.4305
3	274.420177	392.72	12.55	4.983104	415.12	36.1843	0.4138
4	282.803572	391.2	13.82	4.982144	435.67	33.2488	0.3962
5	230.091726	281.86	21.97	8.203632	387.15	72.9749	0.29
6	263.189245	370.31	17.01	7.101902	386.18	78.6186	0.4136
7	275.915515	407.59	22.26	8.06188	397.63	90.0032	0.4331
8	273.125424	385.7	12.76	6.711236	397.05	71.5679	0.4102
9	244.454183	290.91	23.28	9.804813	404.09	101.9708	0.2934
10	242.076661	269.97	12.11	8.114232	403.37	83.2304	0.2727
11	324.267636	476.71	9.13	6.95273	449.65	74.5489	0.4411
12	291.748378	362.91	15.42	9.101398	456.1	95.7118	0.3204
13	291.843771	332.67	12.3	8.27569	457.02	81.6492	0.2944
14	300.123948	458.27	19.98	6.696209	414.65	67.5593	0.4757
15	308.927978	481.07	10.34	6.84503	426.2	77.5918	0.4768
16	290.193221	377.8	26.51	5.639009	425.76	34.9834	0.3758
17	274.474416	357.23	13.76	9.267324	432.57	107.7394	0.3366
18	277.715177	365.22	12.82	9.404164	432.87	114.0003	0.344
19	311.699133	452.5	13.8	9.903432	462.03	126.2752	0.3999
20	368.296917	552.46	16.64	11.250014	522.4	143.2611	0.4176
21	397.254612	315.01	15.73	6.008164	751.76	20.0647	0.1824
22	571.452172	419.19	20.65	8.586191	1082.61	26.2051	0.1659

Table 1: Data calculated by *Spartan* and given formulas for experimental compounds. Compounds are listed by number. Their corresponding 2D structures appear in Fig. 4.

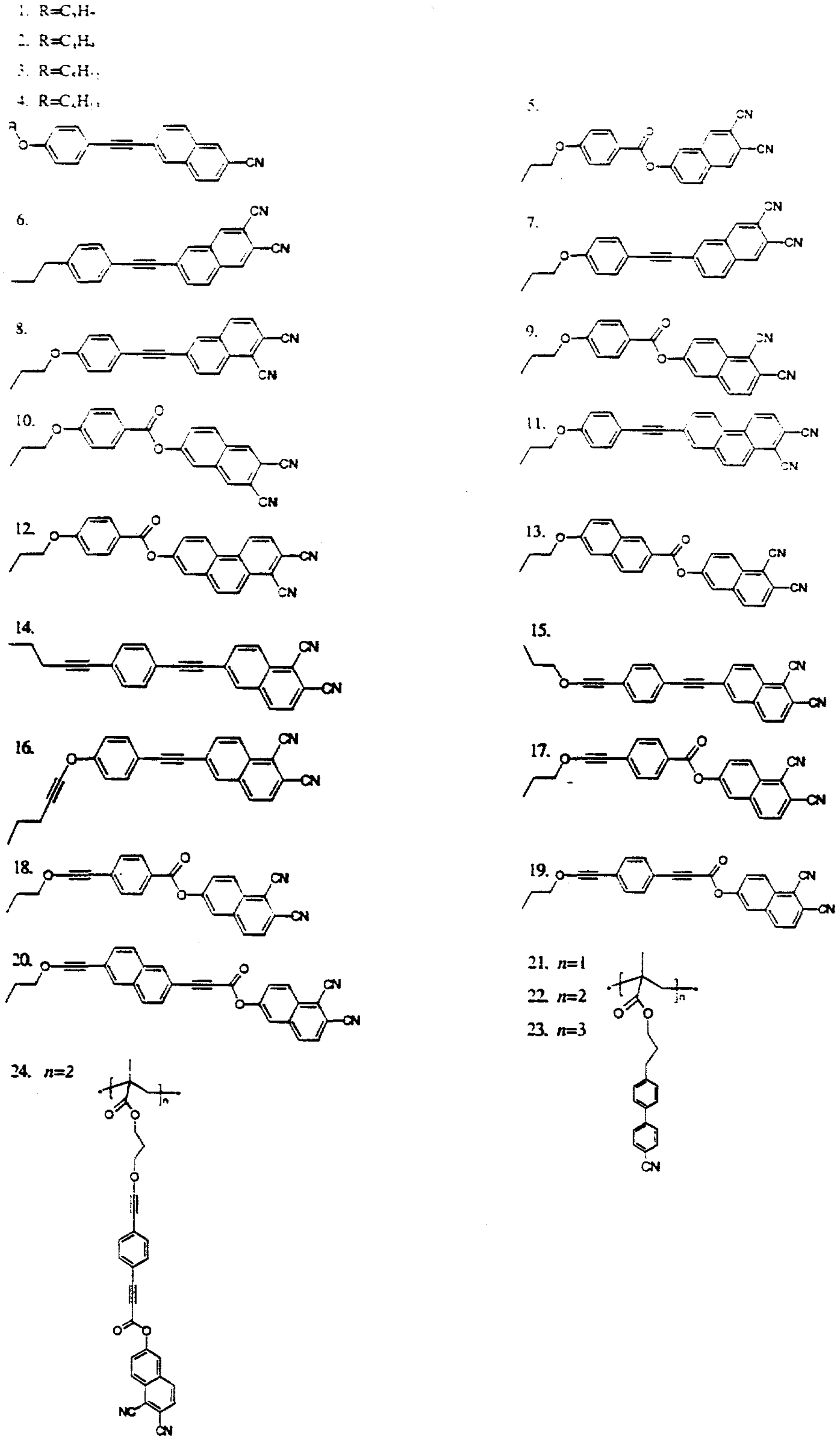

Fig. 4: Two-dimensional structures of all mesogens modeled.

References:

[1] G. Saitoh, M. Satoh, and E. Hasegawa, "Estimating Dielectric Anisotropy of Liquid Crystal Compounds," *NEC Res. & Develop.*, **37**, 497 (1998).

[2] T. Kosc, private communication.

[3] M. Klasen, et al., "Calculation of Opitcal and Dielectric Anisotropy Nematic Liquid Crystals." *Jpn. J. Appl. Phys.*, **37**, 945 (1998).

[4] M. Klasen, private communication.

Measurement of Scattered 351nm Light From OMEGA Targets

Emily Walton

Advised by Dr. James Knauer
University of Rochester
Laboratory for Laser Energetics
1999 Summer High School Academic Research Program

1. Introduction

When the OMEGA laser system fires, not all the laser energy is absorbed by the target. The energy that is not absorbed diffracts around the target and scatters on plasma. There is currently no precise way to measure this scattered light.

The OMEGA laser should ideally be focused to the critical surface around the target. The critical surface is the radius around the target where the electron density allows the electrons to resonate at the same frequency as the laser. At this surface, absorption of the laser energy is at a maximum and scatter is at a minimum. This surface changes as a function of time when the laser hits the target, first growing and then shrinking. Because the critical surface is not always in the same place, and the lenses are fixed focal point, the laser cannot always focus on the critical surface. As a result, some of the laser energy diffracts around the target and scatters on plasma. It is currently assumed that about 80% of laser light is absorbed and that the remaining 20% scatters uniformly over 4π, or the surface of the target chamber. If 0% was absorbed, the distribution of laser light on the target chamber surface would be 80 mJ per cm^2. Currently, plasma calorimeters are used to measure the scattered light, but these are not as accurate as we would like. UV sensitive photodiodes implemented in the OMEGA target chamber will provide a more precise measurement of scattered light than is possible with the plasma calorimeters.

2.Design of the UV Sensitive Photodiode

A photodiode has been designed to measure scattered light from OMEGA targets. It consists of collecting optics and a detector that converts the optical signal to an electrical signal. The detector can be coupled to an oscilloscope and the output can be fed to a computer.

2.1 Design of the Detector

The detector (Figure 1a-e) needs to be sensitive to 351nm light and reject 527nm and 1054nm light. It also needs to convert the light to an electrical output, be easy to assemble, and connect easily to other devices. To convert the light from an optical to an electrical signal, the detector contains an UV-005 PIN photodiode(Figure 2). Since this diode is sensitive to wavelengths from less than 200nm to greater than 1100nm, 3mm thick UG-11 filter glass from Schott Glass is placed before the photodiode(Figure 3). This filter glass has peak transmission at 330nm and transmission falls to less than one percent at 257nm and 388nm. There is a second transmission band with transmission greater than 1% from 699nm to 736 nm and peaking at 715nm. There are two more transmission bands, at 1060nm and 2400nm, but peak transmission is less than .01%.

The detector is designed for easy assembly and connection. The cathode of the photodiode is soldered to the BNC connector and the anode is connected to the ½ inch adapter (ground) with electrically conductive epoxy. This assembly is screwed into the aluminum holder, placing the sensitive spot of the photodiode at the image plane of the collecting optics. The BNC connector ensures easy connection to devices. The filter glass and two washers that act as field stops are also placed in the holder, and are held in place by a snap ring.

The detector sends the electrical pulse out through the BNC connector to a reverse bias circuit (Figure 4). This circuit sends the pulse to an oscilloscope, where the waveform is grabbed by a LabVIEW computer program.

Figure 1a: Front view of the holder

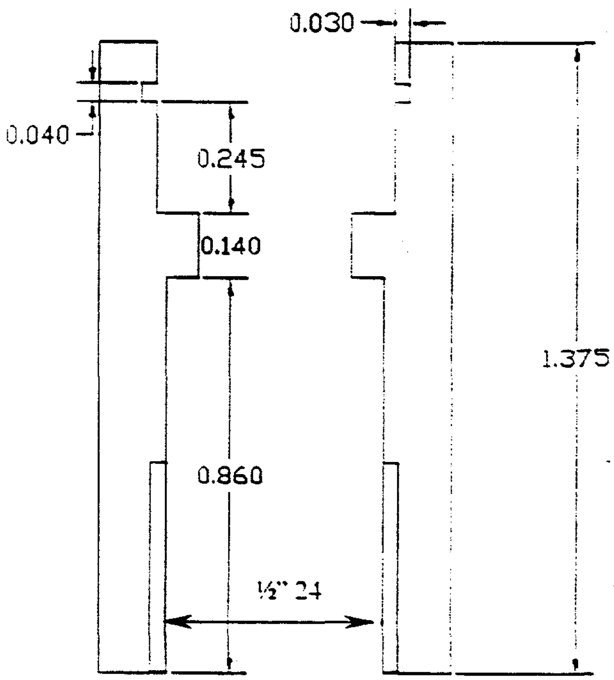

Figure1b: Bottom view of the holder

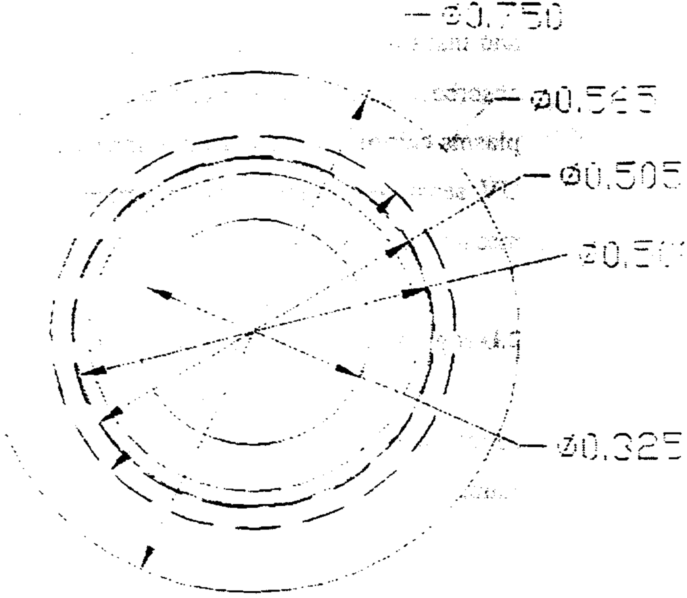

Figure 1c: Washer 1 top and side views

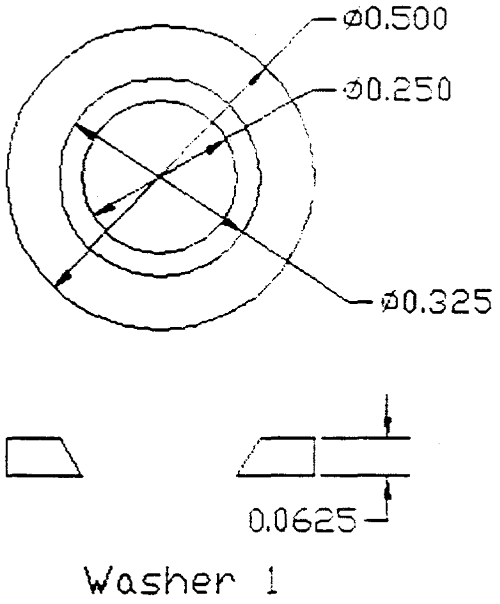

Figure 1d: Side and top views of washer 2

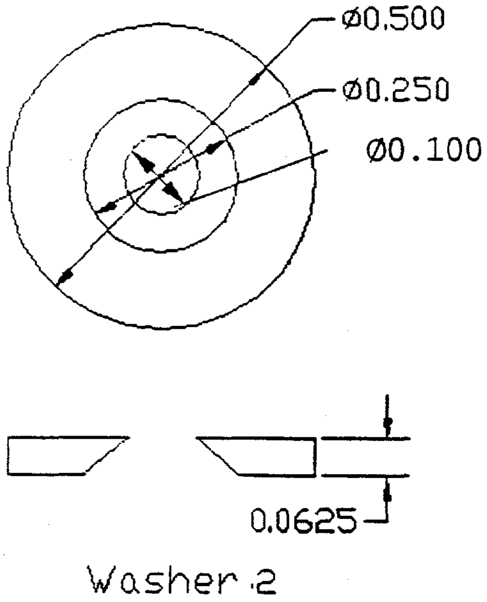

Figure 1e: ½ inch adapter for BNC connector

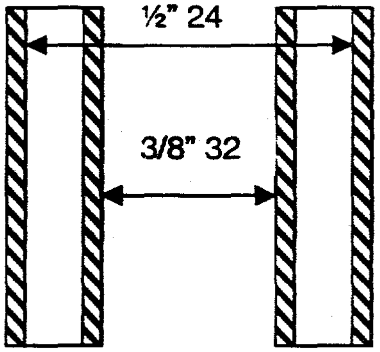

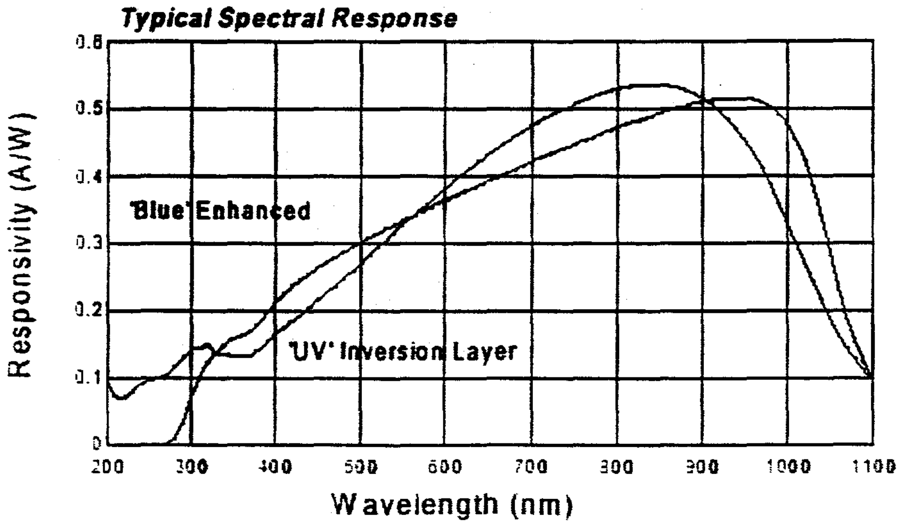

Figure 2: Response of the UDT UV-005 photodiode

Figure 3: transmission of UG-11 filter glass

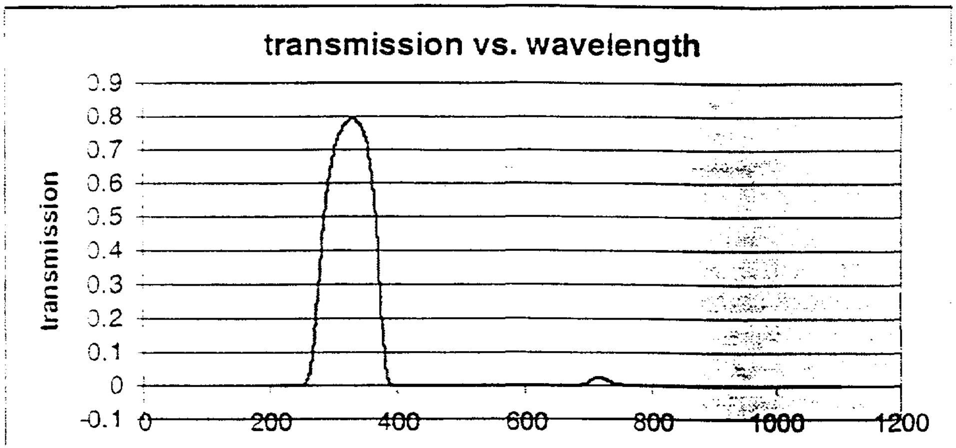

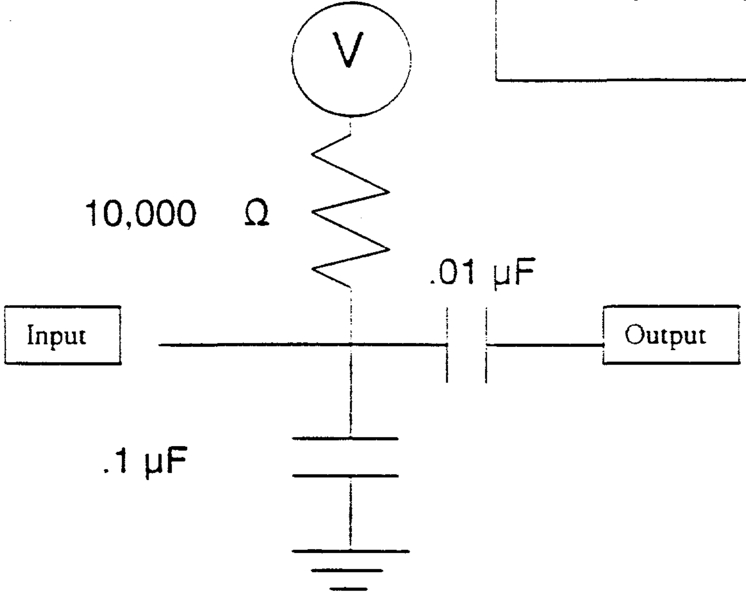

Figure 4: Reverse bias circuit

2.2 Optical Design of the Photodiode

The collecting optics are a modified Cassegrain system (Figure 5) with the second mirror replaced with a reflector made with fused silica. The fused silica reflector is ~50 mm in diameter and ½ inch thick at the top. The ideal focal length of the spherical mirror would be 50.481 cm, but a spherical mirror with focal length 50.8 cm available commercially would be more economical with minimal side effects.

There were three main considerations when designing the collecting optics: the thresholds of the photodiode, constructive or destructive interference at the fused silica reflector, and alignment.

Too much incident energy on the photodiode will cause either damage or nonlinearly of response. The photodiode has a linear response from about 0 to 0.5 mJ of incident light. The saturation current is reached around 0.6 mJ, and the damage threshold was not tested. To reduce the amount of incident light, the fused silica reflector and the spherical mirror were used together. Since the fused silica will reflect around 4% of incident light and the mirror will reflect ~90%, only 3.6% of incident light reaches the detector. In addition, the UG-11 filter glass in the detector has a transmission of ~75% at 351nm, so only ~2.7% of incident light reaches the photodiode. A neutral density filter may still be required.

Constructive and destructive interference could occur at a fused silica reflector with parallel sides. To counteract this, the reflector will be built with a ~.215° wedge on one surface.

A lens system would require alignment with a 351nm laser because the index of refraction changes with wavelength. A purely reflective system can be aligned with a visible laser, simplifying alignment.

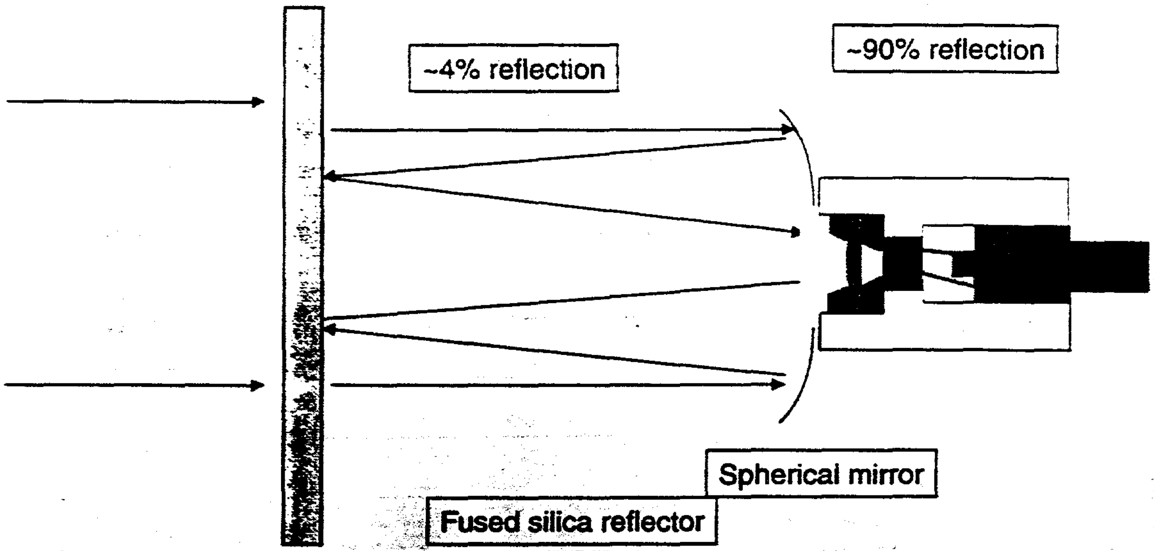

Figure 5: Collective Optics

3. Calibration of the Photodiode

The diode was tested in the Damage Testing Lab in the Laboratory for Laser Energetics(Figure 6). Like the OMEGA system, this laser starts in the far infrared, is converted to green, and finally to the near ultraviolet. Four percent of the laser entered a calorimeter, four percent entered the detector, and the other 92% went elsewhere in the damage testing system.

After leaving the detector as an electrical pulse, the signal was displayed on a Tektronix 520 oscilloscope. From the oscilloscope, a LabVIEW program grabbed 500 data points, one for every 8 nanoseconds, and stored them in an Excel file (Figure 7). Another Excel file stored the energy in, maximum of the signal, and minimum of the signal (Figure 8a-c). Compiling these files gave the maximum voltage out as a function of energy in. The results of this compilation are shown below. The increased scatter, change in slope, and increased error in the 20V graph show that 20V is too large a bias for this diode. Algebraic manipulation gave the energy out as a function of maximum voltage out (Figure 9). With this formula, the output of the detector can be matched with an incident energy.

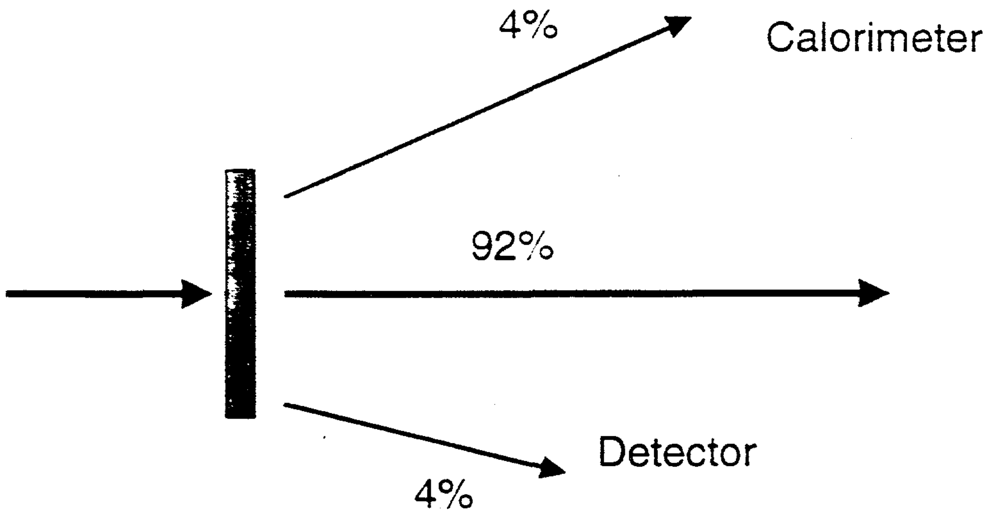

Figure 6(above): Set- up of Damage Testing laser

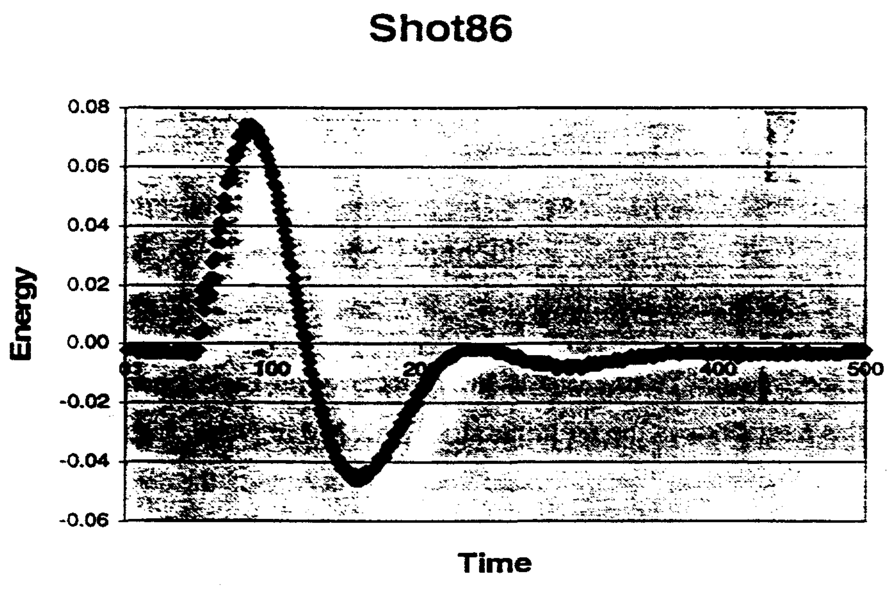

Figure 7: Example output Waveform from one shot

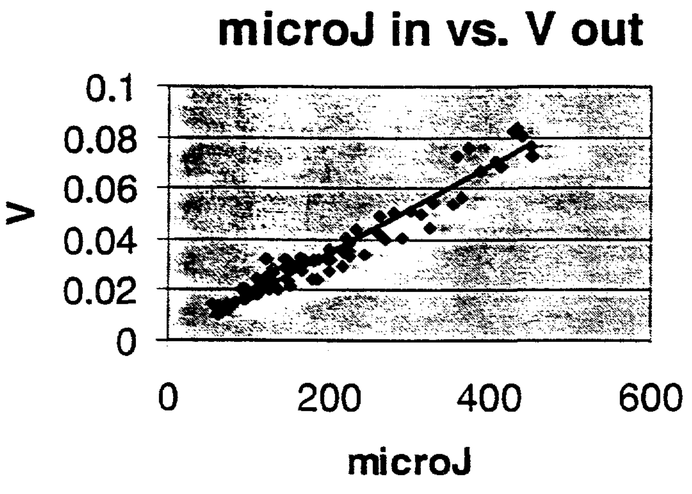

Figure 8a: Compilation for +10V reverse bias

V=. 172mJ in
Error = 2.2 E -3

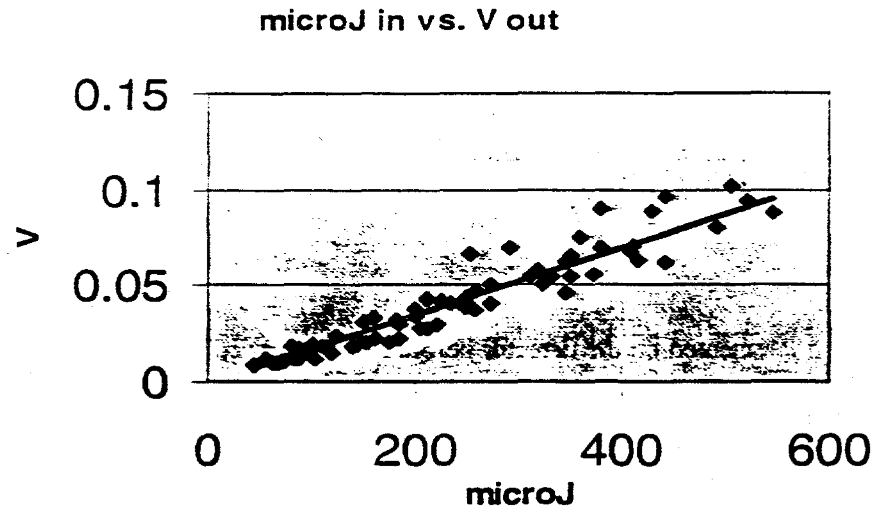

Figure 8b: Compilation for +15 volt reverse bias

V = .175 mJ in
Error = 3.34 E -3

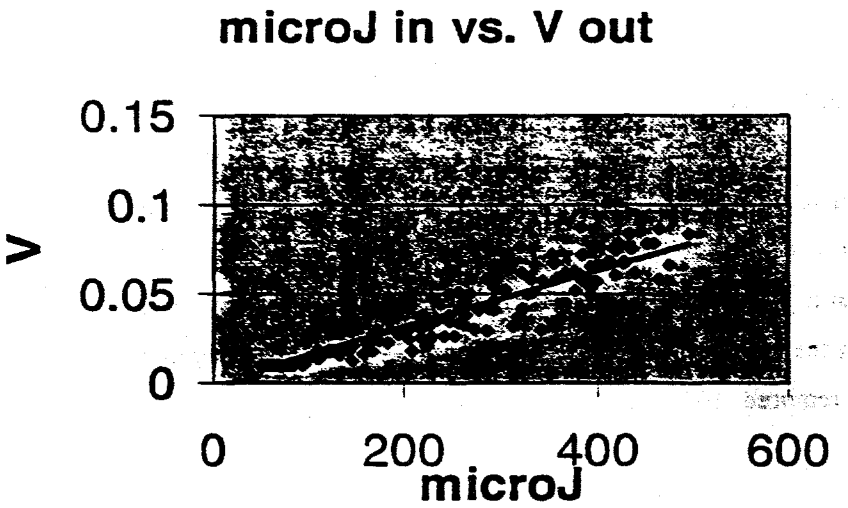

Figure 8c: Compilation for +20V reverse bias

V = .158 mJ in
Error = .281E-3

10V:

mJ in = 5.814 * Vout

Error = ± 3.34E-3

15V:

mJ in = 5.714 * Vout

Error = ± .109E-3

20V:

mJ in = 6.329 * Vout

Error = ±.113E-3

Figure 9: energy in as a function of voltage out

4. Possible Future Work

The optical design must be implemented on the detector before the detector can be placed in the OMEGA target chamber. With the collective optics, approximately 50mJ will enter the UDT UV-005 photodiode. This is well beyond the saturation point of 0.6mJ, so a neutral density filter may be required. Once placed on the target chamber, the photodiode should be used to study the intensity and distribution of scattered light.

5. Conclusion

The UV sensitive photodiode has been designed, but further work is needed before it can be used in the OMEGA target chamber. The optical system must be integrated with the detector, and it would be advisable to use a different photodiode. The UDT UV-005 does not have enough bandwidth to effectively measure the scatter. I would suggest replacing the UDT UV-005 photodiode with a photodiode with a faster response time, such as the 45GHz or 60GHz diodes available from New Focus, Inc. These diodes are designed for work in the infrared, so the response in the near UV range will be lower and a neutral density filter may not be required.

6. References

Jenkins and White, Fundamentals of Optics, 3rd Edition, New York: McGraw- Hill Book Company: 1957.

Halliday and Resnick, Fundamentals of Physics, New York, John Wiley & Sons, Inc.: 1970.

7. Acknowledgements

Dr. Knauer, for help with everything

Ray Bahr, for help with optics

Jeff Kramer, for help with electronics

Jeremy and Scott, for programming support